DYNAMIC BEHAVIOR OF LIQUID NANOFOAM AND ITS FUNCTIONALIZED MATERIALS AND STRUCTURES

By

Mingzhe Li

A DISSERTATION

Submitted to
Michigan State University
in partial fulfillment of the requirements
for the degree of

Civil Engineering — Doctor of Philosophy

2019

ABSTRACT

DYNAMIC BEHAVIOR OF LIQUID NANOFOAM AND ITS FUNCTIONALIZED MATERIALS AND STRUCTURES

By

Mingzhe Li

The use of energy absorption materials and structures for protection in collision, explosion, and impact attacks has long been recognized as one of the most effective approaches to reduce and prevent personnel injuries and infrastructure damages. These systems have been widely used in many industrial, medical, and military applications. Recently, an advanced energy absorption material, liquid nanofoam (LN), has been developed with high energy absorption capacity as well as high energy mitigation rate. The LN system, composed of a liquid phase and a hydrophobic nanoporous media, employs the pressurized liquid flow in nano-channels as its energy absorption mechanism. However, previous studies of the LN mainly focused on the quasi-static behaviors. Only limited effort had been made to understand the working mechanism of the LN under dynamic impacts which are the practical loading condition in scenarios such as auto collisions, blunt impacts and blasts. This dissertation presents the first systematic experimental study on the dynamic behavior of the LN system and reveals the deformation mechanism of LN under high strain rates. These scientific findings open up new applications of the LN functionalized materials and structures.

The intermediate and high strain rate responses of LN systems have been characterized by a lab-customized drop tower apparatus. The competition between liquid infiltration and porous structure deformation at high strain rates has been elucidated at nanoscale. Results show that liquid infiltration into nanopores is independent of the axial buckling stress of the nanopore, and thus is the dominating deformation mechanism of the LN. More importantly, the activation of liquid

infiltration as well as liquid flow in nanopores are much faster than the nanoscale porous structure deformation. This much-enhanced liquid flow speed in nano-environment is experimentally quantified for the first time. It has been demonstrated that the liquid infiltration speed is adaptive to the impact energy level, which provides mechanistic explanation for the high energy absorption efficiency of LN at high strain rates. Results also suggest that LN in the liquid marble form performs better than the liquid form upon high strain rate impact due to the macroscopically homogenous structure in the liquid marble form.

Based on the fundamental understanding of the deformation mechanism and the adaptive nanoscale liquid flow, LN has been integrated into other materials and structures to generate multifunctional materials and structures, e.g. LN-filled tube (LNFT), hybrid hydrogel, and advanced seat belt retractor system. In LNFT, LN is utilized as a novel filling material in thin-walled tube. The resulted LNFTs possess enhanced average post-buckling strength and energy absorption capacity due to the "perfect bonding" between the LN and the tube wall. Also, based on the adaptive nanoscale liquid flow, the LNFT is more efficient for energy mitigation at elevated strain rates. In LN-based hybrid hydrogels, LN is formulated and encapsulated in hydrogel by integrating nanoporous particles into the 3D polymer network. Liquid infiltration mechanism, combined with the chemical and physical cross-linking effects, leads to the improvement of both strength and toughness of the hybrid hydrogel, which is not seen in current hydrogels. In LN-based seat belt retractor system, LN is employed as the load-bearing component, which allows additional payout tunability, adaptability, and reusability in the system.

The knowledge gained in this study will facilitate the design of next generation of advanced LN-functionalized materials and structures for extreme working conditions.

Dedicated to my family

ACKNOWLEDGMENTS

The success in completing this dissertation would not have been possible without the support of a large number of people.

First and foremost, I would like to express my sincere gratitude to my advisor, Prof. Weiyi Lu, for his guidance, encouragement and support during my PhD study. I am deeply indebted for the training and resources he provided, which guided me through the journey to become an independent and hard-working researcher. His significant efforts put in refining my manuscripts and presentations, attention to the inconspicuous results, and strong desire to reveal the underling science have inspired my dedication to excellence. He is not just a great mentor but also a terrific friend. His passion and optimism have inspired and encouraged me to overcome all the obstacles I have encountered in research and my life. I am truly honorable to have such a great advisor in the pursuit of my PhD degree.

I would also like to thank my committee members, Prof. Roozbeh Dargazany, Prof. Venkatesh Kodur, Prof. Andre Lee, and my advisor, Prof. Weiyi Lu, for their generosity and willingness to review this dissertation, provide valuable comments, and attend the defense.

My sincere thanks also go to my colleagues and friends, Mr. Jisheng Chen, Mr. Bang He, Mr. Sihao Gu, Mr. Jun Guo, Mr. Junfeng Li, Ms. Wenqi Li, Mr. Xing Lu, Dr. Dennis Miller, Dr. Lars Peereboom, Ms. Lijiang Xu, Dr. Shutian Yan, Ms. Fuming Yang, Mr. Chi Zhan, Dr. Huan Zhang, Ms. Yani Zhang, Dr. Yi Zhu. I would also like to express my thanks to my colleagues at Ford Motor Company, Dr. Saeed Barbat, Dr. Ridha Baccouche, Mr. Jamel Belwafa, Dr. Zhenyan Gao, Dr. Robert McCoy, and Dr. Dean Jaradi, for their help and support.

Special thanks to the financial support from Michigan State University (start-up funds), Ford Motor Company (MSU-Ford Alliance program), and National Science Foundation (NSF-CBET-

1803695). I am also grateful for the fellowships and travel funds provided by the Department of Civil and Environmental Engineering, the College of Engineering and the Graduate School at Michigan State University.

Last but not least, I would like to thank my family for their overwhelming support and encouragement. To my parents, Junhai Li and Xiangying Kong, and my sister, Shaoqian Li, thank you for your love, support and always believing in me. To my parents-in-law, Bo Hou and Xinhuan Li, thank you for your love and encouraging me to pursue my PhD. Finally, I owe my deepest gratitude to my wife, Zhe. Thank you for your unconditional love, support, patience, and encouragement. I would like to dedicate this dissertation to you and our daughter, Siyan.

TABLE OF CONTENTS

| LIST OF TABLESx | | |
|-----------------|---|----|
| LIST O | F FIGURES | xi |
| Chapte | r 1 Introduction | 1 |
| 1.1 | Motivation | 1 |
| 1.2 | Background | 3 |
| | 1.2.1. Conventional Energy Absorption Materials | |
| | 1.2.2. Liquid Nanofoam | |
| | 1.2.3. Dynamic Behavior of Materials | |
| 1.3 | Research Objectives | |
| | Dissertation Outline | |
| Chapte | r 2 Competition of Deformation Mechanisms at Nanoscale | 23 |
| | Introduction | 23 |
| | 2.1.1. Which is more robust: liquid infiltration or nanopore deformation? | |
| | 2.1.2. Which is faster: liquid infiltration or nanopore deformation? | |
| 2.2 | Strength Competition | |
| | 2.2.1. Experimental | |
| | 2.2.2. Results and Discussion | |
| | 2.2.3. Conclusions | 37 |
| 2.3 | Speed Competition | 38 |
| | 2.3.1. Experimental | |
| | 2.3.2. Results and Discussion | |
| | 2.3.3. Conclusions | 46 |
| 2.4 | Summary | 46 |
| Chapte | r 3 Liquid Flow Speed in Nanopores | 47 |
| 3.1 | Introduction | |
| 3.2 | Materials and Methods | 48 |
| | 3.2.1. Material and Sample preparation | |
| | 3.2.2. Quasi-static compression test | |
| | 3.2.3. Dynamic Test | |
| 3.3 | | |
| 3.4 | Conclusion | 60 |
| Chapte | r 4 Effect of Sample Structure on Dynamic Behavior of LN | 62 |
| _ | Introduction | |
| 4.2 | Materials and Methods | 64 |
| | 4.2.1. Materials and Sample Preparation | 64 |
| | 4.2.2. Quasi-Static Compression Test | |
| | 4.2.3. Dynamic Impact Test | |
| 43 | Results and Discussions | |

| | 4.3.1. Quasi-Static Behavior of LN | 67 |
|--------|--|-----|
| | 4.3.2. Dynamic Behavior of LN | 70 |
| | 4.3.3. Effect of Sample Structure | |
| 4.4 | Summary | 74 |
| | | |
| Chapte | er 5 LN-Functionalized Thin-Walled Structure – Small-Scale | 75 |
| | Introduction | |
| 5.2 | Materials and Methods | 77 |
| | 5.2.1. Materials and Sample Preparation | |
| | 5.2.2. Test Procedures | 78 |
| 5.3 | Results | 79 |
| | 5.3.1. Liquid Infiltration Behavior of LN | |
| | 5.3.2. Quasi-Static Buckling Behavior of LNFT | |
| | 5.3.3. Dynamic Buckling Behavior of LNFT | 83 |
| 5.4 | Discussion | 86 |
| | 5.4.1. LN-Tube Wall Interaction | 86 |
| | 5.4.2. Effect of Liquid-Solid Interfacial Bonding | |
| 5.5 | Conclusion | 92 |
| | | |
| Chapte | er 6 LN-Functionalized Thin-Walled Structure – Large-Scale | 94 |
| 6.1 | Introduction | 94 |
| 6.2 | Materials and Methods | 96 |
| | 6.2.1. Materials and Sample Preparation | |
| | 6.2.2. Test Procedures | |
| 6.3 | Results | |
| | 6.3.1. Liquid Infiltration Behavior of LN | |
| | 6.3.2. Quasi-Static Behavior of LNFT | |
| | 6.3.3. Dynamic Behavior of LNFT | 102 |
| 6.4 | Discussion | 106 |
| | 6.4.1. LN-Tube Wall Interaction | |
| | 6.4.2. Effect of Incident Speed | 109 |
| 6.5 | Summary | 110 |
| | | |
| Chapte | | |
| | Introduction | |
| 7.2 | Materials and Methods | |
| | 7.2.1. Materials and Sample Preparation | |
| | 7.2.2. Test Procedures | |
| 7.3 | Results and Discussions | 115 |
| | 7.3.1. Quasi-Static Behavior of LN | |
| | 7.3.2. Morphology | |
| | 7.3.3. Mechanical Properties | 117 |
| 7.4 | Summary | 121 |
| | | |
| Chapte | · | |
| 8.1 | Introduction | 123 |

| BIBL | IOGRAPHY | 145 |
|-------|---|-----|
| APPE | NDIX | 137 |
| A DDE | NIDIV | 125 |
| | 9.3.2. Liquid Infiltration in Hydrogel under Unconfined Compression | 136 |
| | 9.3.1. High Strain Rate Test | |
| 9. | 3 Future Work | |
| 9. | 2 Limitations | 134 |
| | 1 Contributions | |
| Chapt | ter 9 Conclusions and Future Work | 133 |
| 8. | 5 Summary | 132 |
| 8. | 4 Results | 130 |
| | 3 Pulling Test Setup for LN-Functionalized Belt Retractor System | |
| | 8.2.2. Selection of LN for Desire Belt Retraction | 127 |
| | 8.2.1. Design of LN-Functionalized Seat Belt Retractor System | 125 |
| 8. | 2 Design | |

LIST OF TABLES

| Table 1-1: Summary of energy absorption materials |
|---|
| Table 1-2: Surface reagents and the bonded layer thickness [76,77] |
| Table 1-3: Control parameters of <i>P</i> _{in} |
| Table 2-1: $\Delta V_{\rm sp}$ and $P_{\rm in}$ of various IR01-based LN samples |
| Table 3-1: Effective liquid flow speed in a single nanopore |
| Table 5-1: Comparison of empty, water-filled, and LN-filled tubes under quasi-static compression tests. |
| Table 5-2: Comparison of empty, water-filled, and LN-filled tubes under dynamic tests 85 |
| Table 6-1: Comparison of empty and LN-filled tubes under quasi-static compression tests 101 |
| Table 6-2: Comparison of empty and LN-filled tubes under gas gun impact 105 |
| Table 8-1: The LN candidates used in this study |

LIST OF FIGURES

| Figure 1-1: (a) Persons killed in traffic accidents in the U.S. (b) A typical mechanical response of an energy absorber. |
|--|
| Figure 1-2: (a) The progressive folding of a steel tube (Reprinted from [36] with permission from Elsevier, Copyright 2003) (b) Common deformation modes of thin-walled tubes (Reprinted from [16] with permission from Elsevier, Copyright 2017) (c) Typical mechanical behavior of thin-walled tubes (d) Mechanical behavior of foam-filled tubes (Reprinted from [16] with permission from Elsevier, Copyright 2017) |
| Figure 1-3: (a) Aluminum foam (Reprinted from [38] with permission from The American Society of Mechanical Engineers, Copyright 2017) (b) Polystyrene foam (Reprinted from [39] with permission from John Wiley & Sons, Inc., Copyright 2015) (c) The deformation mode of a foam cell (Reprinted from [40] with permission from The Royal Society, Copyright 2006) (d) Typical mechanical response of a polyethylene foam. |
| Figure 1-4: An LN sample in a transparent PMMA testing cell |
| Figure 1-5: Three different types of nanoporous silica materials. (a) A microporous material (Reprinted from [71] with permission from American Chemical Society, Copyright 2015) (b) A mesoporous materials (Reprinted from [72] with permission from Elsevier, Copyright 2006) (c) A macroporous material (Reprinted from [73] with permission from The Royal Society of Chemistry, Copyright 2013). |
| Figure 1-6: Typical compressive behavior of LN containing nanoporous silica without surface treatment. |
| Figure 1-7: Schematic of surface modification |
| Figure 1-8: Typical surface treatment procedure |
| Figure 1-9: Experimental setup of surface treatment |
| Figure 1-10: Typical compressive behavior of LN containing nanoporous silica with surface treatment. |
| Figure 1-11: Schematic of the liquid infiltration mechanism in a nanopore |
| Figure 1-12: Schematic of the strain rate and related experimental techniques [89,90] |
| Figure 1-13: Strain rate sensitivity of various materials. (a) Copper (Reprinted from [97] with permission from Elsevier, Copyright 2006) (b) Steel (Reprinted from [98] with permission from Elsevier, Copyright 2008) (c) Polycarbonate (Reprinted from [99] with permission from Elsevier, Copyright 2001) (d) Polyurea (Reprinted from [100] with permission from Elsevier, Copyright 2007). |

| Figure 1-14: Strain rate sensitivity of cellular foams. (a) ALPORAS aluminum foam (Reprinted from [106] with permission from Elsevier, Copyright 2010) (b) Closed-cell aluminum foam (Reprinted from [104] with permission from Elsevier, Copyright 2005) |
|---|
| Figure 1-15: (a) A typical drop tower tester (Reprinted from [91] with permission from Elsevier, Copyright 2012) (b) A functionally graded aluminum foam subjected to drop tower impact (Reprinted from [108] with permission from Elsevier, Copyright 2015) |
| Figure 1-16: LN related studies including simulation, quasi-static experimental characterization and dynamic experimental characterization |
| Figure 2-1: Schematics of the LN system under loading (a) pressurized LN system (b) liquid infiltration (c) nanopore deformation including radial collapse and axial buckling of the nanopore. |
| Figure 2-2: Pore size distribution of IR01 characterized by water porosimetry technique (a) Cumulative volume of the intruded water as a function of applied external pressure (b) Pore size distribution of the nanoporous silica gel IR01 |
| Figure 2-3: SEM photos of the silica gel IR01 containing 3-D nanoporous structure with an average pore diameter of 115 nm |
| Figure 2-4: The schematic of the experimental setup of quasi-static compression test. The sample was sealed in a stainless-steel testing cell equipped with O-rings |
| Figure 2-5: SEM photos of the silica gel SG90 containing 3-D nanoporous structure with an average pore diameter of 7.8 nm |
| Figure 2-6: Loading history of the dry pre-compression on empty IR01 silica gels under various peak stress σ_{max} |
| Figure 2-7: (a) Sorption isotherm curves of IR01-based LN system without dry pre-compression (b) Sorption isotherm curves of LN system with dry pre-compression at $\sigma_{max} = 2$ MPa (c) Sorption isotherm curves of LN system with dry pre-compression at $\sigma_{max} = 4$ MPa (d) Sorption isotherm curves of LN system with dry pre-compression at $\sigma_{max} = 6$ MPa. The loading rate for all experiments was 1 mm/min. |
| Figure 2-8: Loading history of the dry pre-compression on empty SG90 silica gels under peak stress $\sigma_{max} = 24$ MPa |
| Figure 2-9: Sorption isotherm curves of SG90-based LN system with or without dry pre- compression |
| Figure 2-10: Schematic of the experimental setup of dynamic impact test. The drop weight is 10kg and the sampling rate is 10^6s^{-1} |

| Figure 2-11: (a) Loading history of the quasi-static compression and dynamic impacts on SN sample (b) Sorption isotherm curves of the LN consisting of SN after quasi-static compression or dynamic impact and 46 wt% LiCl aqueous solution |
|---|
| Figure 2-12: (a) Loading history of the quasi-static compression and dynamic impacts on LN sample (b) Sorption isotherm curves of the LN samples after quasi-static compression or dynamic impact |
| Figure 2-13: Schematic of the sample configuration (a) SN sample (b) LN sample with empty nanopores (c) LN sample with filled nanopores |
| Figure 3-1: Stainless-steel testing cell with two pistons equipped with O-rings |
| Figure 3-2: Pore size distribution of silica gel. The average pore diameter of the silica gel was measured to be 120 nm |
| Figure 3-3: Typical sorption isothermal curves of LN samples under quasi-static compression test. The strain rate is 7.4×10^{-3} s ⁻¹ . |
| Figure 3-4: Typical acceleration history of LN under dynamic tests at various strain rates of $1.3\times10^2~\text{s}^{-1}$, $2.8\times10^2~\text{s}^{-1}$, $5.8\times10^2~\text{s}^{-1}$. |
| Figure 3-5: Typical sorption isotherm curves of the LN sample (a) under dynamic tests (b) under quasi-static compression tests. |
| Figure 3-6: Schematic of effective liquid flow in LN sample. All the surface nanopores are accumulated as the total cross-sectional area A_n |
| Figure 3-7: Typical SEM image of silica particles (a) Image of a silica particle (b) Image of nanopores (c) Binary image of nanopores |
| Figure 4-1: Liquid marble (a) Schematic of a liquid marble in which water is stabilized with hydrophobic particles (b) Snapshot of a liquid marble composed of water and hydrophobic nanoporous silica. The diameter of a liquid marble ranges from micron level to millimeter level. |
| Figure 4-2: Typical sorption isothermal curves for both LN samples under quasi-static compression test |
| Figure 4-3: Typical dynamic loading curves of LN samples. (a) The LN-L sample (b) The LN-M sample |
| Figure 4-4: (a) Snapshot of LN-L sample (b) Schematic of LN-L sample structure (c) Snapshot and microscopy image of LN-M sample (d) Schematic of LN-M sample structure |
| Figure 4-5: Typical acceleration history of LN-L sample under dynamic impacts. The rising time is defined as the time from the initiation of external impact to the beginning of liquid infiltration. |
| |

| Figure 5-1: A typical LNFT sample with outer diameter of 12.7 mm and effective height of 20.3 mm |
|--|
| Figure 5-2: Typical sorption isothermal curves of LN under quasi-static compression test and dynamic impact test |
| Figure 5-3: (a) Typical stress-strain curves of filled steel tubes (b-d) Snapshots of the buckling behavior of (b) Empty tube (c) Water-filled tube (d) LNFT |
| Figure 5-4: Typical stress-strain curves of tubes under dynamic tests (a) Empty tube (b) Water-filled tube (c) LNFT with R_m =0.3 (d) LNFT with R_m =0.55 |
| Figure 5-5: Energy absorption of each part in LNFT under quasi-static compression tests and dynamic tests |
| Figure 5-6: Typical stress-strain curves of PE foam-filled tubes (a) under quasi-static compression tests (b) under dynamic tests. |
| Figure 5-7: Comparison of <i>C</i> in foam-filled tubes, including LNFT in this work, bonded solid foam-filled tube [25,26,28,177–179], unbonded solid foam-filled tube [24,27,29,30,175,176,178,179] and PE foam-filled tube in this work |
| Figure 5-8: Schematic of the filler-tube wall interaction of (a) Empty tube (b) Solid foam-filled tube with imperfect interfacial bonding (c) LNFT or solid foam-filled tube with perfect interfacial bonding. |
| Figure 6-1: A typical large-scale LNFT sample with outer diameter of 76.2 mm and effective height of 81.3 mm. The LNFT was sealed by two metallic caps equipped with O-rings 97 |
| Figure 6-2: Schematic of the experimental set-up of gas gun impact test |
| Figure 6-3: Typical sorption isothermal curves of the LN used in current study under quasi-static compression test |
| Figure 6-4: (a) Typical stress-strain curves of Al tubes (b-c) Snapshots of the buckling behavior of (b) Empty tube (c) LNFT |
| Figure 6-5: Typical stress-strain curves of empty Al tubes under gas gun impact |
| Figure 6-6: Snapshots of empty Al tube under gas gun impact |
| Figure 6-7: Typical stress-strain curves of LNFTs under gas gun impact |
| Figure 6-8: Typical sorption isothermal curves of the LN in LNFTs after quasi-static compression test and gas gun impact test |
| Figure 6-9: Snapshots of LNFT under gas gun impact |
| Figure 6-10: Wall thickness profile along the cross-section of empty tube and LNFT |

| Figure 7-1: The schematic of the working mechanism of LN-functionalized hydrogel 114 |
|--|
| Figure 7-2: Typical sorption isothermal curves of the silica gel SP120 in F127 aqueous solution |
| Figure 7-3: SEM image of LN (SP120 in F127 aqueous solution) functionalized PAAm hydrogel. |
| Figure 7-4: Unconfined compressive stress-strain curves of PAAm hydrogels |
| Figure 7-5: The recovery ability of LN-functionalized PAAm hydrogels under unconfined compression |
| Figure 7-6: Tensile stress-strain curves of PAAm hydrogels |
| Figure 7-7: Confined compressive stress-strain curves of PAAm hydrogels |
| Figure 7-8: The toughness of LN-functionalized PAAm hydrogels |
| Figure 7-9: LN-functionalized PAAm hydrogels (a) before confined compression test (b) after confined compression test |
| Figure 8-1: (a) Schematic of traditional seat belt system in a vehicle (b) A typical seal belt retractor (c) A typical torsion bar |
| Figure 8-2: Cumulative estimated number of lives saved by seat belt use [214] |
| Figure 8-3: The LN-functionalized seat belt retractor assembly (a) with retractor housing and belt (b) a front view |
| Figure 8-4: Schematic of the force relation in the LN-functionalized seat belt retractor 127 |
| Figure 8-5: Typical sorption isothermal curves of the LN candidates (a) SP300-based LN (b) SP120-based LN |
| Figure 8-6: Snapshot of the belt pulling test |
| Figure 8-7: The mechanical response of LN-functionalized seat belt retractor (a) SP300-based LN (b) SP120-based LN |
| Figure 9-1: (a) Rate sensitivity in LNFTs. (b) Schematic of split Hopkinson pressure bar. (c) Schematic of experimental set-up of blast test |
| Figure 9-2: Triggering liquid infiltration in hydrogel under unconfined compression from four aspects |
| Figure A-1: Testing cell – piston sleeve |
| Figure A-2: Testing cell – piston. |

| Figure A-3: Drop tower – base and track | 140 |
|--|-----|
| Figure A-4: Drop tower – drop weight platform. | 141 |
| Figure A-5: Drop tower – drop weight. | 142 |
| Figure A-6: Cap for large-scale tube – confining part. | 143 |
| Figure A-7: Cap for large-scale tube – sealing part. | 144 |

Chapter 1

Introduction

1.1 Motivation

The rapidly evolving world is facing many grand challenges in the 21st century. One of the global problems is human injuries and infrastructure damages due to collision, explosion, and impact attacks. For example, road traffic crashes have been a leading cause of death in the U.S. According to the traffic safety report by National Highway Traffic Safety Administration (NHTSA), about 35,000 people are killed on roadways each year in the U.S. as shown in Figure 1-1a [1]. Road traffic injuries have placed a huge societal and economic burden. The advances in technologies have led to the emergence of autonomous vehicles which have potential to reduce traffic congestion and improve productivity [2]. Yet recent negative trends in crashes involving active driving technologies assisted vehicles have suggested the importance of passive protection system to save lives and prevent occupant injuries. Given these facts, it is urgent to develop protection systems with high energy mitigation efficiency for personnel and infrastructures.

Developing energy absorption materials and structures is a promising way to address the above challenge. When subjected to external impact, the energy absorption material deforms and converts the kinetic energy associated with the impact to other forms of energy. Thus, the transmitted load level, which reaches the protected personnel or infrastructures is alleviated. Figure 1-1b shows a typical mechanical response of an energy absorber. Ideally, the transmitted pressure, which is the stress level of the plateau, should be maintained below the safety threshold until the input energy is fully mitigated.

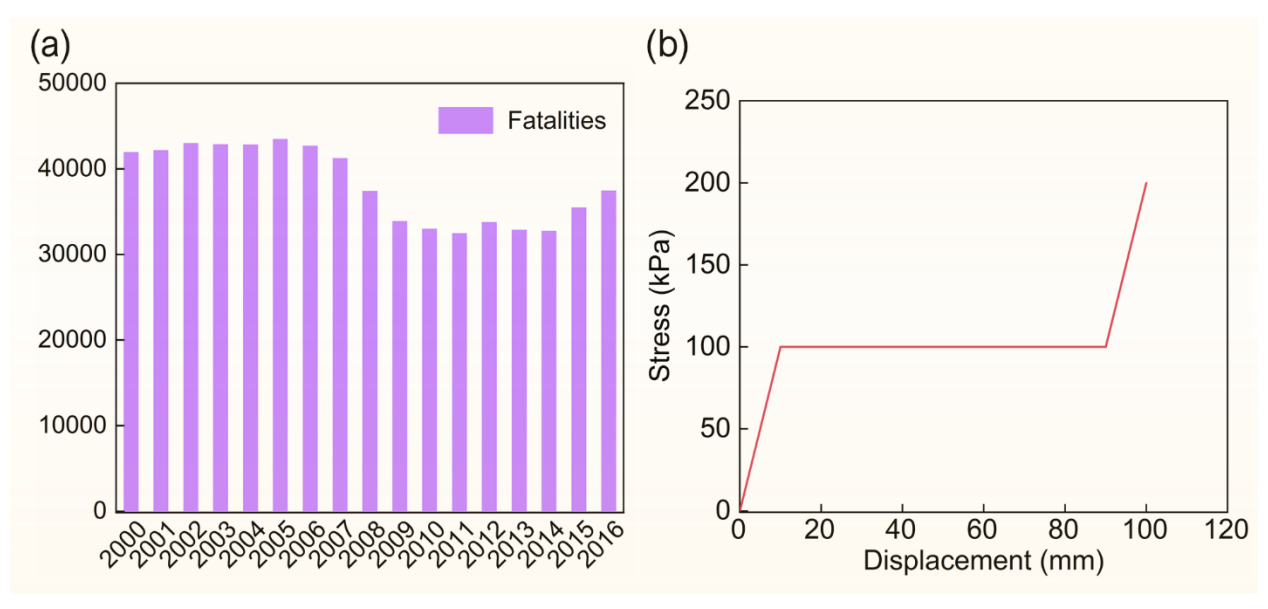


Figure 1-1: (a) Persons killed in traffic accidents in the U.S. (b) A typical mechanical response of an energy absorber.

In the past decades, various energy absorption materials have been developed for impact protection, such as cellular materials [3,4], granular materials [5,6], micro-trusses [7,8], fiber reinforced composite materials [9,10], and many others. However, several issues have limited their energy absorption performance. Firstly, upon impact, localized damage can be introduced and thus, the energy absorption capacity of the system cannot be fully utilized [11–13]. Secondly, as the loading speed increases, the materials cannot respond fast enough to the external loading. Consequently, the incident energy can penetrate the protection layer with negligible mitigation and cause severe damage. Thirdly, for most of these materials, the reusability is nearly zero as permanent deformation is the main energy dissipation mechanism.

In view of these challenges, we propose to study a novel energy absorption material – liquid nanofoam (LN), which combines a non-wettable liquid phase and a nanoporous media. This dissertation mainly focuses on the deformation mechanism and energy mitigation performance of the LN at intermediate and high strain rates. The research findings presented herein provide guidance on the design of next-generation advanced energy absorption materials and structures.

1.2 Background

1.2.1. Conventional Energy Absorption Materials

1.2.1.1. Thin-Walled Tube

Thin-walled and cellular structures are widely used energy absorbing devices in both military and commercial applications due to their superior performance, low cost, high deformability, and ease of manufacturing and installation [14–18]. The progressive plastic deformation of the metallic tube wall is known as its main energy absorbing mechanism. The metallic thin-walled tube can be applied to various loading situations, including axial crushing [19], lateral compression [20], lateral indentation [21], tube inversion [22], and tube splitting [23].

However, the tube wall buckling initiation requires a relatively large stress, after which the average post-buckling stress drops abruptly. The specific energy absorption, i.e. the gravimetric energy absorption efficiency, of empty tube is dominated by the post-buckling stress, which is much lower than the theoretical limit determined by the initial buckling stress.

For years, to close the gap between the practical and theoretical specific energy absorption of thin-walled tubes, researches have been focused on reinforcing the empty tube by metallic foam fillers. It has been demonstrated that the filler-tube interaction can effectively improve the energy absorption and mechanical properties of thin-walled tube under both quasi-static [24–28] and dynamic [29,30] conditions. However, due to higher density, metallic foam filled tube may show a lower specific energy absorption compared with empty tube [24]. Efforts have been made to improve it by using multi-cell tube [31], double-walled tube [32], conical configurations [33], light-weight foam[34], or numerical optimization [35].

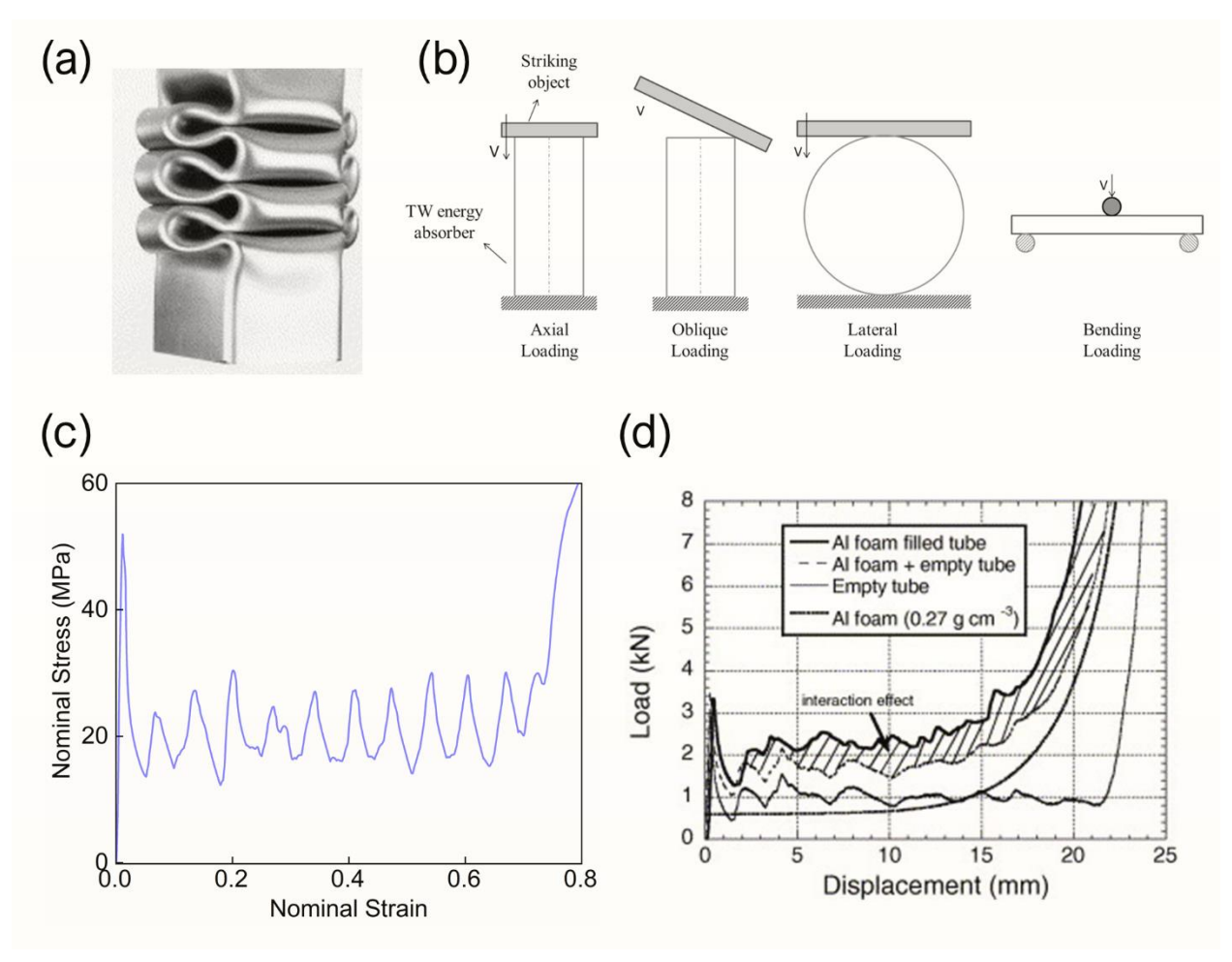


Figure 1-2: (a) The progressive folding of a steel tube (Reprinted from [36] with permission from Elsevier, Copyright 2003) (b) Common deformation modes of thin-walled tubes (Reprinted from [16] with permission from Elsevier, Copyright 2017) (c) Typical mechanical behavior of thin-walled tubes (d) Mechanical behavior of foam-filled tubes (Reprinted from [16] with permission from Elsevier, Copyright 2017)

1.2.1.2. Foams

Foams are cellular solid materials trapping pockets of gas inside. The high energy absorption capacity combined with high strength-density ratio has led foams to be used in many stiffness related and passive safety structures [37]. The controlling parameters of a foam include the cell structure, density and matrix materials. Based on its matrix, foams are classified into two kinds: polymeric foam such as polyurethane foam and metallic foam such as aluminum foam. Metallic

foams usually contains highly disordered cells (Figure 1-3a), whereas polymeric foams have a regular cellular structure (Figure 1-3b).

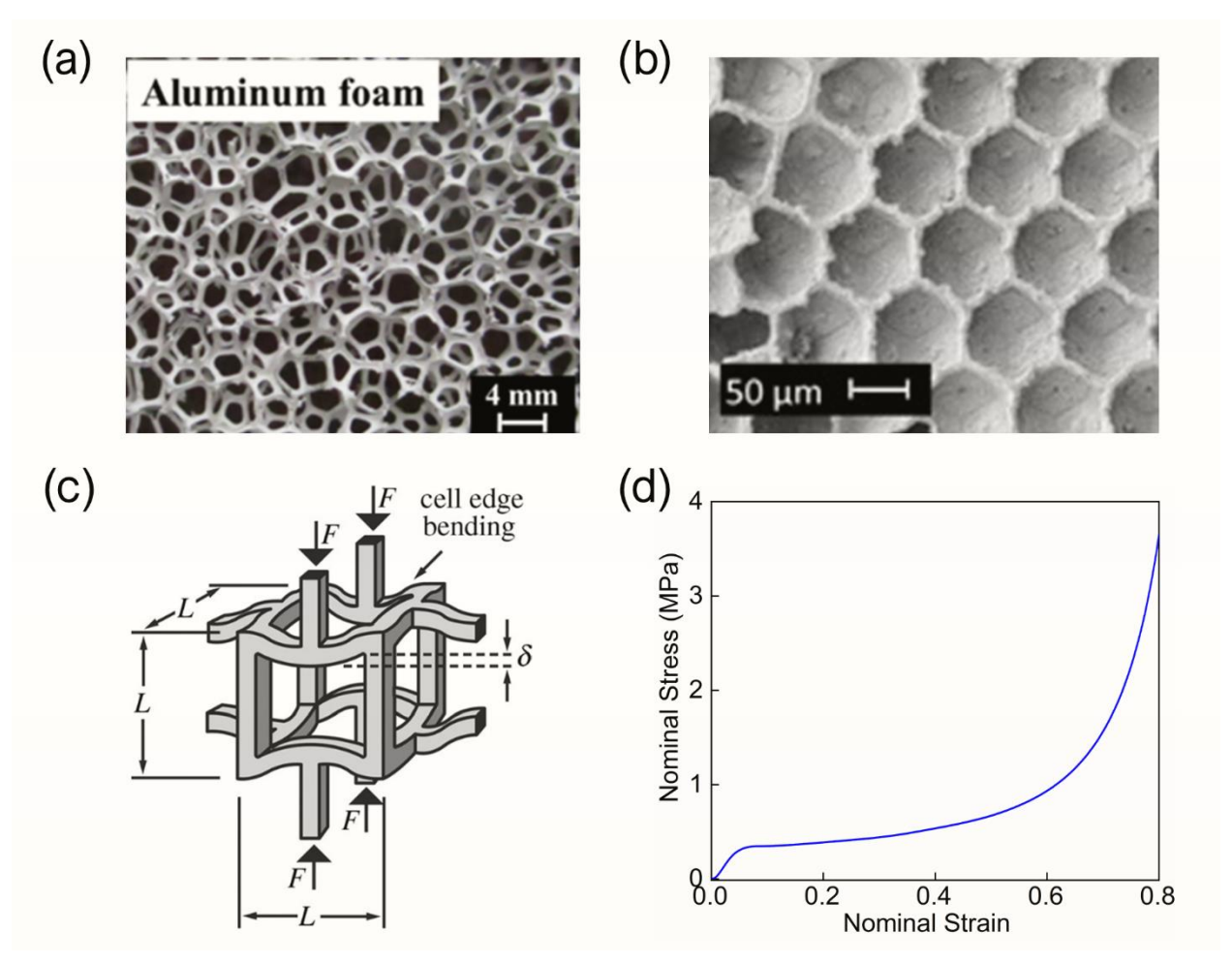


Figure 1-3: (a) Aluminum foam (Reprinted from [38] with permission from The American Society of Mechanical Engineers, Copyright 2017) (b) Polystyrene foam (Reprinted from [39] with permission from John Wiley & Sons, Inc., Copyright 2015) (c) The deformation mode of a foam cell (Reprinted from [40] with permission from The Royal Society, Copyright 2006) (d) Typical mechanical response of a polyethylene foam.

The energy dissipation mechanism of a foam is the deformation (bending or buckling) of the foam cell wall, as shown in Figure 1-3c. However, the damage localization, rate embrittlement effect and permanent deformation have limited the energy absorption performance of foams.

1.2.1.3. Other Materials

The energy absorption materials also include honeycombs [41], carbon nanotube forest [42], nanoand micro- trusses [43,44], composites [45–47], granular media [48,49], shear thickening liquid [50], etc. However, as previously discussed, the performance of these materials are limited by the rate embrittlement effect and damage localization effect (Table 1-1).

Table 1-1: Summary of energy absorption materials.

| Material | Mechanism | Issue |
|---|---|---|
| Thin-walled tube | Buckling of tube wall | Low energy absorption efficiency after buckling initiation, damage localization, rate embrittlement effect, permanent deformation |
| Foam, Honeycomb, Nano- and Micro trusses | Deformation of unit cell | Damage localization, rate embrittlement effect, permanent deformation |
| Carbon nanotube forest | Deformation of unit cell, internal friction | Damage localization, rate embrittlement effect, permanent deformation, shear |
| Composite | Fracture, delamination | Damage localization, rate embrittlement effect, permanent deformation |
| Shear thickening liquid | Shear thickening | Only applied in high shear rate |
| Granular media | Internal friction | Localized force chains |

1.2.2. Liquid Nanofoam

In the past decade, a novel energy absorption system, liquid nanofoam (LN), with high energy absorption efficiency has been developed for high-performance passive protection devices [51–57]. Figure 1-4 shows a typical LN sample in a transparent poly(methyl methacrylate) (PMMA) testing cell. LN system is composed of two phases: a nanoporous material phase containing large volume fraction of nanometer pores whose surface is specially treated and non-wettable to the liquid phase [56], and a liquid phase where the nanoporous material is immersed.

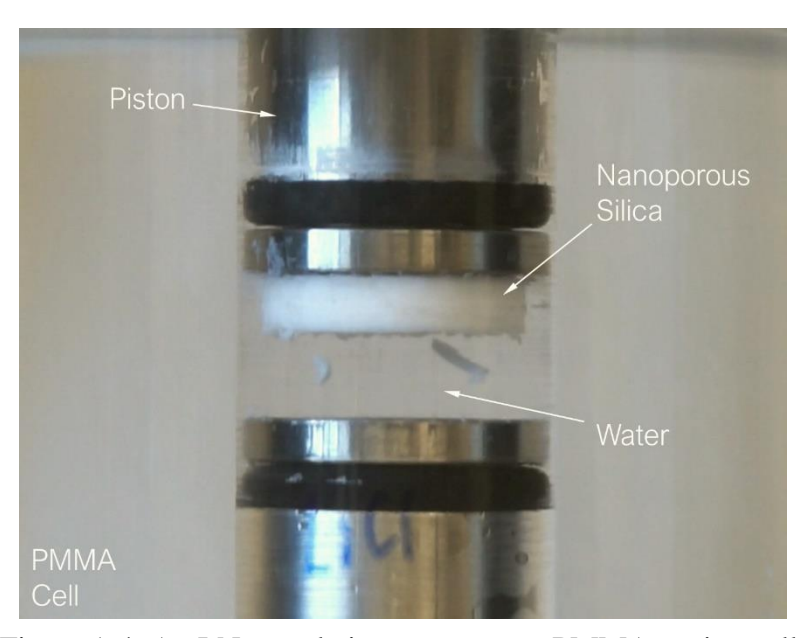


Figure 1-4: An LN sample in a transparent PMMA testing cell.

1.2.2.1. Nanoporous Particles

Nanoporous particles are widely used in a number of applications, such as sensing [58–62], molecular transportation [63–65], separation [66] and catalysis [67–70], due to their high specific surface area, unique framework and surface properties. Typical nanoporous materials include nanoporous silica, carbon, zeolites, polymer, ceramics, etc. Nanoporous materials are classified into three types based on its pore size, namely, microporous material (< 2 nm), mesoporous material (< 50 nm) and macroporous material (< 50 nm), as shown in Figure 1-5.

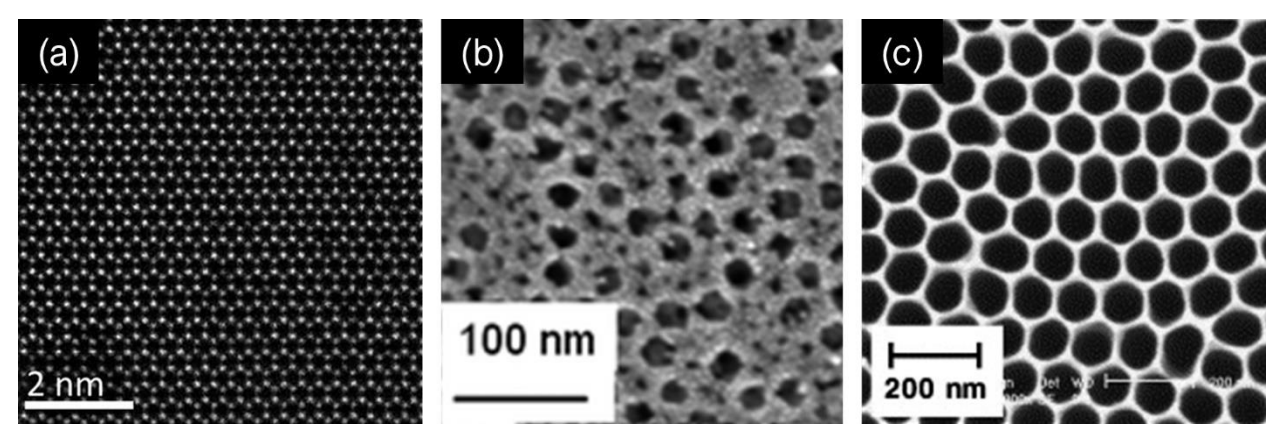


Figure 1-5: Three different types of nanoporous silica materials. (a) A microporous material (Reprinted from [71] with permission from American Chemical Society, Copyright 2015) (b) A mesoporous materials (Reprinted from [72] with permission from Elsevier, Copyright 2006) (c) A macroporous material (Reprinted from [73] with permission from The Royal Society of Chemistry, Copyright 2013).

In the past, enormous efforts have been made to develop methods to synthesize nanoporous materials. The widely used methods include templating methods [74] and nanocasting methods [75]. The templating method starts from a suitable template structure. In the templating step, the template is surrounded or bonded to the precursor. The created pore resembles the size and shape of the templates. Finally, the template is removed. Therefore, the properties and most importantly the size and interconnectivity of the pore can be tuned by the templates. Nanocasting is a powerful method for synthesizing nanoporous materials that are difficult to synthesize by conventional method. Hard templates are usually applied in this method to synthesis nanoporous material with ordered pore structures. The nanocasting method includes the formation of the hard template, the casting of precursor and the removal of the hard template. Ordered porous material, such as zeolite, alumina membrane, are commonly used in this method.

1.2.2.2. Surface Treatment

As discussed previously, the inner surface of nanoporous particles must be hydrophobic, so that the effective solid-liquid interfacial tension is larger than the combination of the effective surface tension of nanopore wall and the liquid. Thus, at ambient conditions, the nanopore surface can repel the liquid and keep it out of nanopores. Otherwise, the nanoporous particles would be soaked up spontaneously by the liquid and the system becomes rigid, as shown in Figure 1-6.

Surface modification is applied to increase the surface hydrophobicity of the nanoporous particles. One of the most efficient surface modification methods is to graft an alkyl layer on the nanopore surface [56], as shown in Figure 1-7. The interaction between the hydroxyl groups and the surface treatment reagent is:

The surface properties would be dominated by the grafted alkyl layer. Commonly used surface treatment reagent and their effective layer thicknesses are listed in Table 1-2. Figure 1-8 shows typical surface treatment procedure and Figure 1-9 shows the experimental set-up.

Table 1-2: Surface reagents and the bonded layer thickness [76,77].

| Surface Reagent | Effective Layer Thickness (nm) |
|---|--------------------------------|
| CH ₃ Si(CH ₃) ₂ Cl | 0.3 |
| $CH_3(CH_2)_7Si(CH_3)_2Cl$ | 0.8 |
| CH ₃ (CH ₂) ₁₇ Si(CH ₃) ₂ Cl | 1.4 |

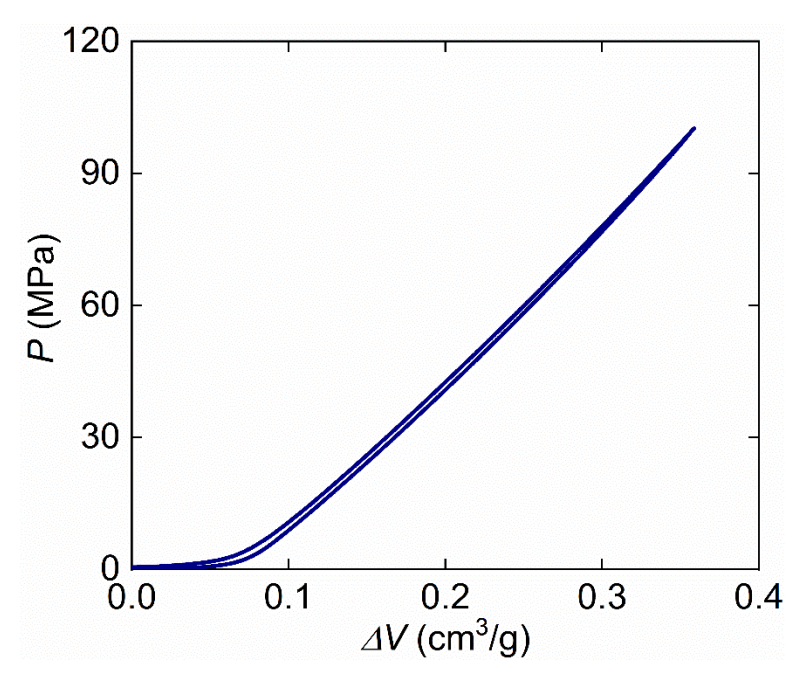


Figure 1-6: Typical compressive behavior of LN containing nanoporous silica without surface treatment.

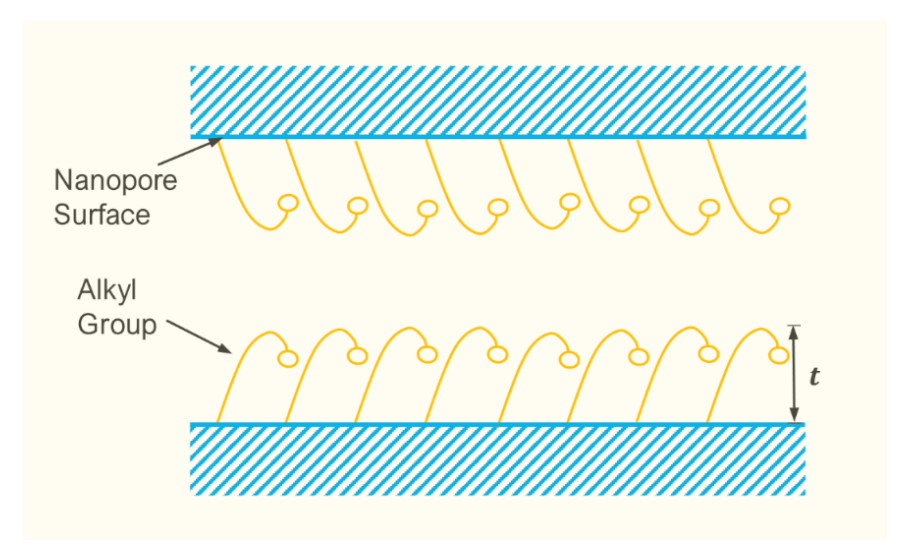


Figure 1-7: Schematic of surface modification.

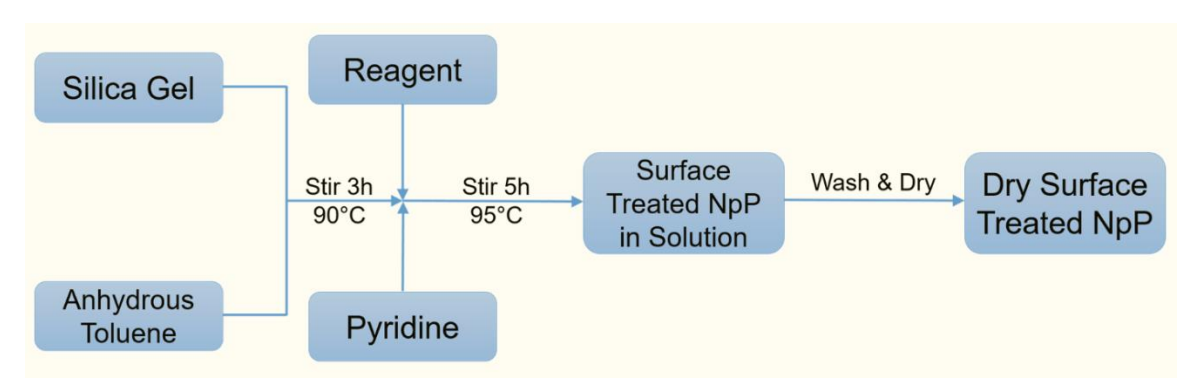


Figure 1-8: Typical surface treatment procedure.

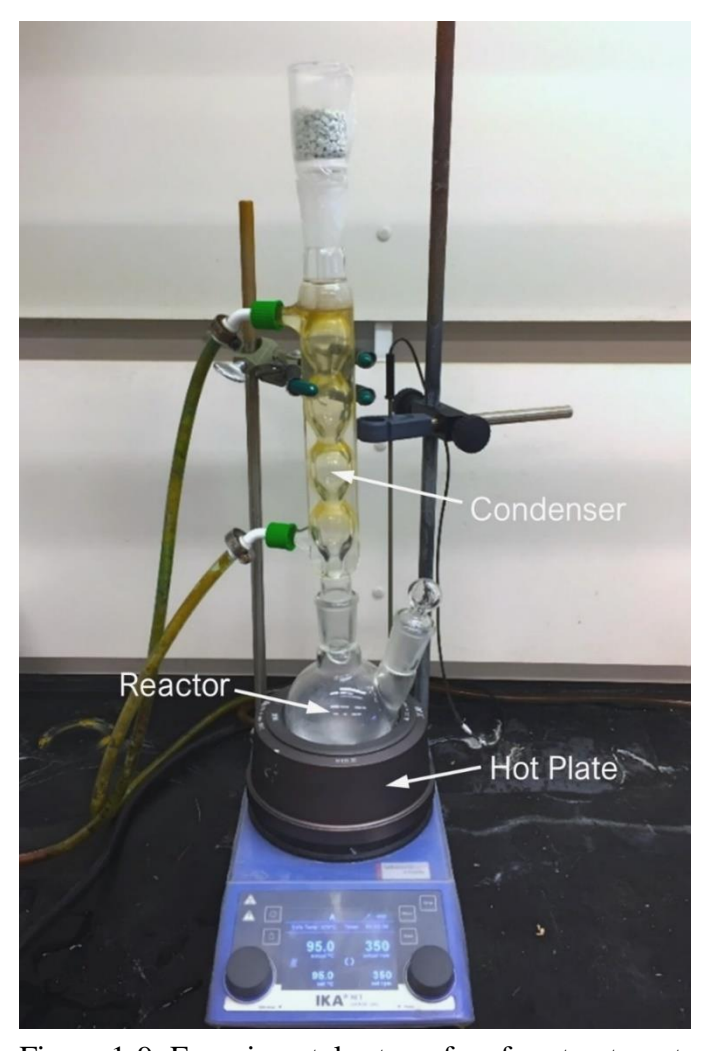


Figure 1-9: Experimental setup of surface treatment.

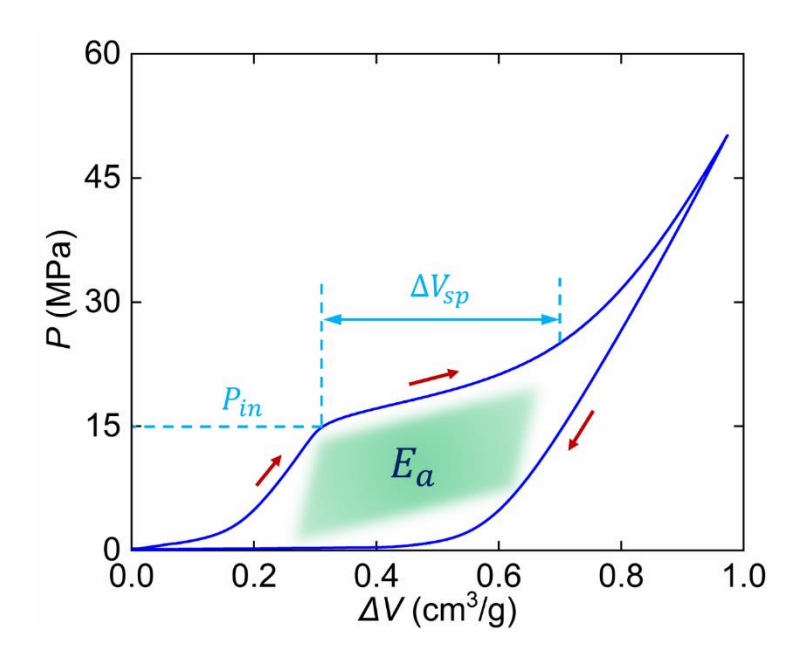


Figure 1-10: Typical compressive behavior of LN containing nanoporous silica with surface treatment.

After surface treatment, the nanoporous material can be used in the LN system. Typical compressive behavior of LN is shown in . As the external pressure is relatively low, the LN system volume decreased slowly. As the pressure increases to about 15 MPa, the slope of the curve decreases remarkably and an infiltration plateau can be observed. The plateau indicates that the capillary effect of the hydrophobic nanopore is overcome and liquid is driven into the nanopores. When the external pressure reaches around 25 MPa, the infiltration plateau ends. The pressure at which the liquid infiltrates into the nanopores is defined as the liquid infiltration pressure P_{in} . Therefore, the P_{in} ranges from 15 MPa to 25 MPa. The effective specific pore volume ΔV_{sp} , which is the volume change during liquid infiltration, is around 0.55 cm³/g. Upon unloading, the pressure drops abruptly, leading to a highly hysteretic behavior of the LN system. The area enclosed by the loading and unloading curves is the energy absorbed by the LN system E_a .

1.2.2.3. Liquid Infiltration Mechanism under Quasi-Static Loading Condition

Figure 1-11 shows the liquid infiltration mechanism in a single nanopore. Since the inner pore surfaces are hydrophobic, the liquid phase cannot enter the nanopores spontaneously under ambient condition. As the LN system is pressurized and the pressure reaches a critical value, the capillary effect is overcome. Consequently, the liquid molecules are driven into the nanopores. The nanopore surface is exposed to the liquid, creating energetically unfavorable solid-liquid interface. Upon removal of the external pressure, the solid-liquid interfacial tension is dissipated as heat [78]. Due to the ultra-large specific surface area (ranging from 100 to 1,200 m²/g [79]), tremendous amount of energy is dissipated.

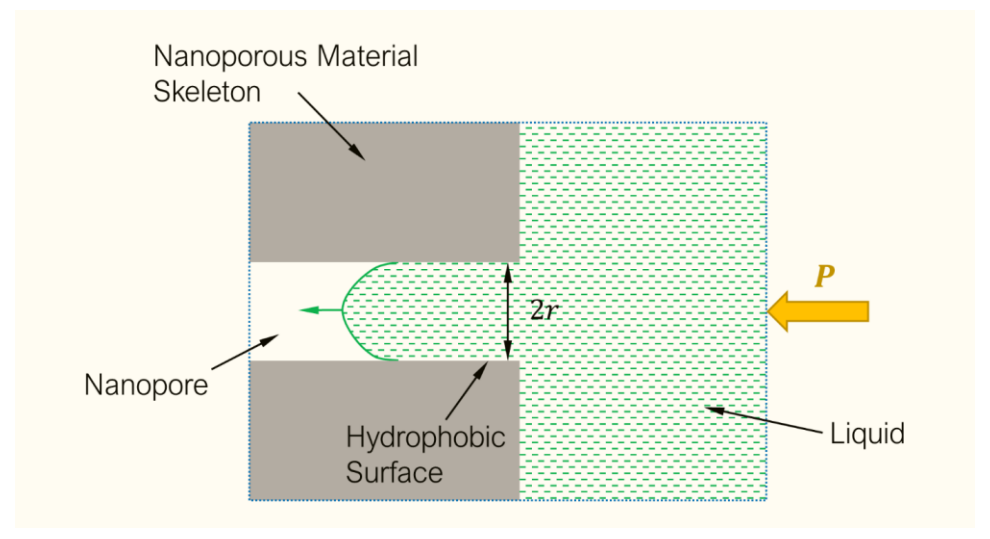


Figure 1-11: Schematic of the liquid infiltration mechanism in a nanopore.

1.2.2.4. System Parameters

The liquid infiltration pressure is governed by the Young-Laplace equation,

$$P_{in} = \frac{2\gamma \cdot cos\theta}{r} \tag{1-1}$$

where γ is the effective solid-liquid interfacial tension, θ is the contact angle between the liquid and nanopore surface, and r is the effective nanopore radius. Thus, P_{in} can be controlled by adjusting various factors, as summarized in Table 1-3.

Table 1-3: Control parameters of $P_{\rm in}$.

| Control Parameters | P_{in} |
|-------------------------------------|----------|
| Pore size [80] | ↓ |
| Surface coverage [56,81] | ↑ |
| Viscosity of liquid [82] | ↑ |
| Ion concentration in liquid [83–85] | ↑ |
| Temperature [86] | - |

^{*} The change in $P_{\rm in}$ is based on increasing value of each control parameter.

1.2.2.5. Advantages of the LN under Wide Range of Strain Rates

Based on previous study under quasi-static loading conditions [51–57], the LN system has multiple advantages compared with conventional energy absorption materials:

- (1) High energy absorption efficiency. Due to its ultra-large specific surface area and the unique energy dissipation mechanism, the LN system has high energy absorption efficiency ranging from 5 J/g to 100 J/g, much higher than that of conventional energy absorption materials [87];
- (2) Light weight and small size. The density of typical nanoporous materials is $0.1 \sim 0.5$ cm³/g and the size of nanoporous particles is $1 \sim 100$ µm. Due to its fluidity, the LN system can accommodate to any shape, making it a potential filling material in other materials and structures;
- (3) Reusability. With proper surface treatment of the nanoporous particles, the LN can be fully reusable [56]. This is beneficial for mitigation of second impact.
- (4) Tunability. The performance of LN can be controlled via tuning various parameters listed in Table 1-3. The LN can be customized to protect different personnel and infrastructures.

[&]quot;1" denotes positive correlation, "1" denotes negative correlation, and "-" denotes uncertainty

In current work, in the range of intermediate and high strain rates, the LN has additional advantages over conventional energy absorption materials and structures.

- (5) Ultra-fast response and energy mitigation rate. The liquid infiltration activation takes less than millisecond, which makes LN a promising energy absorber in high strain rate impact. It has also been numerically demonstrated that the LN system possesses ultra-fast energy mitigation rate for a single nanopore [54,88]. In this dissertation, we have experimentally demonstrated this ultra-fast response in chapter 2 and 3.
- (6) Suppression of damage localization. Due to the existence of the liquid phase, hydro-static pressure developed in LN is capable of preventing damage localization. This have been validated in chapter 5 and 6 in this dissertation.

1.2.3. Dynamic Behavior of Materials

1.2.3.1. Classification of Loading Conditions

When subjected to a high-speed loading, the materials or structures deforms rapidly, i.e. the values of strain rate are high. The mechanical response of the object at intermediate (1 s⁻¹) or above strain rates is defined as its dynamic behavior. The dynamic behavior of materials and structures is of great importance in evaluating the material performance for events such as collision, explosion, and ballistic impact. The loading conditions can be classified to several regimes according to the strain rate of the material (Figure 1-12).



Figure 1-12: Schematic of the strain rate and related experimental techniques [89,90].

Various experimental techniques have been developed to study the mechanical behaviors of materials under different strain rates. Quasi-static tests are typically accomplished by a variety of hydraulic or screw driven machines. The dynamic behavior is usually characterized by drop tower test [91], split Hopkinson pressure bar [92], gas gun impact [93], shock tube [94], or pressure-shear plate impact test [89], etc.

1.2.3.2. Strain Rate Effect on Mechanical Response of Materials and Structures

As the strain rate increases, the mechanical behavior of materials and structures may change drastically (Figure 1-13).

From the material science point of view, the strain rate dependence of materials is related to the microstructure of the materials. In crystalline materials such as metals, the dislocation motion and

interaction with interfaces leads to strain rate sensitivity of the materials [95,96]. Figure 1-13a and Figure 1-13b show the strain rate effect on the mechanical properties of metals.

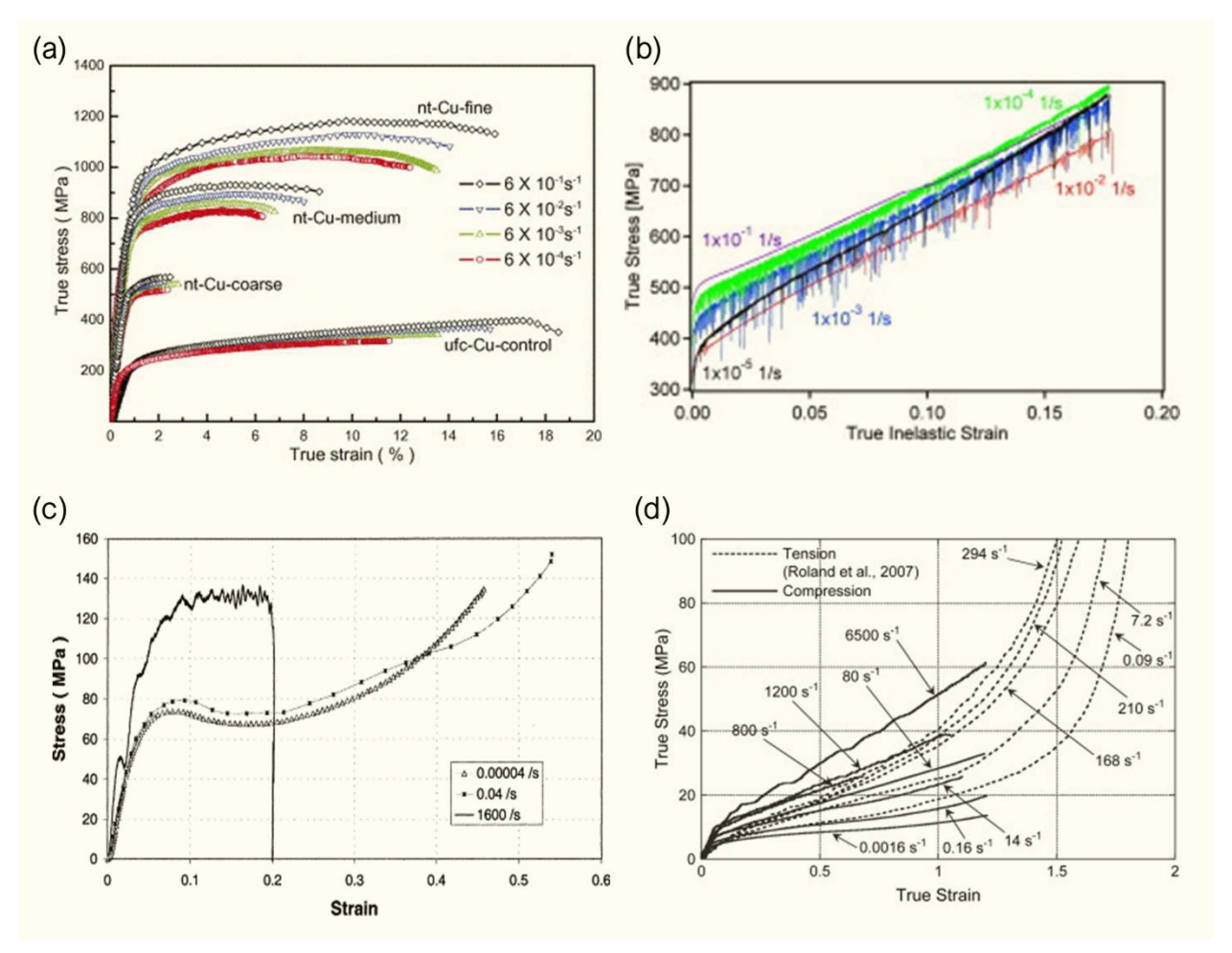


Figure 1-13: Strain rate sensitivity of various materials. (a) Copper (Reprinted from [97] with permission from Elsevier, Copyright 2006) (b) Steel (Reprinted from [98] with permission from Elsevier, Copyright 2008) (c) Polycarbonate (Reprinted from [99] with permission from Elsevier, Copyright 2001) (d) Polyurea (Reprinted from [100] with permission from Elsevier, Copyright 2007).

In amorphous materials such as polymers, the viscous flow of the polymer chain results in the viscoelastic behavior of the material, which is strain rate dependent, above its glass transition temperature [101]. Figure 1-13c and Figure 1-13d show the strain rate effect on the mechanical properties of polymeric materials. As the strain rate increases, the polymer becomes more rigid as well as brittle since the polymer chain movement is suppressed in short interval of time.

Strain rate can also affect the mechanical response of energy absorption materials and structures. For example, in cellular foams, micro-inertia effect leads to the strain rate dependency of both the plateau stress and the densification strain [102–106]. Figure 1-14 shows the strain rate sensitivity of various cellular foams. Typically, as strain rate increases, the buckling strength is promoted while the compressibility is reduced, which is problematic for protection as the increased buckling strength may exceed the safety threshold of the protected personnel or infrastructures.

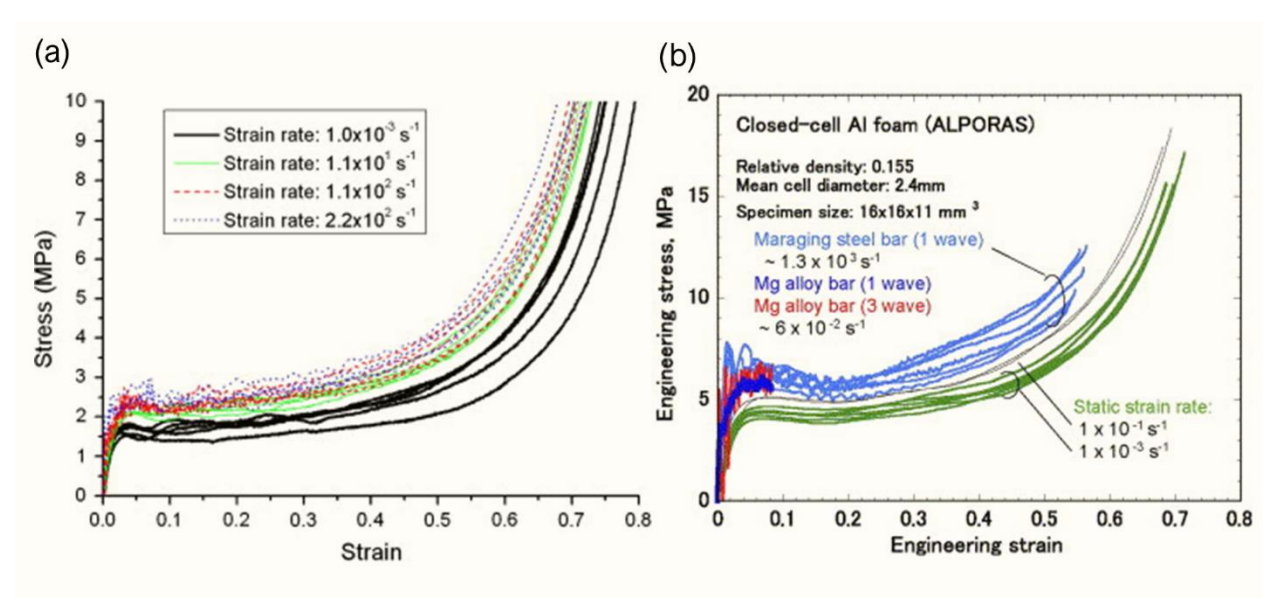


Figure 1-14: Strain rate sensitivity of cellular foams. (a) ALPORAS aluminum foam (Reprinted from [106] with permission from Elsevier, Copyright 2010) (b) Closed-cell aluminum foam (Reprinted from [104] with permission from Elsevier, Copyright 2005)

1.2.3.3. Working Mechanism and Experimental Setup of Drop Tower Tests

In a drop tower apparatus [107], a weight falls from a pre-determined height and impact the specimen which is supported on a horizontal base. The incident velocity of the drop weight is determined by the free-falling equation and measured by an accelerometer sensor located on the drop weight or optical sensor located just above the specimen. The force history of the impact is measured by the accelerometer or a load sensor located just below the specimen. Figure 1-15a shows a typical drop tower apparatus and Figure 1-15b shows a foam-core sandwich panel subjected to drop tower impact.

The advantages of drop tower test include: (i) it allows a wider range of sample geometries. (ii) The strain rate has a wider range from 10 to 10^3 s⁻¹. (iii) The experimental set-up is cost effective.

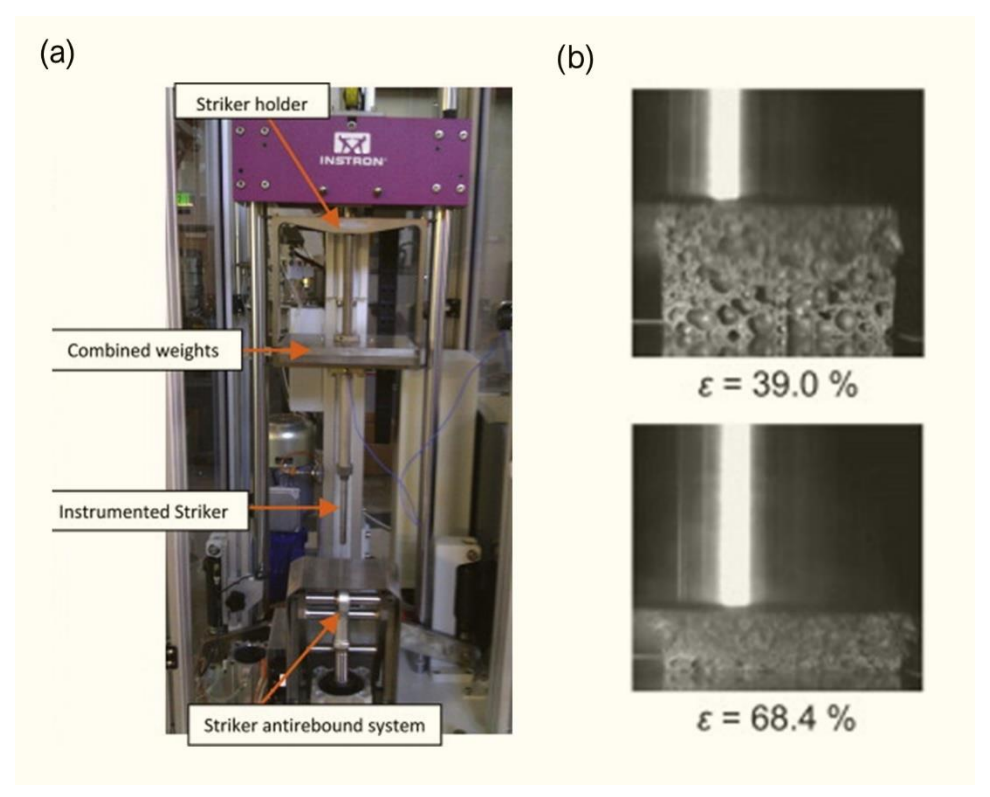


Figure 1-15: (a) A typical drop tower tester (Reprinted from [91] with permission from Elsevier, Copyright 2012) (b) A functionally graded aluminum foam subjected to drop tower impact (Reprinted from [108] with permission from Elsevier, Copyright 2015).

1.3 Research Objectives

The LN-based energy absorption system has been a topic of study for about one decade. Figure 1-16 summarizes that studies on LN system have been mainly focused on its quasi-static responses in the past decade. While the quasi-static behavior of LN system has been extensively investigated [79,109–119], it shed little light on the actual system performance under dynamic loading in practical applications. Therefore, characterizing the dynamic behavior of LN system is required to evaluate its energy absorption efficiency under real impact scenarios. Qiao et al. [120] conducted high speed impact experiment with SHPB (Split Hopkinson Pressure Bar) apparatus on Fluka 100 nanoporous silica-based LN system and Sun et al. [52] demonstrated the cushioning effect of

Zeolite β /water LN system. Despite of these results, the dynamic behavior of LN is still unclear and a systematic study on the dynamic behavior of the LN system is desired.

The focus of this research is to characterize the dynamic behavior of LN system and to understand the corresponding deformation mechanism. The liquid infiltration behavior of LN system at high strain rates will be elucidated and the energy absorption performance of LN system under dynamic impacts will be evaluated. We will also validate the ultra-fast response of LN system and demonstrate its extremely high and adaptive energy mitigation capability at high strain rate. The study will have merit in guiding the design of next-generation energy absorption materials and structures.

The second research objective is to experimentally characterize the liquid flow speed in the nano-environment. The liquid flow in nano-channels is considerably different from bulk phase liquid flow. While many researches have investigated the nanoscale liquid flow speed using cylindrical nano-channel (2D) models, this research features the study of nanoscale liquid flow using interconnected irregular 3D nanoporous structure.

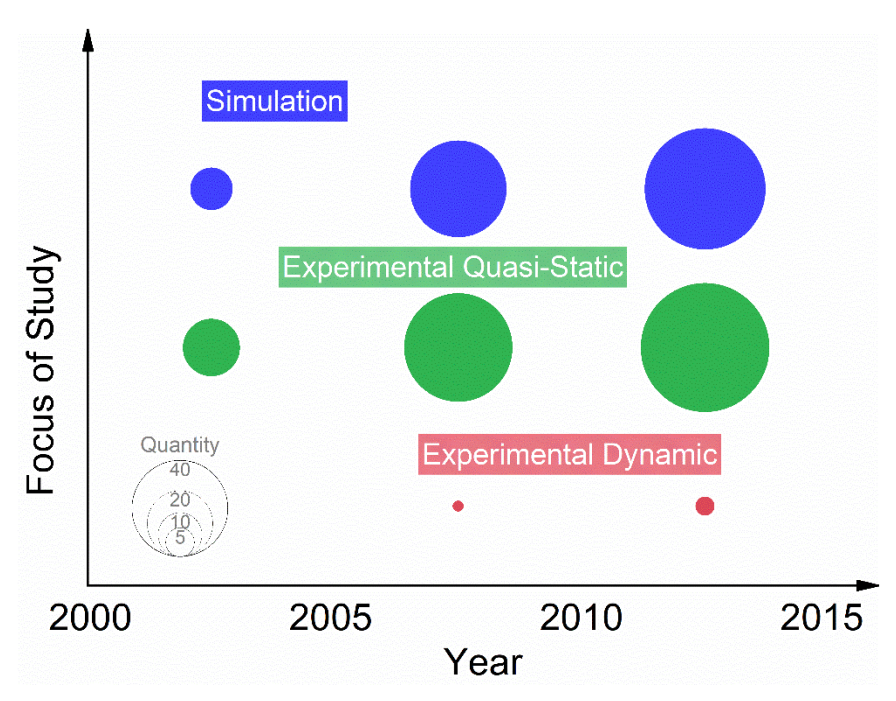


Figure 1-16: LN related studies including simulation, quasi-static experimental characterization and dynamic experimental characterization.

The third research objective is to realize the application of LN system in various materials and structure. The LN system will be used to functionalize other energy absorption or load bearing materials such as hydrogel, and structures such as thin-walled tube and vehicle belt retractor system. We will demonstrate that the LN system is an excellent energy absorbing component to be incorporated with other materials or structures.

1.4 Dissertation Outline

This dissertation consists of nine chapters. Chapter 1 introduces the motivation of this research. A brief overview of energy absorption materials and structures, liquid nanofoam, and dynamic behavior of materials is provided. Chapter 2 presents the competition mechanism between liquid infiltration and pore deformation in LN systems under both quasi-static compression and dynamic impact conditions. Chapter 3 presents an experimental method to characterize the liquid flow in 3D nanopores. Chapter 4 discusses the effect of sample structure on the performance of LN system under dynamic loading conditions. Chapter 5 reveals the reinforcement effect of LN on small scale thin-walled tubes and demonstrates the "perfect bonding" between LN and the tube wall, which leads to the enhanced filler-tube wall interaction. Chapter 6 presents an experimental study on large-scale thin-wall tubes filled by LN. Chapter 7 explores the reinforcement effect of LN on hydrogel. Chapter 8 provides a novel design of seat belt retractor using LN. Chapter 9 summarizes the main findings and discusses the future work.

Chapter 2

Competition of Deformation Mechanisms at Nanoscale

This chapter presents the competition mechanism between liquid infiltration and pore deformation in LN systems under both quasi-static compression and dynamic impact conditions. The strength competition was investigated quasi-statically and results show that liquid infiltration can always happen, independent of the critical axial buckling pressure of nanopores. The speed competition was studied by dynamic impact test and we have demonstrated that the speed of activation and liquid flow of LN is higher than that of pore deformation. The study reveals the fundamental competition mechanism between liquid infiltration and pore deformation, and sheds lights on the design of liquid nanofoam-based high-performance energy absorption materials and devices. The study on strength competition between liquid infiltration and pore deformation presented in this chapter was published in *Nanoscale* [121] and the study on speed competition between liquid infiltration and pore deformation presented in this chapter is to be submitted for publication consideration.

2.1 Introduction

The underlying energy dissipating mechanism of LN is to force a non-wetting liquid to flow into hydrophobic nanopores, converting the external mechanical energy into solid-liquid interaction energy and heat dissipated by solid-liquid surface friction [78]. Due to the ultra-large surface area of nanoporous material (~1000 m²/g), the energy absorption capacity can be as high as 100 J/g, much higher than conventional materials [120,122]. In addition, liquid may flow out of the hydrophobic nanopores upon removing the loading, making LN a reusable energy absorber. More

importantly, it has been theoretically validated that the LN system possesses ultra-fast energy dissipation rate. For example, the single carbon nanotube-based LN can be immediately activated at the incident speed of 1000 m/s [88].

While the energy dissipating mechanism of LN, namely liquid infiltration into nanopores, has been extensively studied, two fundamental questions regarding whether the liquid infiltration will happen or not remain unanswered.

2.1.1. Which is more robust: liquid infiltration or nanopore deformation?

As the LN system is pressurized (Figure 2-1a), the nanopore is subjected to a uniform load, leading to either liquid infiltration (Figure 2-1b) into the nanopore or nanopore deformation (Figure 2-1c). The pressure under which liquid infiltration occurs is determined by the Laplace-Young equation

$$P_{in} = \frac{2\gamma \cdot \cos\theta}{r} \qquad \qquad 2 - 1$$

where γ is the liquid-solid surface tension, θ is the contact angle between the nanopore surface wall and liquid, and r is the radius of the nanopore.

The pore deformation is classified into two different modes, i.e. axial buckling and radial collapse. The critical pressures dominating these modes are the critical axial buckling pressure P_{axial}^{cr} , and the critical radial collapse pressure P_{radial}^{cr} , respectively.

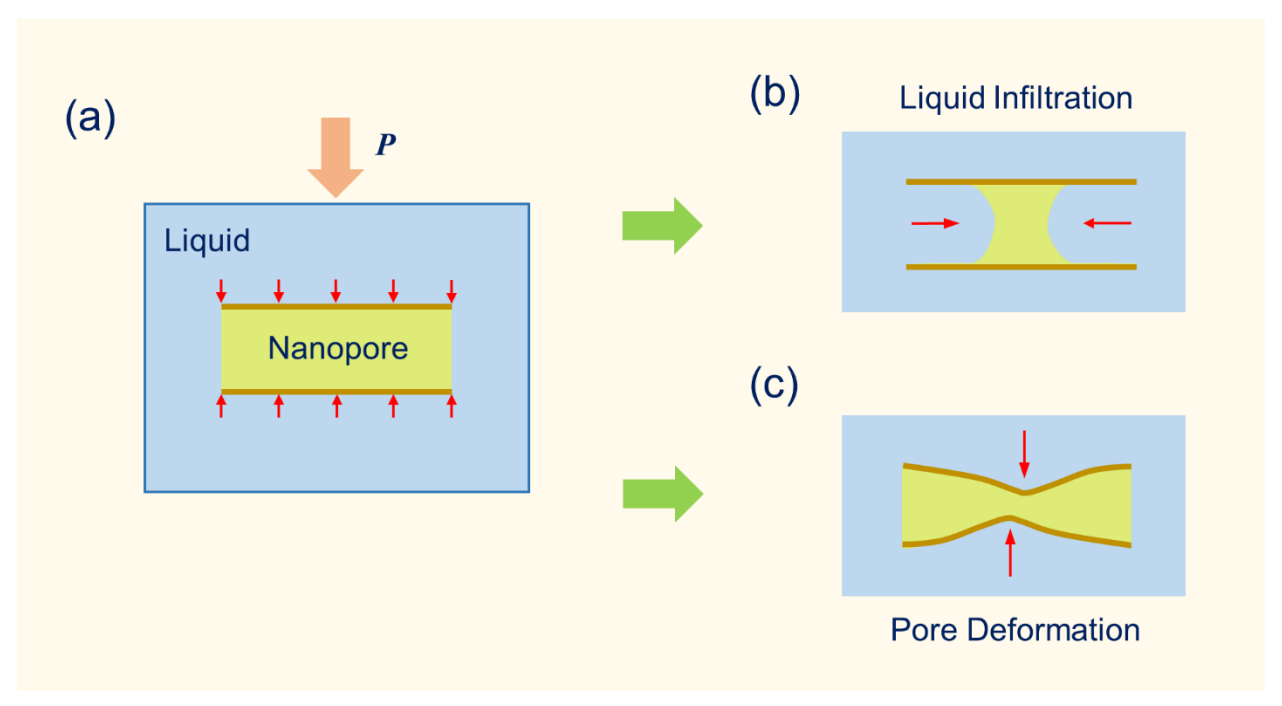


Figure 2-1: Schematics of the LN system under loading (a) pressurized LN system (b) liquid infiltration (c) nanopore deformation including radial collapse and axial buckling of the nanopore.

In this chapter we investigate the strength competition between liquid infiltration and nanopore deformation by comparing the quasi-static performance of two solid nanofoams (SNs) and SN-based LNs. One LN system has the quantitative relation of $P_{in} > P_{axial}^{cr}$ and the other $P_{in} < P_{axial}^{cr}$. Results show that liquid infiltration plateau can be observed for both LNs. Therefore, it is demonstrated that liquid infiltration occurs, independent of the axial buckling stress of the nanopore. The elucidation of this strength deformation competition mechanism will offer guidance for designing high performance energy absorption structures.

2.1.2. Which is faster: liquid infiltration or nanopore deformation?

As the strain rate increases, the nanopore may not respond fast enough due to inertia effect or shock wave effect [123]. The increased strain rate also requires much higher liquid flow speed in nanopores (red arrows in Figure 2-1b), while it has a limit [124–126]. That is, under high strain rate conditions, if the liquid infiltration is slower than pore deformation, pore deformation occurs regardless of the quantitative relationship between P_{in} and P_{axial}^{cr} or P_{radial}^{cr} . Evaluating the speed

competition between liquid infiltration and nanopore deformation is desired to demonstrate the high strain rate performance of LN.

Here we have investigated the speed competition between liquid infiltration and nanopore deformation by comparing the dynamic performance of a solid nanofoam (SN) and the SN-based LN. The P_{axial}^{cr} of the nanopore wall is lower than P_{in} . Under dynamic impact, the nanopore volume of SN are reduced, indicating the nanopores collapse; While for LN, the liquid infiltration behavior is not affected and the nanopore volume remains the same. Therefore, it can be validated that the liquid infiltration is faster than nanopore buckling. This piece of information is of great importance in order to evaluate the potential application of LN in high speed impact conditions.

2.2 Strength Competition

2.2.1. Experimental

Two LN systems were investigated in this session. The first SN (denoted as IR01) was a hydrophobic nanoporous silica (Perform-O-Sil 668, Nottingham Corp.). The as-received material was in powder form, with an average particle size of 4 µm. The average pore diameter was 115 nm, characterized by the water porosimetry technique (Figure 2-2) and scanning electron microscope (Figure 2-3). The corresponding liquid phase is saturated lithium chloride (LiCl) aqueous solution (46 wt%).

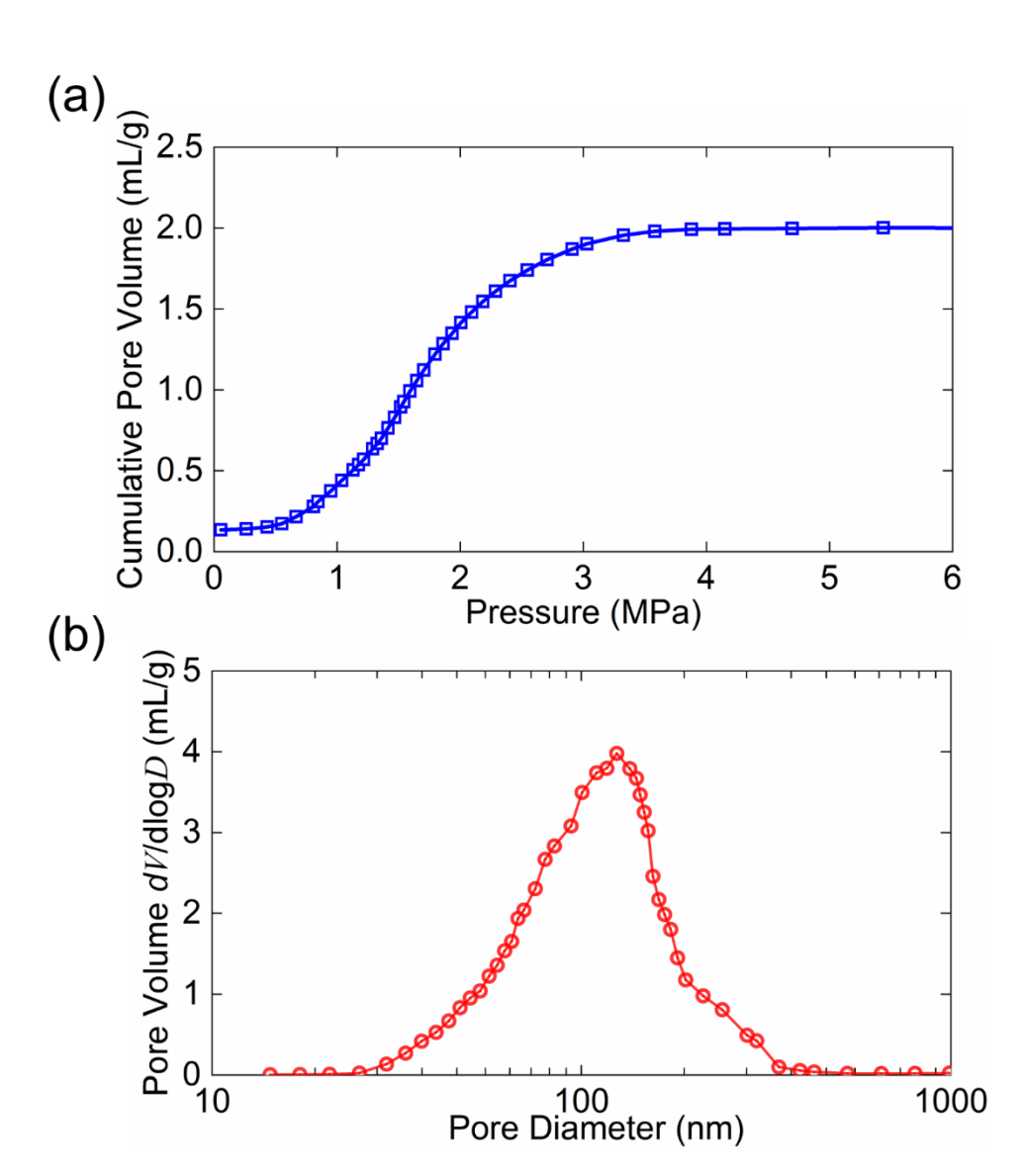


Figure 2-2: Pore size distribution of IR01 characterized by water porosimetry technique (a) Cumulative volume of the intruded water as a function of applied external pressure (b) Pore size distribution of the nanoporous silica gel IR01.

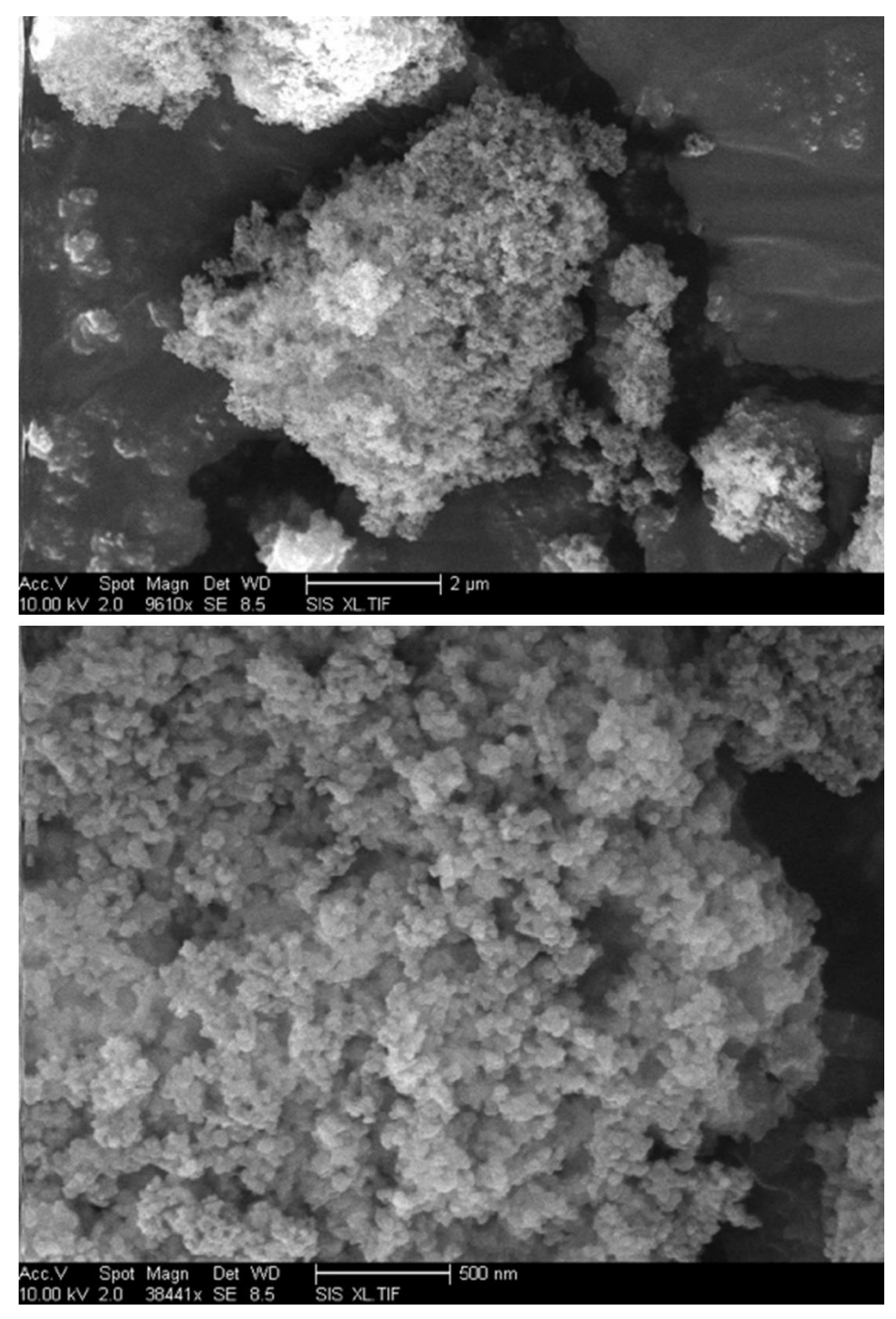


Figure 2-3: SEM photos of the silica gel IR01 containing 3-D nanoporous structure with an average pore diameter of 115 nm.

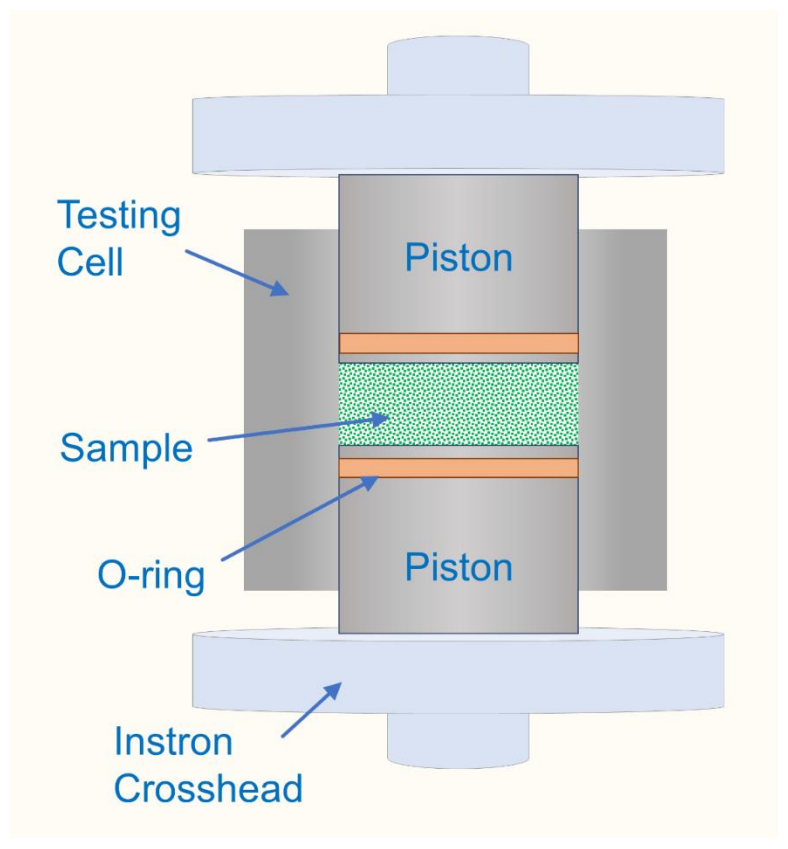


Figure 2-4: The schematic of the experimental setup of quasi-static compression test. The sample was sealed in a stainless-steel testing cell equipped with O-rings.

In a stainless-steel cylinder (Figure 2-4), 0.2 g of the nanoporous silica gel was first precompressed to various peak forces without the presence of liquid at a constant rate of 1 mm/min by a universal tester (Model 5982, Instron, Inc.). Once the peak force was reached, the crosshead of the Instron machine was moved back at the same velocity. The peak forces applied on silica gel IR01 samples were 0.25 kN, 0.50 kN and 0.75 kN, respectively. The cross-sectional area of the pistons, A_1 , was 126 mm². Thus, the applied peak stress, σ_{max} , were 2 MPa, 4 MPa, and 6 MPa accordingly.

Pressure-induced liquid infiltration tests were conducted on all the IR01 particles, with or without pre-compression, based liquid nanofoam (LN) systems. In the stainless-steel cylinder, 2 g of saturated lithium chloride (LiCl) aqueous solution (46 wt%) was slowly dropped on the silica gel samples to minimize air bubbles trapped in the LN specimens. Since the silica gel particles

were hydrophobic, they were not soaked up by the aqueous solution at ambient condition. The LN sample was sealed by two pistons with O-rings. The upper piston was driven into the cylinder by the Instron machine at a constant rate of 1 mm/min. When the internal pressure reached 9 MPa, the piston was moved back at the same speed. The friction between O-ring and cylinder wall was minimized by high vacuum grease and no leaking was observed during all infiltration tests. The applied pressure was calculated as

$$P = \frac{F}{A_1}$$
 2 – 2

where F was the force applied on the piston. The specific volume change of the LN sample was defined as

$$\Delta V = \frac{A_1 \cdot \Delta l}{m}$$
 2 – 3

where Δl and m were the thickness change of LN sample and the mass of the silica gel, respectively. Part of the ions in the saturated LiCl aqueous solution was trapped in the nanopores during the first loading-unloading cycle, which would affect the second loading-unloading cycles. To remove these residual electrolytes in nanopores, the silica gel samples were separated from the saturated LiCl solution by filtering, thoroughly rinsed by large amount of ethanol and warm DI water, and then dried in air at 80 °C for 48 h. The second pressure-induced liquid infiltration tests were conducted on the recycled nanoporous silica gel-based LN systems. The mass ratio between the nanoporous silica gel and the saturated LiCl aqueous solution was the same.

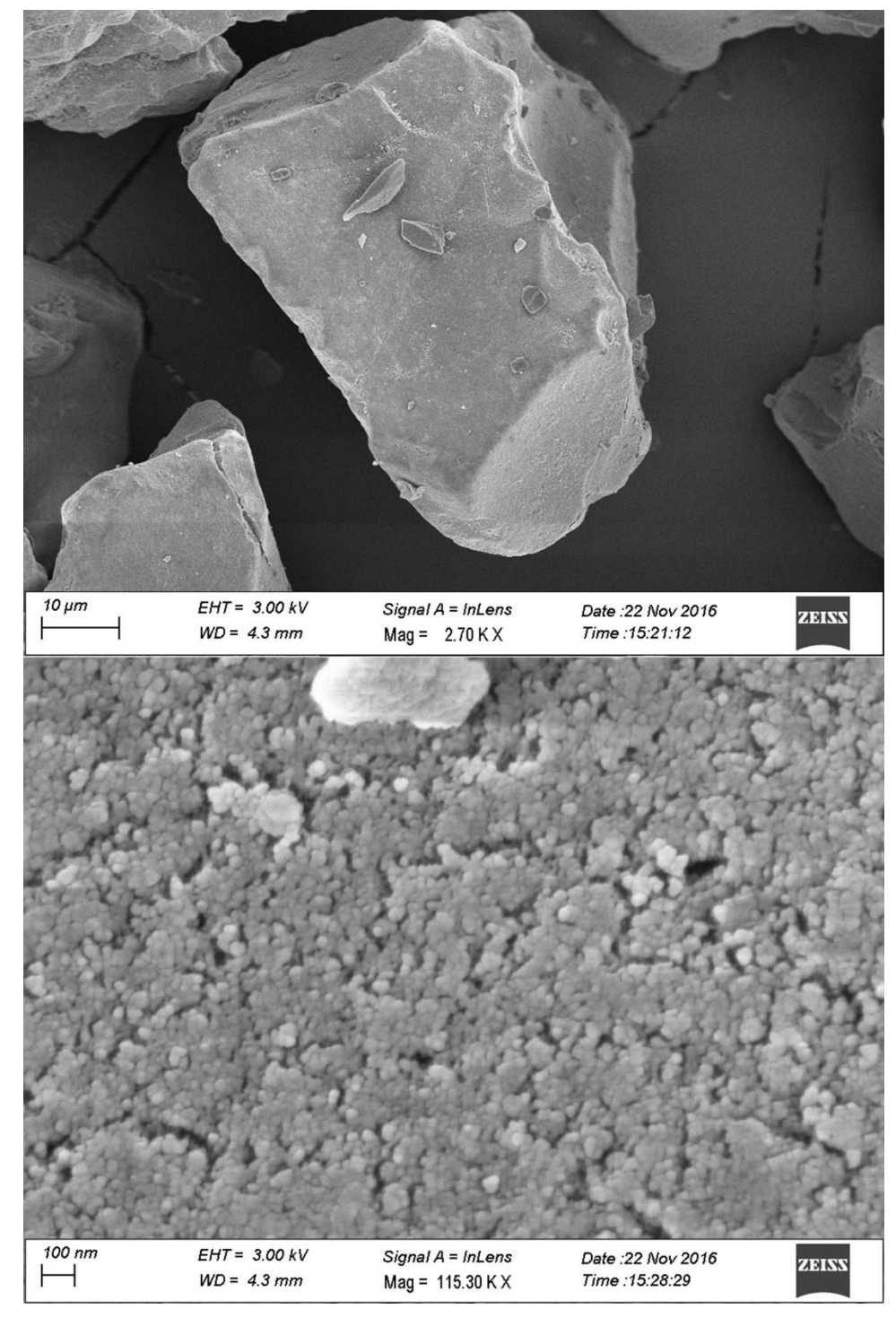


Figure 2-5: SEM photos of the silica gel SG90 containing 3-D nanoporous structure with an average pore diameter of $7.8~\mathrm{nm}$.

The second SN (denoted as SG90) was a nanoporous silica (60759, Sigma-Aldrich). The particle size and average nanopore size of it were 40–63 µm and 7.8 nm [127]. The as-received SG90 had modified surface, which was non-wettable to water. The corresponding liquid phase is DI water.

The same mechanical characterization method was applied on SG90 and SG90-based LN. The peak forces of dry pre-compression applied on silica gel SG90 samples was 3 kN. Thus, the applied peak stress, σ_{max} , was 24 MPa. The peak pressure in pressure-induced liquid infiltration tests was 48 MPa.

2.2.2. Results and Discussion

2.2.2.1.
$$P_{in} > P_{axial}^{cr}$$

Figure 2-6 shows the stress-strain curves of dry pre-compression tests on IR01 silica gels. The observed hysteresis behavior indicates that permanent mechanical deformation including buckling and collapse of nanopores occurred even at the peak stress, σ_{max} , as low as of 2 MPa. Note due to the 3-D porous structures of silica gel IR01 (See SEM photo in Figure 2-3), no radial collapse deformation is expected, that is, P^{cr}_{radial} is too large to be reached in the experiment. Therefore, the deformation at 2 MPa is totally attributed the axial buckling. Thus, $P^{cr}_{radial} \leq 2$ MPa. With the increase of the peak stress, the associated loop area of hysteresis in stress-strain curve increases, and the deformation of nanopores become more severe as more nanopores are permanently deformed. Besides, due to relatively wide pore size distribution in the silica gel (Figure 2-2), no clear elastic to plastic transition was observed in this dry pre-compression tests.

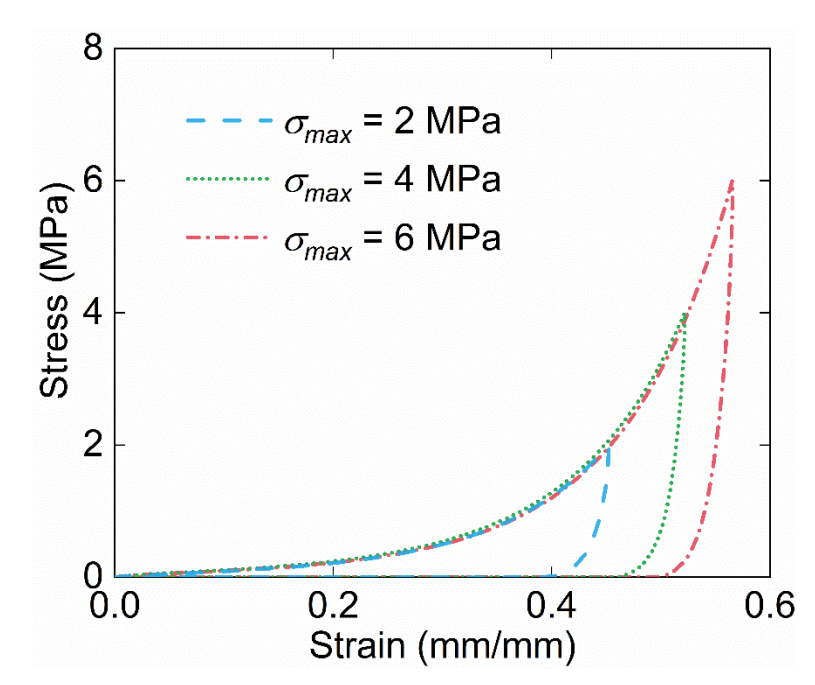


Figure 2-6: Loading history of the dry pre-compression on empty IR01 silica gels under various peak stress σ_{max} .

Pressure-induced liquid infiltration tests on LN systems were conducted with or without dry pre-compression. Figure 2-7 shows the $P-\Delta V$ curves of various IR01-based LN samples. Initially, the liquid did not enter the nanopores due to the surface hydrophobicity of the silica gel, and the porous particles may experience compression or/and bending deformation. As the external pressure reached a critical value, the capillary effect was overcome and the liquid was driven into the nanopores. Consequently, a stress plateau was observed, similar to simulation results in [121]. Once all nanopores were filled, the system became incompressible. The width of the stress plateau reflected the specific nanopore volume of the silica gel specimens, ΔV_{sp} . The liquid infiltration pressure, P_{in} , was defined as the pressure at the mid-point of the stress plateau. For LN system without pre-compression (i.e. $\sigma_{max}=0$), P_{in} was about 2.6 MPa. Therefore, $P_{in}>P_{axial}^{cr}$, high enough to deform nanopores in comparison with the dry pre-compression on particles, yet the liquid was successfully invaded, in consistency with theoretical analysis and MD simulations [121], and ΔV_{sn} was around 1.60 cm³/g. As the pre-compression peak stress σ_{max} increased from 0 to 6

MPa, P_{in} increased from 2.6 MPa to 4.2 MPa, and ΔV_{sp} of corresponding LN decreased from 1.6 cm³/g to 1.10 cm³/g. The results of all liquid infiltration tests were summarized in Table 2-1. The increased P_{in} is in consistency with the liquid infiltration into small pores as the large pores collapsed prior by the dry pre-compression. The decreased ΔV_{sp} also agrees well with the increased collapse volume of nanoporous particles by the applied dry pre-compression in Figure 2-6. P_{in} is smaller than that in simulations due to the larger pores used in experiments.

Table 2-1: $\Delta V_{\rm sp}$ and $P_{\rm in}$ of various IR01-based LN samples.

| σ_{max} (MPa) | $\Delta V_{sp}~({ m cm^3/g})$ | P_{in} (MPa) |
|----------------------|-------------------------------|----------------|
| 0 | 1.60 | 2.6 |
| 2 | 1.45 | 3.2 |
| 4 | 1.30 | 3.4 |
| 6 | 1.10 | 4.2 |

To further confirm the whole process was dominated by liquid infiltration rather than permanent mechanical deformation of nanopores under compression on LN systems, the silica nanoporous particles were collected by filtering out the liquid, then thoroughly rinsed by ethanol and warm DI water to remove the residual electrolytes in the nanopores followed by drying in the air. The recycled silica nanoporous particles were mixed with same amount of saturated LiCl solution and tested under quasi-static compression. The $P-\Delta V$ curves are plotted as the second loading-unloading cycles in Figure 2-7. The liquid infiltration performance of all silica gel samples with different levels of dry pre-compression remained the same, indicating that the nanoporous structures was not further deformed in the first loading-unloading cycle with the presence of the non-wettable liquid. Please note that the silica nanoporous particles have 3-D porous structures, as

shown in Figure 2-3. When suspended in a liquid solution, upon compression, liquid invades in a spatial dimension and no radial collapse deformation is expected.

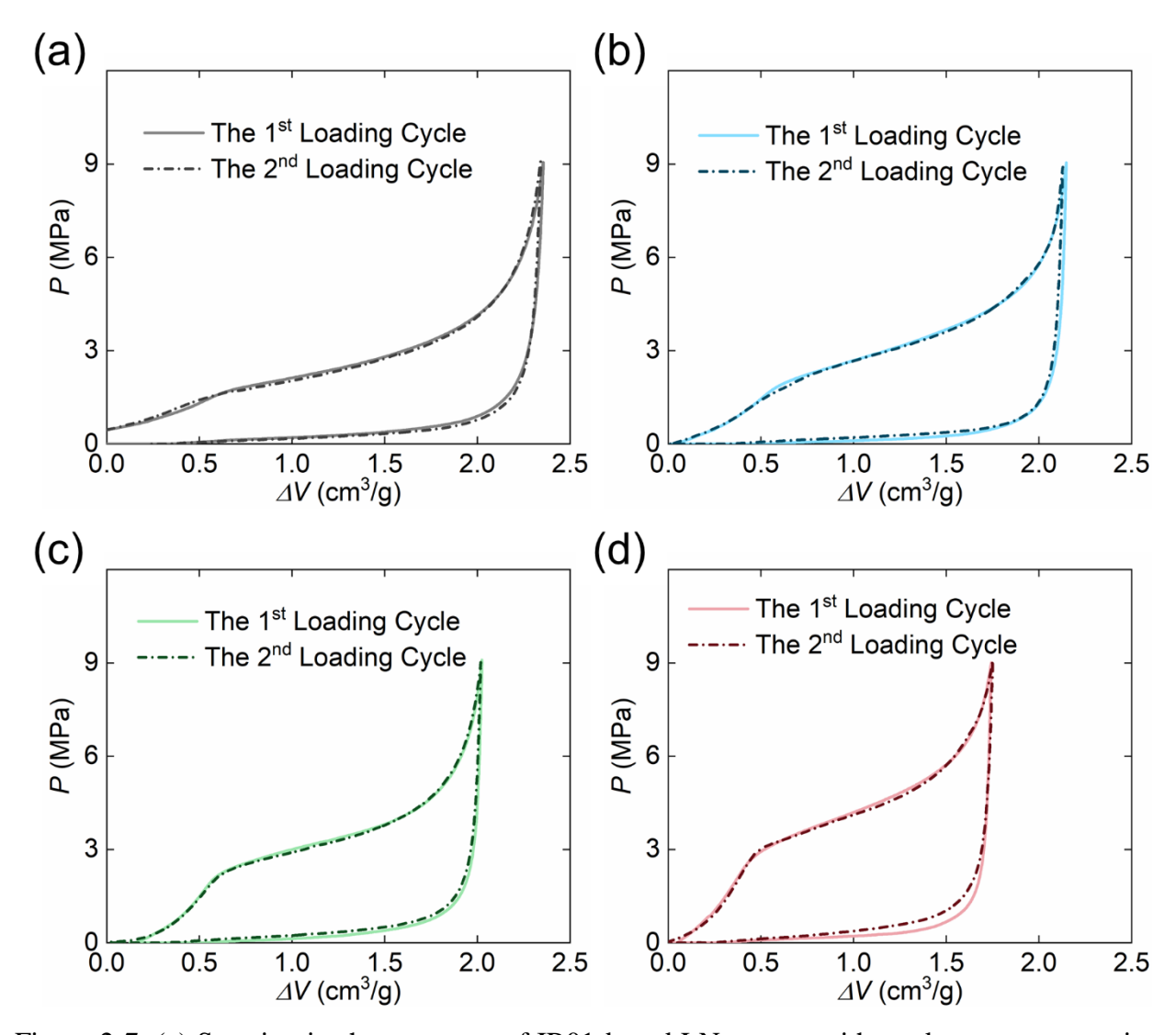


Figure 2-7: (a) Sorption isotherm curves of IR01-based LN system without dry pre-compression (b) Sorption isotherm curves of LN system with dry pre-compression at $\sigma_{max} = 2$ MPa (c) Sorption isotherm curves of LN system with dry pre-compression at $\sigma_{max} = 4$ MPa (d) Sorption isotherm curves of LN system with dry pre-compression at $\sigma_{max} = 6$ MPa. The loading rate for all experiments was 1 mm/min.

So far, we have demonstrated that liquid can invade into nanopore even when the liquid infiltration pressure is higher than the critical axial buckling pressure. The underlying mechanism

is the presence of liquid environment suppresses the axial buckling of nanopores and consequently, the liquid infiltration dominates the deformation process, although $P_{in} > P_{axial}^{cr}$ [121].

2.2.2.2.
$$P_{in} < P_{axial}^{cr}$$

Figure 2-8 shows the stress-strain curves of dry pre-compression tests on SG90 silica gels. The applied peak stress, σ_{max} , was 24 MPa. Figure 2-9 shows the $P-\Delta V$ curves of various SG90-based LN samples. For LN system without pre-compression (i.e. $\sigma_{max}=0$ MPa), P_{in} was about 20 MPa and was around 0.55 cm³/g. As the pre-compression peak stress σ_{max} increased from 0 to 24 MPa, both P_{in} and ΔV_{sp} were exactly the same as those without pre-compression, indicating the pore structure was not damaged. Therefore, the critical axial buckling pressure P_{axial}^{cr} was higher than 24 MPa. Then the quantitative relationship was $P_{in} < P_{axial}^{cr}$. Under this condition, the liquid infiltration plateau can be observed in Figure 2-9, that is, liquid infiltration occurs. Therefore, we have demonstrated that liquid can invade into nanopore when the liquid infiltration pressure is lower than the critical axial buckling pressure.

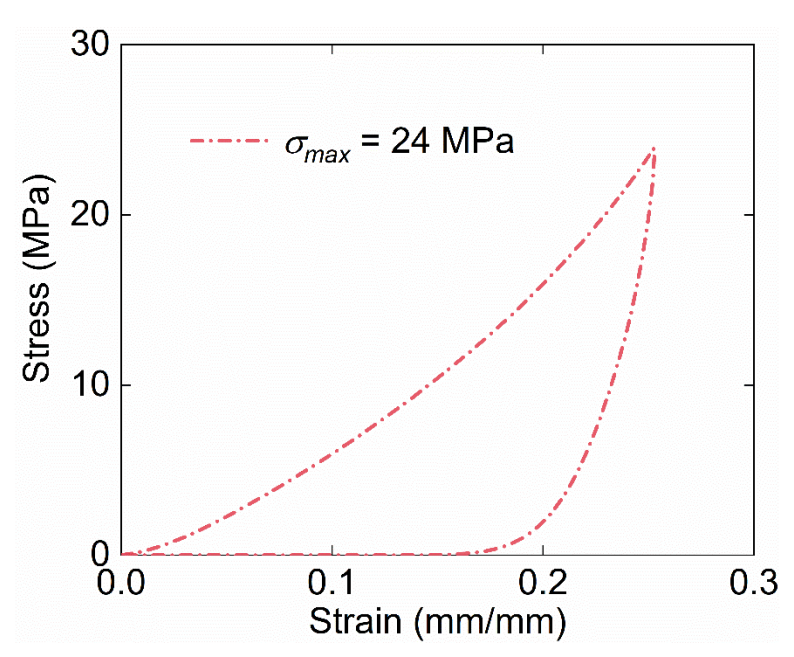


Figure 2-8: Loading history of the dry pre-compression on empty SG90 silica gels under peak stress $\sigma_{max} = 24$ MPa.

2.2.3. Conclusions

In this session, we have demonstrated that liquid infiltration can always happen regardless of the quantitative relationship between the liquid infiltration pressure and the critical axial buckling pressure.

 $P_{in} < P_{axial}^{cr}$: Liquid infiltration happens once P_{in} is reached;

 $P_{in}>P_{axial}^{cr}$: Liquid suppresses the nanopore axial buckling and invades into the nanopores.

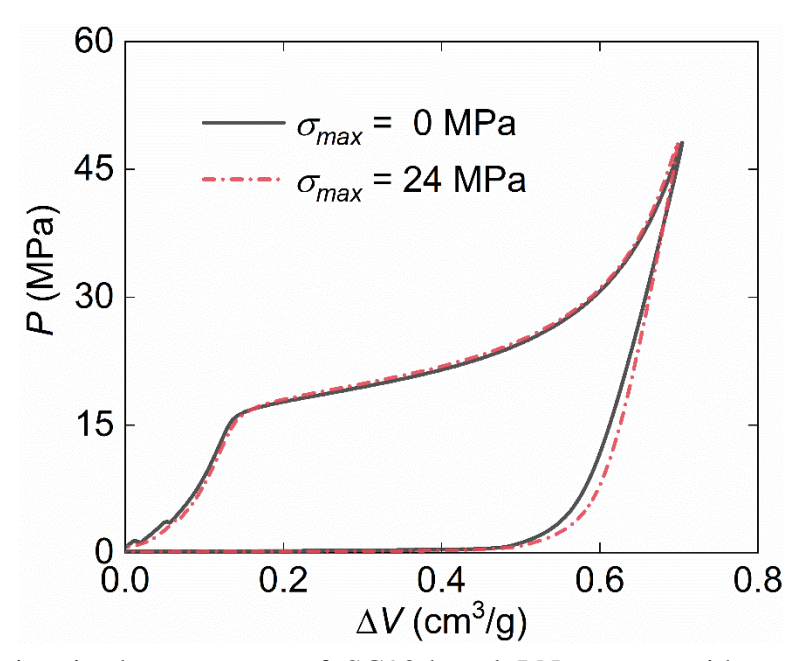


Figure 2-9: Sorption isotherm curves of SG90-based LN system with or without dry precompression.

2.3 Speed Competition

2.3.1. Experimental

Silica gel IR01 was used as the nanoporous material in this session. The SN sample consisting 0.2 g of nanoporous silica was sealed in a stainless-steel testing cell as illustrated in Figure 2-4. Quasistatic compression was applied to the SN sample by a universal tester (Model 5982, Instron, Inc.) at a constant loading speed of 1 mm/min. When the applied force reached 5 kN, the Instron crosshead was moved back at the same rate. The porous structure of nanoporous silica was then examined by pressure-induced liquid infiltration tests. Briefly, after quasi-static compression, the nanoporous silica was collected and mixed with 0.8 g of 46 wt% lithium chloride (LiCl) solution in the testing cell, forming SN-based LN system. The LN was then compressed by the universal tester. Once the force reached 1.9 kN, the crosshead was moved back.

The dynamic behavior of SN sample was investigated using a drop tower apparatus, as illustrated in Figure 2-10. The SN sample was impacted by a 10 kg freely falling drop weight. By

adjusting the free drop heights, dynamic tests were conducted at incident speeds of 1 and 2 m/s. The deceleration history was measured by an accelerometer (353B03, PCB Group, Inc.) and recorded by a PXI oscilloscope (PXIe-5105, NI Corp.) at a sampling rate of 10⁶ s⁻¹. The applied pressure was calculated as

$$P = \frac{m_w \cdot a}{A_1}$$
 2 – 4

where a is the deceleration of drop weight and m_w is the 10 kg drop weight. The displacement of the upper piston was calculated as

$$\delta t = \iint a \tau d^2 \tau \qquad 2 - 5$$

where t and τ are time. After the dynamic tests, pressure-induced liquid infiltration tests were conducted to examine the porous structure of the SN.

The LN sample was prepared by sealing 0.2 g of nanoporous silica and 0.8 g of 46 wt% LiCl aqueous solution in the stainless-steel testing cell. The same quasi-static compression as well as dynamic impact was applied on LN samples. The porous structure of the nanoporous silica was then characterized by pressure-induced liquid infiltration tests.

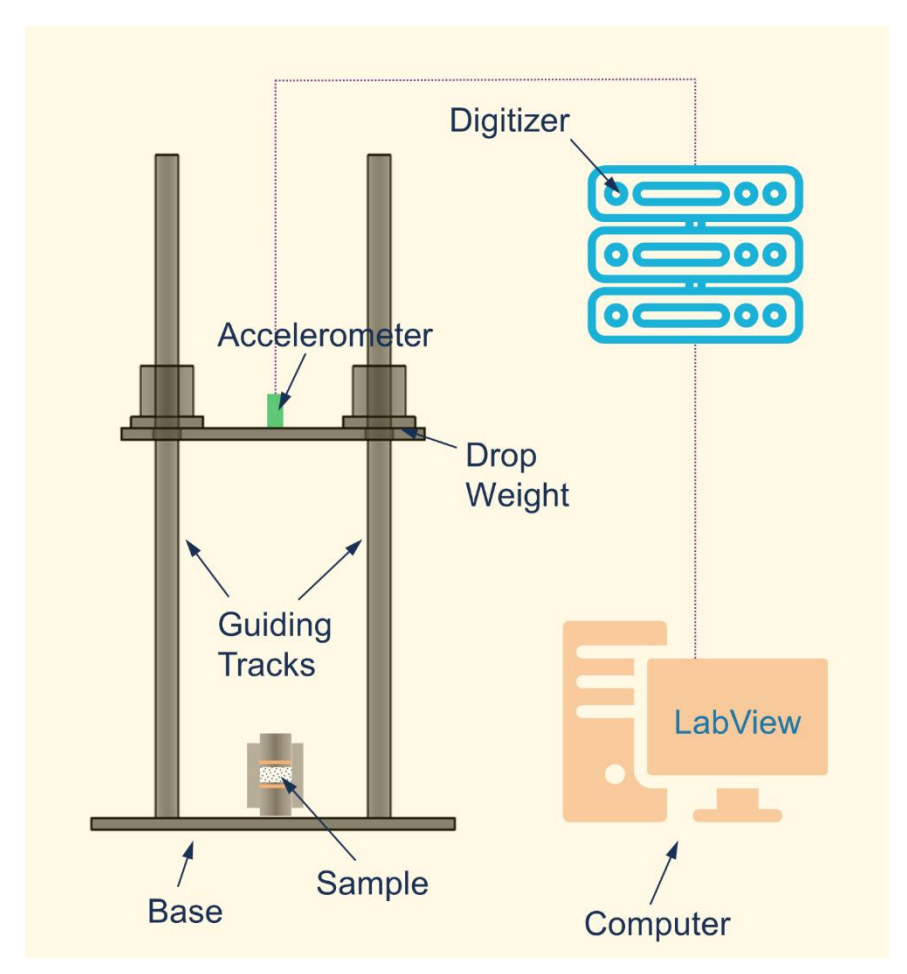


Figure 2-10: Schematic of the experimental setup of dynamic impact test. The drop weight is 10 kg and the sampling rate is 10^6 s⁻¹.

2.3.2. Results and Discussion

Figure 2-11a shows typical stress-strain curves of SN sample subjected to quasi-static compression or dynamic impact. For dynamic impacts, only the loading curves are shown here. The unloading part could not be measured because the contact between drop weight and the upper piston could not be guaranteed when the drop weight bounced back. As quasi-static compression was applied, the strain at peak stress $\sigma_p = 40$ MPa was 0.68. More importantly, the unloading path was quite different from the loading path. The hysteric behavior indicates that the nanopores of the SN undergo permanent deformation including buckling and collapse of the nanopore wall. As the incident speed increased to 1 m/s, the stress-strain curve was higher than that in quasi-static

compression test and the strain at $\sigma_p=40$ MPa was reduced to 0.61, indicating that the SN stiffened as strain rate increased. Thus, the extent of nanopore deformation was reduced, which could be validated by pressure-induced liquid infiltration tests. As a result, the energy absorption efficiency of the SN became lower. As the incident speed increased to 2 m/s, the rate stiffening effect was further pronounced.

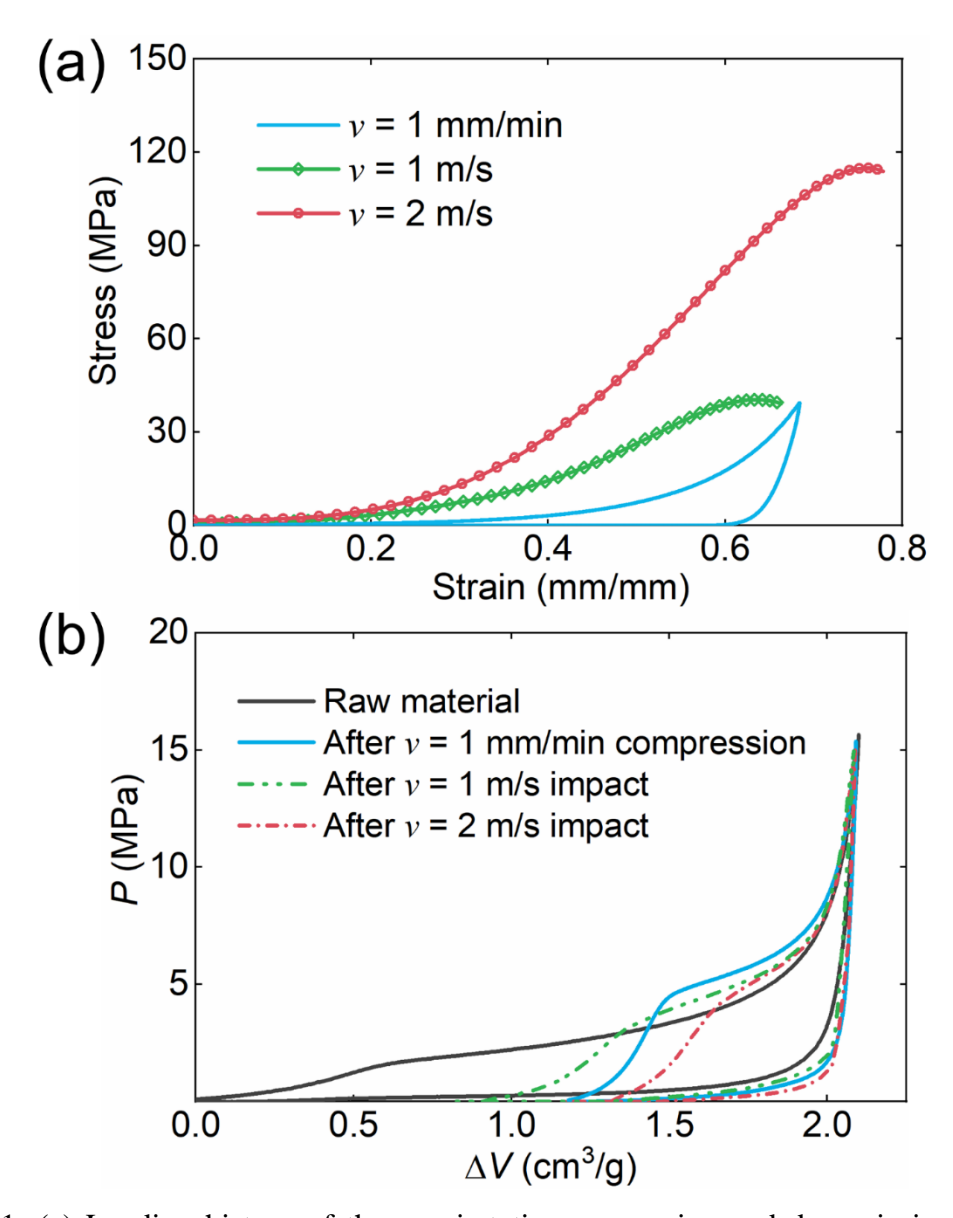


Figure 2-11: (a) Loading history of the quasi-static compression and dynamic impacts on SN sample (b) Sorption isotherm curves of the LN consisting of SN after quasi-static compression or dynamic impact and 46 wt% LiCl aqueous solution.

Figure 2-11b shows typical $P-\Delta V$ curves of various SN-based LN samples. As the SN was mixed with liquid at ambient condition, the liquid did not flow into the nanopores due to the surface hydrophobicity of the SN. When the pressure reached a critical value, i.e. the infiltration pressure P_{in} , the energy barrier caused by the capillary effect was overcome and the liquid was driven into the nanopores. Consequently, an infiltration plateau, where the curve exhibited the smallest slope, was observed. Once all the nanopores were filled with liquid, the system became incompressible. The specific nanopore volume of the nanoporous silica, ΔV_{sp} , can be determined from the width of the infiltration plateau. From Figure 2-11b, the ΔV_{sp} of raw SN was around 1.8 cm³/g. After quasi-static compression, the ΔV_{sp} was reduced to 0.5 cm³/g, which means 1.3 cm³/g of nanopore was crushed or damaged during compression. As the SN was impacted to the same peak stress at 1 m/s, the remaining ΔV_{sp} was around 0.65 cm³/g; that is, the damaged nanopore decreased to 1.15 cm³/g, consistent with the loading history in Figure 2-11a. As the incident speed increases to 2 m/s, more nanopores were damaged due to the increasing incident energy/peak stress. Therefore, only 0.3 cm³/g of nanopores remained after the impact.

The rate sensitive behavior is likely to result from the inertia effect [128–130]. As the SN sample is compressed quasi-statically, the deformation of the nanofoam is in the homogeneous mode, i.e. the stress field is uniformly distributed in the sample. Therefore, once the buckling/collapse stress of the nanopore wall is reached, all these nanopores will undergo permanent deformation. However, as the strain rate increases, the stress equilibrium condition is no longer valid. The local stress builds up quickly at the impact end due to inertia effect. Consequently, only the upper part of the SN is subjected to deformation.

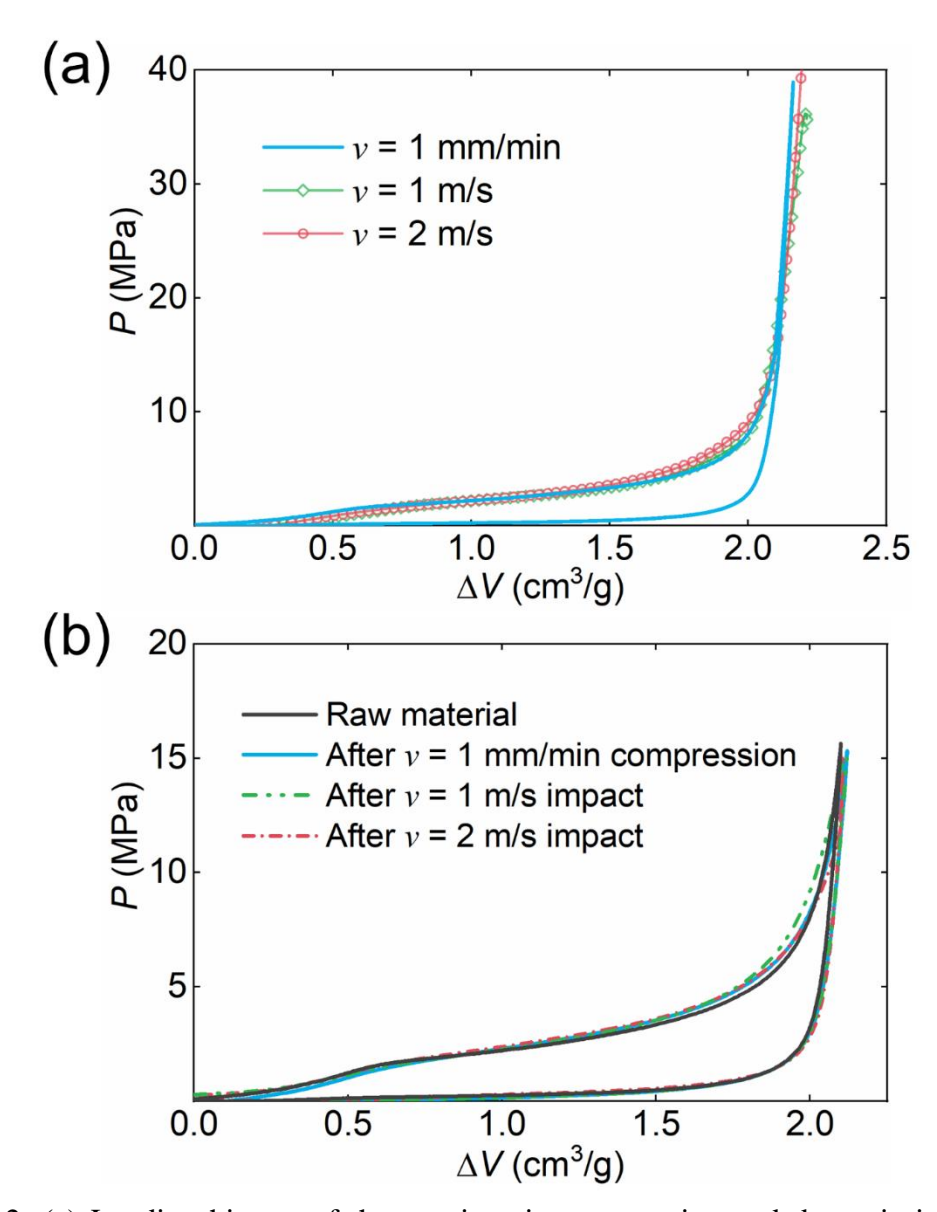


Figure 2-12: (a) Loading history of the quasi-static compression and dynamic impacts on LN sample (b) Sorption isotherm curves of the LN samples after quasi-static compression or dynamic impact.

The LN sample was prepared by functionalizing the SN with aqueous solution. The mechanical behavior was also characterized by quasi-static compression or dynamic impact tests. Typical $P-\Delta V$ curves of various LN are shown in Figure 2-12a. For clarity, only part of the loading curves ($P<40~\mathrm{MPa}$) are shown here. As quasi-static compression was applied, initially, liquid stayed outside the nanopores and the LN showed elastic behavior. As P_{in} was reached, liquid infiltration

occurred, and a stress plateau was observed. As all nanopores were used up, the compressibility of the LN system became zero. Upon unloading, the pressure dropped abruptly and liquid may flow out of the nanopores. The energy absorption capacity of LN can be calculated from the area enclosed by the loading and unloading curves. The nanopore volume as well as the infiltration pressure after compression remained the same as that of raw material as shown in Figure 2-12b, indicating that the nanopore structure was not damaged during the compression test.

More importantly, as the incident speed increased to 1 and 2 m/s, the mechanical response showed almost zero difference from that in quasi-static compression test (Figure 2-12a). Neither the infiltration pressure nor the nanopore volume involved in liquid infiltration was affected by the remarkably increased strain rates. In addition, the nanopore structure was exactly the same as the raw material, as validated by the loading curves in Figure 2-12b. Therefore, the mechanical behavior of LN is strain rate insensitive in this range of loading rates.

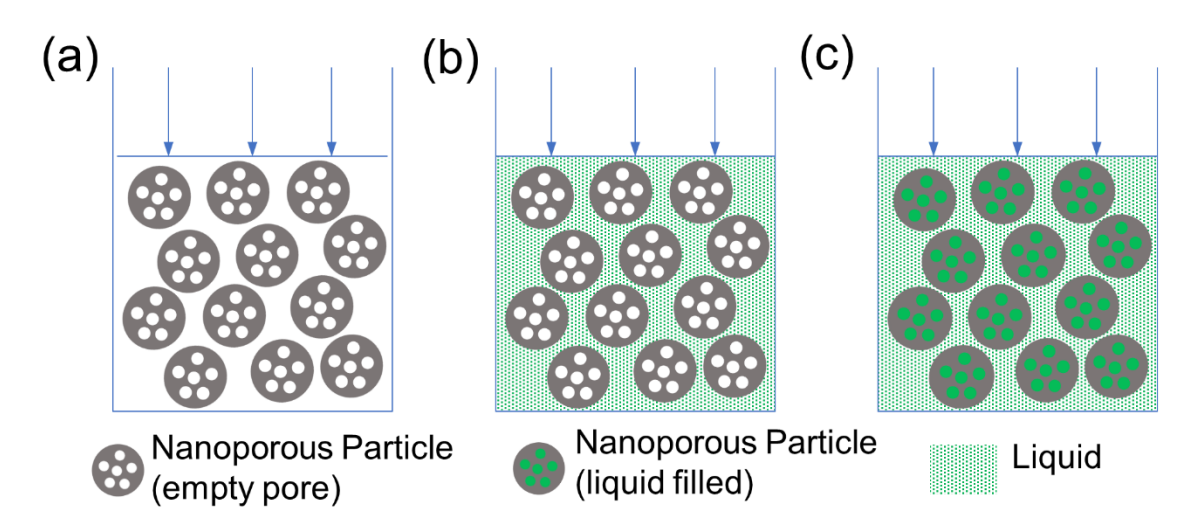


Figure 2-13: Schematic of the sample configuration (a) SN sample (b) LN sample with empty nanopores (c) LN sample with filled nanopores.

Based on the distinct rate sensitivity of SN and LN, two major findings can be generated. Firstly, dynamic localization of crushing caused by the inertia effect can be eliminated by the LN. For SN, upon high speed dynamic impact, the stress equilibrium may not be reached due to the

microscopical heterogeneous configuration (Figure 2-13a). For LN, all the nanoporous particle are surrounded by liquid before the onset of liquid infiltration. Therefore, the applied stress during impact is transformed to homogeneous hydrostatic pressure on LN, as shown in Figure 2-13b; Thus, the stress field is uniformly distributed in the LN and no damage localization will occur.

Secondly, the liquid infiltration speed is higher than the speed of nanopore wall buckling. The initial buckling stress of the nanopore is about 1.5 MPa, comparable to the initial liquid infiltration pressure (~1.6 MPa). Considering these similar initiation stresses, the dominating factor would be the speed. If the liquid infiltration is slower than the nanopore wall buckling, the relatively larger nanopores start to collapse once the critical stress 1.5 MPa is reached. As the impact progresses, more nanopores will be crushed and not involved in the liquid infiltration process. As a result, the LN will show rate dependent behavior and the nanopore volume after impact will be reduced, which is the contrary of our results. Therefore, the liquid infiltration must be faster than the nanopore wall buckling speed. As the LN is impacted, liquid infiltrates into the nanopores before the buckling of nanopore wall. Once the invasion of liquid occurs, the liquid inside the nanopores will provide a strong constraint to the nanopores and suppress the buckling of the nanopores (Figure 2-13c), i.e. the buckling stress of nanopores is significantly increased. Consequently, no nanopore damage will happen, which is consistent with our results. The ultra-fast liquid infiltration speed is attributed to the frictionless flow in the nano-environment [131–134]. As the liquid enters the nanopore, a depletion layer with low concentration of liquid molecules and highly oriented hydrogen bonds would form in between the nanopore wall and liquid. The weak interaction between liquid and nanopore wall and the strong orientation effects of hydrogen bonds leads to a frictionless surface and contribute to the flow rate enhancement.

2.3.3. Conclusions

In summary, we investigated the competition between liquid infiltration and nanopore wall buckling in LN under dynamic impact. Results show that the nanopores in SN are damaged under both quasi-static compression as well as dynamic impact, while the liquid infiltration behavior is rate independent and the nanopores in LN remain the same. The distinct rate sensitivity indicates that the liquid infiltration is faster than nanopore deformation. To the best of our knowledge, this is the first time to validate this and demonstrate that the liquid infiltration mechanism is more efficient than solid cell buckling for energy absorption in high strain rate scenario.

2.4 Summary

In this chapter, we have investigated both liquid infiltration and pore deformation of LN systems under both quasi-static compression and dynamic impact and revealed the fundamental mechanism of competition between liquid infiltration and pore deformation. We have demonstrated that (i) liquid infiltrates into nanopores, independent of the axial buckling stress of the nanopore and (ii) the activation of liquid infiltration as well as liquid flow in nanopores are faster than pore deformation. These findings not only address the fundamental and puzzling question regarding liquid infiltration or pore deformation, but also provides guidance for designing high-performance liquid nanofoam-based energy absorption materials and devices.

Chapter 3

Liquid Flow Speed in Nanopores

The previous chapter demonstrated the speed of activation and liquid flow in nanopores is higher than that of pore deformation, but it did not quantify the actual liquid flow speed in nanopores. This chapter presents an experimental method to characterize the liquid flow in 3D nanopores. We found the effective liquid flow speed in 3D nanopores under dynamic impact was 5 orders magnitude higher than that of the quasi-static loading case. Importantly, the liquid infiltration speed as well as the energy absorption efficiency of the liquid nanofoam (LN) were adaptive to the incident speed and energy level. This provides a mechanistic explanation for the high energy-absorption efficiency of LN at high, blast impact-level, strain rates and demonstrates the importance of experimentally investigating liquid flow behavior in 3D, instead of the traditional 2D, nanopores. The material presented in this chapter was published in *Physical Chemistry Chemical Physics* [126].

3.1 Introduction

The LN system employs liquid flow in nano-environment as its energy absorption mechanism. Liquid flow in nano-environment is the key to many medical and industrial applications, such as drug delivery [135], energy absorption [53,136,137], sensing [58], molecular transportation [138] and many others. Considerably different from bulk phase liquid flow, in nanopores or nano-channels whose sizes are comparable to those of liquid molecules, no continuous liquid phase can be fully developed [139,140]. The confined environment at nanoscale enhances solid-liquid interactions such as hydrophobic repelling, resulting in the breakdown of the non-slip boundary

condition [141]. To characterize fluid flow on the nanoscale, various groups have investigated the liquid flow speed using cylindrical nano-channel (2D) models. Numerically, Huang et al. found an extremely high water transport velocity of 400 m/s in a graphene oxide membrane by Molecular Dynamics (MD) simulation [142]. Experimentally, Majumder et al. reported that the water flow velocity in aligned carbon nanotubes (CNTs) with 7 nm pores is 4 to 5 orders of magnitude higher than that predicted by continuum models [124], while Holt et al. found an enhancement of 2 to 4 orders of magnitude in sub-2 nm CNTs [63], Although these findings have significantly advanced our understanding of liquid flow behavior in the 2D nano-channels with naturally frictionless carbon surface [143] and smaller nanopores (<10 nm), there is a great need to investigate the liquid flow in 3D nanostructured materials in LN system because they involve distinct fluid diffusion characteristics.

To address this, we have examined liquid flow behavior in the LN system, which consists of particles containing 3D nanopores and a non-wettable liquid phase. The mechanical behavior of LN samples at various strain rates and the liquid flow speed in the nanopores have been experimentally investigated. This information is especially important in order to evaluate the potential use of LN under real-life scenarios such as collision, blunt impact and blast waves, and to understand the mechanism of energy absorption at high strain rates.

3.2 Materials and Methods

3.2.1. Material and Sample preparation

The nanoporous silica gel used in this study was an unmodified silica (SP-1000-20, DAISO Co., Ltd). The hydrophilic silica gel surface was converted into hydrophobic by anchoring a thin layer of chloro(dimethyl)octylsilane on the top, as previously reported [144]. After surface treatment, the nanoporous structure of the silica gel was characterized by an AutoPore IV 9500 Mercury

Porosimeter. The LN sample was prepared by sealing 0.18 g of surfaced treated silica gel particles and 0.54 g saturated lithium chloride (LiCl) aqueous solution (46 wt%) in a stainless-steel testing cell with two pistons equipped with O-rings, as shown in Figure 3-1. The cross-sectional area of the pistons, A_2 , was 286 mm². The initial length of the LN samples, l_0 , was 4.5 mm with minimized air content in the testing cell.



Figure 3-1: Stainless-steel testing cell with two pistons equipped with O-rings.

3.2.2. Quasi-static compression test

The quasi-static liquid infiltration behavior of LN was characterized by an Instron 5982 universal tester at a constant loading rate of 2 mm/min (Figure 2-4). The applied force was gradually increased from 0 kN to 4.3 kN, after which the Instron crosshead was moved back at the same speed. The loading-unloading process was repeated for 5 times. The external pressure applied on the LN sample was calculated as

$$P = \frac{F}{A_2}$$
 3 – 1

where F is the force applied by the Instron crosshead. The specific system volume change can be expressed as

$$\Delta V = \frac{A_2 \cdot \Delta l}{m}$$
 3 – 2

where Δl and m are the LN sample thickness change and the mass of silica gel, respectively.

3.2.3. Dynamic Test

The dynamic behavior of the same LN sample was investigated by a lab-customized drop tower apparatus, as shown in Figure 2-10. The LN sample was impacted by a drop weight guided by two vertically aligned tracks. By controlling the free drop heights, the dynamic tests were conducted at various incident speeds of 0.60, 1.25 and 2.60 m/s. Due to the height limit of the drop tower apparatus, 2.60 m/s is the maximum incident speed that we can reach. An accelerometer (353B03, PCB Group, Inc.) was attached to the drop weight to measure its deceleration history which was then recorded by a digitizer (PXIe-5105, NI Corp.) at the sampling rate of 10⁶ samples/s. During all the above tests, the friction between the O-ring and the stainless-steel cell was minimized by lubricant and no liquid leaking was observed. The external pressure applied on the LN sample was calculated as

$$P = \frac{m_w \cdot a}{A_2}$$
 3 – 3

where a is the measured deceleration of the drop weight and m_w is the 3.81 kg drop weight. The displacement of the piston was calculated as

$$\delta t = \iint a \tau d^2 \tau$$
 3-4

Where t and τ are time. The strain rate could be calculated as

$$\varepsilon = \frac{v}{l_0} \tag{3-5}$$

where v is the average incident speed during liquid infiltration.

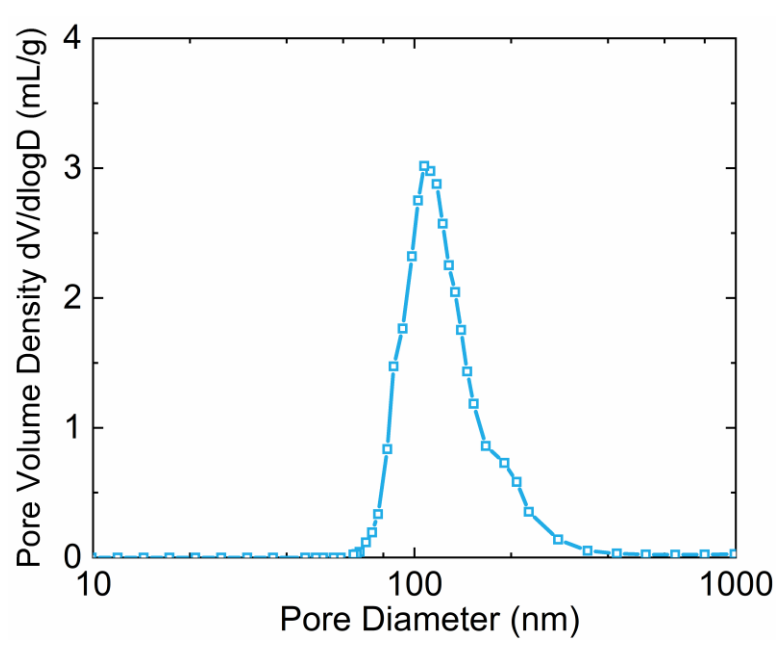


Figure 3-2: Pore size distribution of silica gel. The average pore diameter of the silica gel was measured to be 120 nm.

3.3 Results and Discussion

The nanoporous silica gel used in this study had an average particle size of 20 µm with narrow distribution. After surface treatment, the silica gel surface was grafted with a layer of silyl groups and thus becomes hydrophobic. The average pore diameter and specific pore volume of the silica gel were measured to be 120 nm and 0.76 cm³/g by AutoPore IV 9500 Mercury Porosimeter. The narrow pore size distribution is shown in Figure 3-2.

The quasi-static liquid infiltration behavior was first investigated by a series of pressure-induced infiltration tests at a constant loading rate of 2 mm/min, of which the strain rate is 7.4×10^{-3} s⁻¹. Figure 3-3 shows the representative sorption isothermal curves of the LN samples under quasi-static compression tests. As the sorption isothermal curves of all subsequent cycles are nearly identical to that of the second one, only the curves of first three cycles are shown here. We observed the formation of an infiltration plateau, where the loading curve exhibits the smallest

slope, in the first loading cycle. This corresponds to the liquid molecules being driven into the nanopores when the energy barrier at the solid-liquid interface, i.e. the capillary effect is overcome by the external pressure. This liquid infiltration process is determined by the capillary effect and the transport effect [78]. The transport effect can be neglected, since the average nanopore size of this material (120 nm) is relatively large. Once the liquid molecules enter the nanopore, the effect of nanopore wall on the liquid molecule transportation is only secondary [145]. Thus, the non-zero slope of the infiltration plateau is mainly due to the narrow pore size distribution of the nanoporous particles (Figure 3-3). Once all the nanopores are filled with liquid molecules, the LN system becomes incompressible, as shown by the linear elastic region at the end of the loading curve. The volume associated with the infiltration plateau, i.e. the infiltration volume, is the initial volume of the empty nanopores filled by the liquid molecules. The initial infiltration pressure and the end infiltration pressure of the LN were found to be 0.9 MPa and 4.5 MPa, respectively, in the first loading cycle. They were defined as pressure points at which the loading curve slope changed by 50%. The effective pore volume was found to be around 0.7 cm³/g, as determined from the specific volume change associated with the width of infiltration plateau. The infiltration volume is consistent with the mercury porosimetry analysis result as expected.

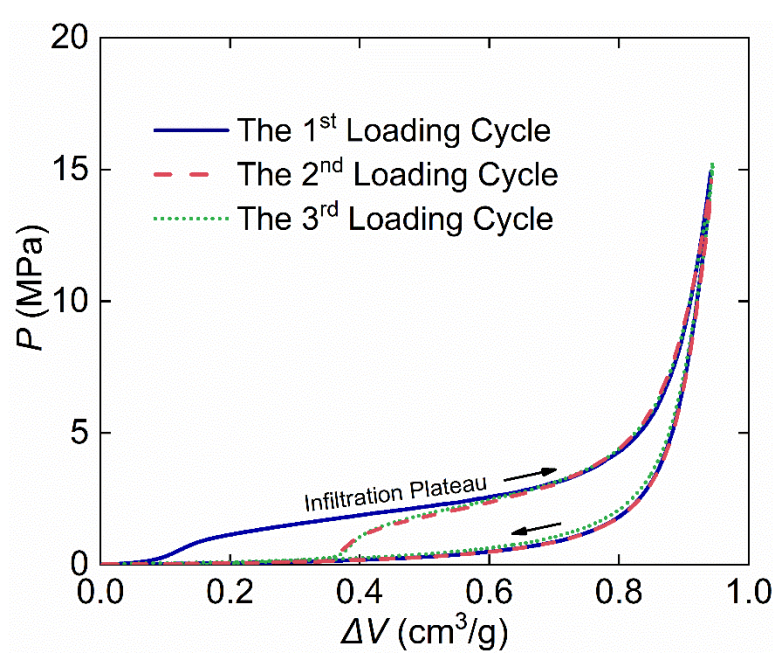


Figure 3-3: Typical sorption isothermal curves of LN samples under quasi-static compression test. The strain rate is 7.4×10^{-3} s⁻¹.

We further demonstrated that in the first cycle, the unloading process could be described as an abrupt pressure decrease followed by liquid defiltration, indicated by the lower pressure plateau of the unloading curve. The initial defiltration pressure of the LN was about 1.5 MPa, defined as the point at which the unloading curve slope decreased by 50%. Although the defiltration volume could not be directly read from the curve, it equaled to the total infiltration volume in the second loading cycle, which was 0.45 cm³/g. The partial defiltration process increased the infiltration pressure to 1.2 MPa for the second and latter cycles. This partial repeatability may have been caused by defective spots in surface treatment, infiltration depth in specific nanopores, pore geometry [146], and the energy barrier of gas-phase nucleation [147]. From cycle two and on, the mechanical behavior of the LN sample is completely repeatable, and thus we conducted all the dynamic tests on the same sample. All the dynamic sorption-isotherm curves were directly compared with the 2nd quasi-static loading curve.

The dynamic behavior of the same LN sample was characterized by a drop tower apparatus at various incident speeds of 0.60, 1.25 and 2.60 m/s. The corresponding strain rates are 1.3×10^2 s⁻¹, 2.8×10^2 s⁻¹, 5.8×10^2 s⁻¹, respectively. The acceleration history of the LN sample at various incident speeds are shown in Figure 3-4. From the acceleration history, the dynamic $P - \Delta V$ loading curves of the LN sample at various incident speeds can be determined as shown in . For clarity, only part of the loading curves (P<15 MPa) are shown here. The unloading curves could not be measured because once the drop weight speed reached 0 m/s, the drop weight bounced back when the contact between the upper piston and the drop weight could not be guaranteed.

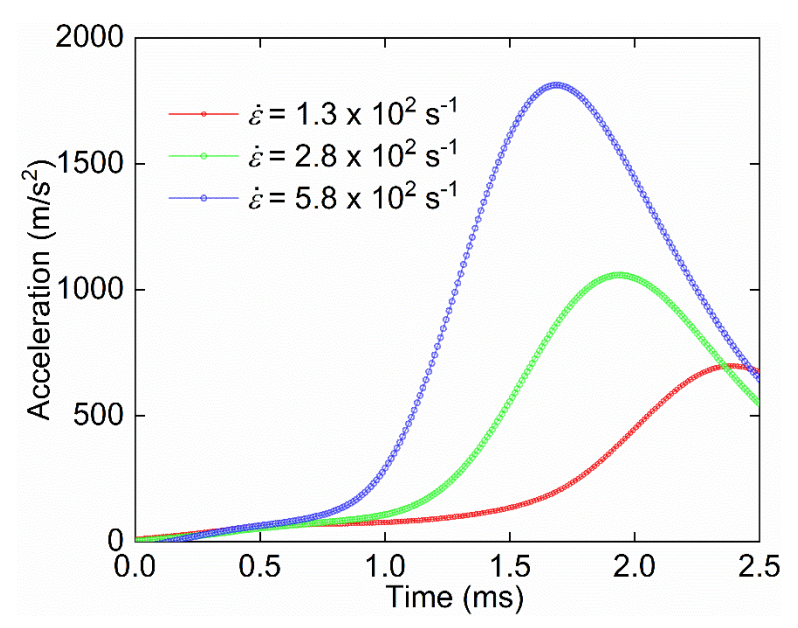


Figure 3-4: Typical acceleration history of LN under dynamic tests at various strain rates of 1.3×10^2 s⁻¹, 2.8×10^2 s⁻¹, 5.8×10^2 s⁻¹.

As shown in Figure 3-5a, although the strain rates of the dynamic tests were 5 orders magnitude higher than that of quasi-static tests, the liquid infiltration process remained the same. Importantly, neither the effective pore volume nor the initial infiltration pressure of the LN was affected by the considerably increased strain rates. As shown in Figure 3-5b, after all the dynamic tests, the mechanical behavior of the LN sample was the same as the second quasi-static cycle. Based on these findings, we can conclude that the liquidinfiltration behavior of the LN is strain rate

independent. Therefore, the dynamic behavior of LN system can be characterized at quasi-static loading conditions.

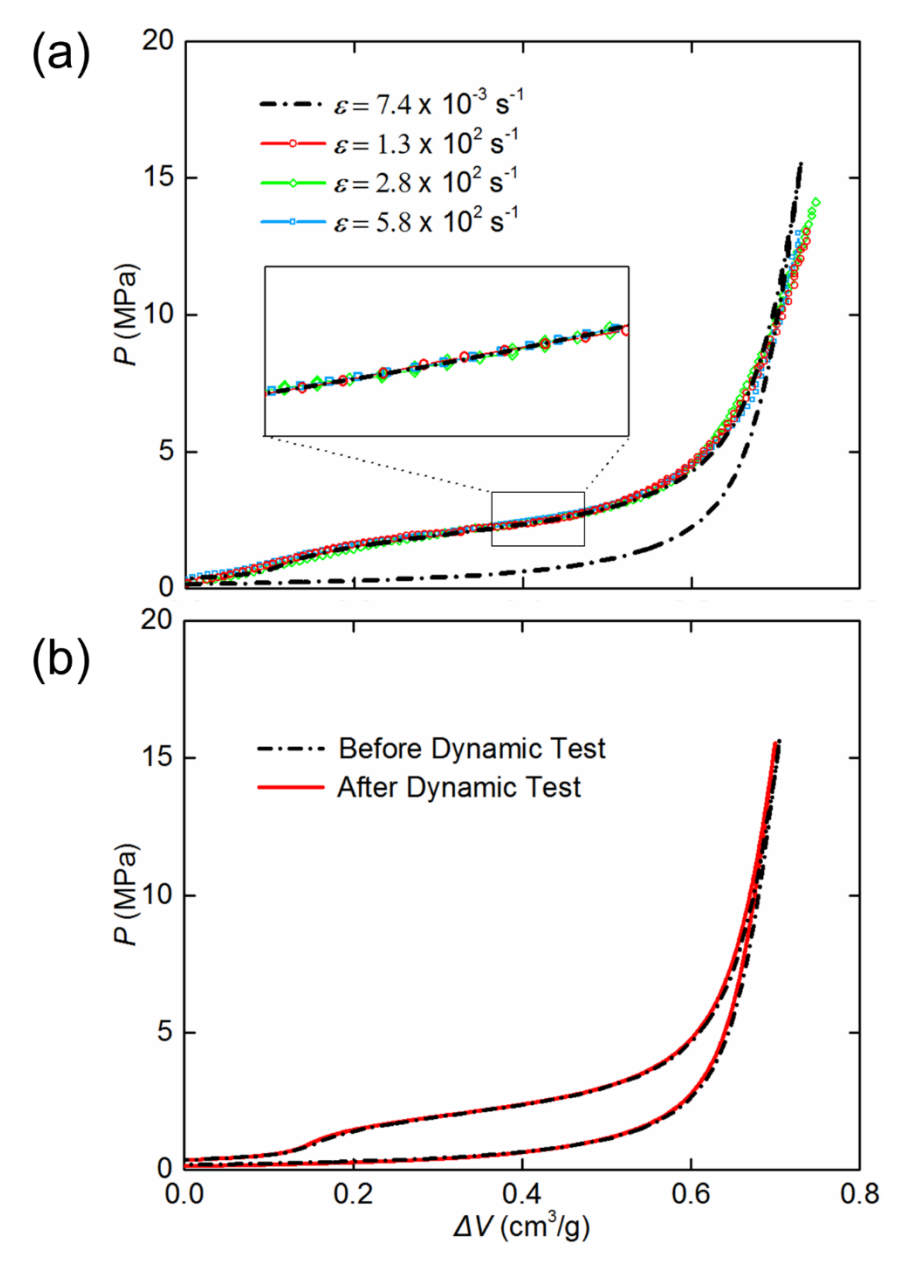


Figure 3-5: Typical sorption isotherm curves of the LN sample (a) under dynamic tests (b) under quasi-static compression tests.

The strain rate independency of the liquid infiltration behavior in LN system, as shown by the observed continuous plateau in the dynamic $P-\Delta V$ curves, indicates that the macroscopic liquid infiltration speed is comparable with and adaptive to the impact speed. Microscopically, in the LN

sample, all surface nanopores on the silica gel particles are exposed to the liquid phase before the onset of infiltration. Once the liquid infiltration is activated, continuous liquid flow takes place in all the surface nanopores simultaneously. It is important to note that the rate independent and repeatable infiltration behavior of the LN also suggest that the energy loss in the infiltration process associated with the flexibility [148–150] and contraction [151] of nanopore walls is negligible. In addition, the nanopore wall becomes more rigid at higher strain rates [152]. Consequently, the energy conservation assumption is satisfied and the macroscopic liquid infiltration speed equals to the accumulative liquid flow speed in all the 3D nanopores. In this way, the effective liquid flow speed in a single nanopore with random 3D configuration and any nanopore size can be directly calculated from the dynamic impact speed on LN system as shown by the simplified model (Figure 3-6).

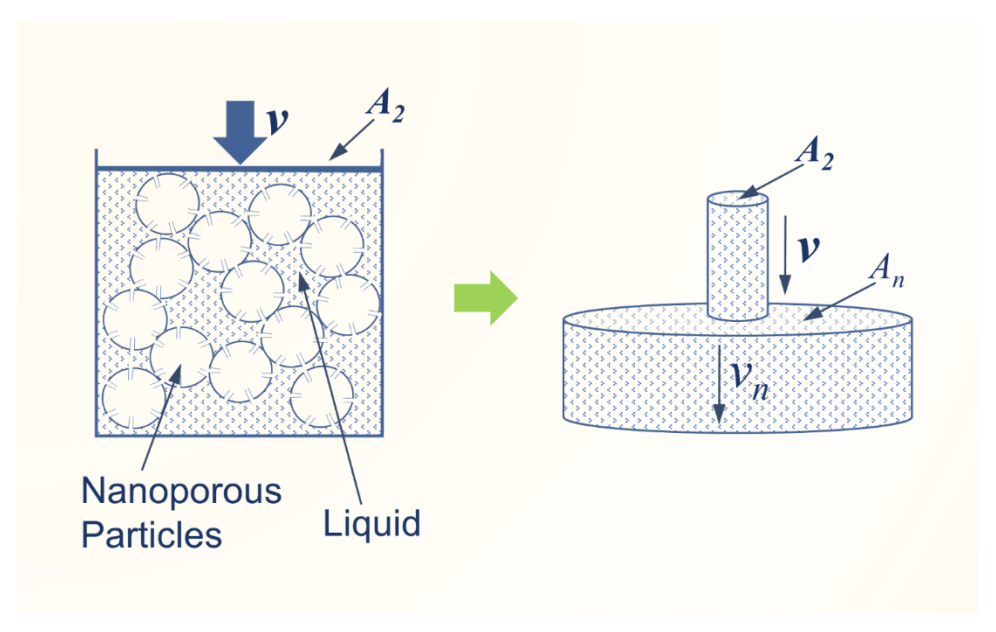


Figure 3-6: Schematic of effective liquid flow in LN sample. All the surface nanopores are accumulated as the total cross-sectional area A_n .

In our model, the total cross-sectional area for the liquid flow in the LN system is the accumulated cross-sectional area of all the surface nanopores. Since the total system volume

change is the same as the volume of liquid molecules infiltrated into the nanopores. The effective liquid flow speed in the nano-channels, v_n , can then be calculated as

$$v_n = \frac{A_2}{A_n}v 3 - 6$$

where A_n is the accumulated cross-sectional area of all the nanopores. A_n can be determined by

$$A_n = \alpha \mathbf{A}^* \cdot N = \alpha \mathbf{A}^* \cdot \frac{V}{V^*}$$
 3 – 7

where α is the ratio of the total cross-sectional area of the surface nanopores to the outer surface area for each silica particle, A^* is the outer surface area of a single particle

$$A^* = 4\pi r^2 3 - 8$$

N is the number of silica particles, V is the total volume of the silica gel and V^* is the volume of a single particle

$$V^* = \frac{4\pi r^3}{3}$$
 3 - 9

The value of α is measured from the surface morphology of a single silica gel particle characterized by a Carl Zeiss EVO LS25 Scanning Electron Microscope (SEM), as shown in Figure 3-7. Due to the different grayscale of voids and silica skeleton, the SEM image can be converted into binary image using the im2bw function in MATLAB. The α of this specific silica gel is 0.29. The average radius of a single particle, r, is 10 μ m. V can be calculated as

$$V = V_{sp} \cdot m_0 = \left(\Delta V_{sp} + \frac{1}{\rho_{SiO_2}}\right) \cdot m_0$$
 3 – 10

where V_{sp} is the specific volume of the silica gel, ΔV_{sp} =0.76 cm³/g is the specific pore volume and ρ_{SiO_2} =2.2 g/cm³ is the density of amorphous solid silica. According to above equations, the

effective liquid flow speed in a single nanopore can be determined. As shown in Table 3-1, the effective liquid flow speed in a single nanopore under quasi-static compression test is only 5×10^{-5} cm/s, while the effective liquid infiltration speed in a single nanopore under dynamic test can reach 3.9 cm/s which is 5 orders of magnitude higher.

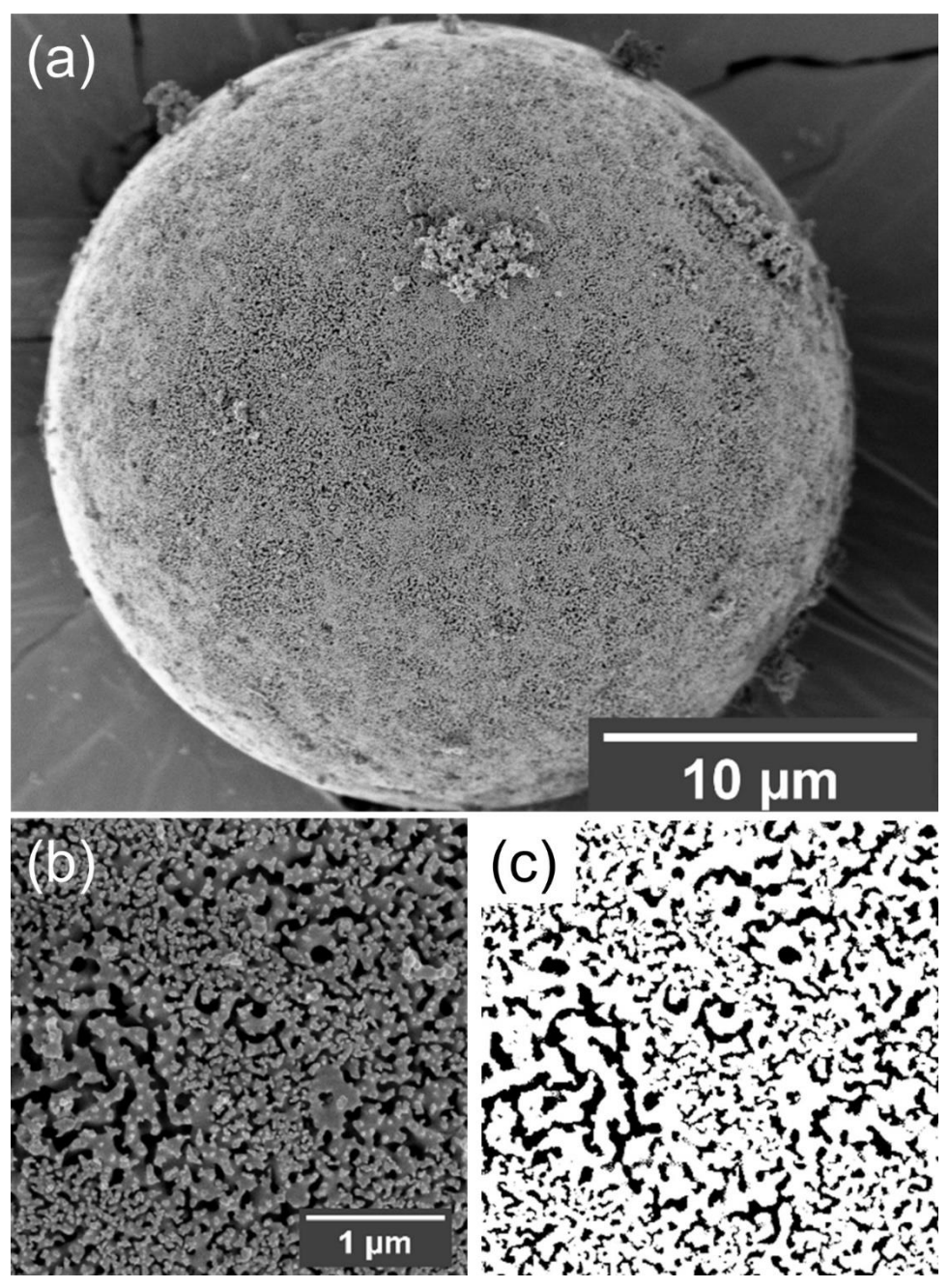


Figure 3-7: Typical SEM image of silica particles (a) Image of a silica particle (b) Image of nanopores (c) Binary image of nanopores.

Table 3-1: Effective liquid flow speed in a single nanopore.

| | Quasi-Static | | Dynamic | |
|------------------------------------|----------------------|---------------------|---------------------|---------------------|
| Strain Rate (s ⁻¹) | 7.4×10 ⁻³ | 1.3×10 ² | 2.8×10^{2} | 5.8×10 ² |
| Effective Liquid Flow Speed (cm/s) | 5×10 ⁻⁵ | 0.9 | 1.9 | 3.9 |

Based on these experimental results, we arrived at two major findings. Firstly, continuum theories are not applicable at the nanoscale even when the pore size is hundreds of nanometers. For a nanopore with pore diameter of 120 nm, the measured liquid flow speed gives a Reynolds number much smaller than 2000, and thus it can be treated as laminar flow [153]. As described by the conventional Hagen-Poiseuille equation, the liquid flow speed is proportional to the pressure difference (ΔP) at the channel ends. In our LN system, ΔP is a constant under various strain rates, but the liquid flow speed is changing dramatically. The considerably enhanced liquid flow speed may be attributed to the "frictionless" flow in the nano-environment. As the liquid molecules enter the hydrophobic nanopore, a low-density depletion layer would form in between the liquid molecules and the nanopore wall [134]. The concentration of liquid molecules as well as hydrogen bond in the depletion layer is much lower than that of the bulk phase. Despite its reduction in number, the hydrogen bonds are highly orientated [131–133]. The ordered hydrogen bonds as well the weak attraction between the hydrophobic nanopore wall and water molecules in the depletion layer contributes to the liquid flow speed enhancement in nanopores. It is also important to note that the rate independent ΔP might appear surprising given the previous finding that high loading rate has a pronounced effect on liquid infiltration due to the periodic energy barriers from the van der Waals (vdW) interactions between unstable liquid molecules and carbon atoms in nanopore wall [80,154]. However, in our previous work [145], we have demonstrated that the liquid infiltration behavior is dominated by the excessive interfacial tension at the nanopore entrance.

Once the liquid molecules enter the nanopore, the effect of nanopore wall on the liquid molecule motion is only secondary. Thus, the overall vdW repulsion as well as shearing stress remain the same, leading to a negligible loading rate effect.

Secondly, the liquid infiltration speed is adaptive to the external impact speed and energy level. As the liquid molecules enter the nanopores, wave energy carried by the liquid molecules will be captured in the nanopores simultaneously. As the strain rate and the kinetic energy of the liquid molecules increase, more wave energy will be trapped in the nanopores, which is the non-dissipative protection mechanism of the LN, namely the energy capture [137,155]. As the loading condition changes from quasi-static compression to dynamic impact, the kinetic energy of the confined liquid molecules increased by 5 orders of magnitude. In other words, the energy capture efficiency of the LN is also adaptive to the external impact speed and energy level. With the combination of the dissipative energy absorption and non-dissipative energy capture mechanisms, the LN system can be more efficient at high strain rates.

3.4 Conclusion

In summary, we developed a streamlined experimental method using the dynamic liquid infiltration behavior of LN as an effective means to characterize the nanoscale liquid flow speed in 3D nanoporous network with random configurations. The measured liquid flow speed in 3D nanopores is 5 orders of magnitude higher than that of the quasi-static loading case. In addition, the liquid infiltration speed as well as the energy absorption efficiency of the LN is adaptive to the incident speed and energy level. Meanwhile, for the first time, we have demonstrated that the dynamic behavior of LN systems can be fully characterized at quasi-static conditions since the dynamic liquid infiltration behavior of LN is independent to the strains rates in a wide range (quasi-static to ~500 s⁻¹). The much-enhanced liquid flow speed in nano-environment and the adaptive

liquid infiltration speed suggest that the energy absorption mechanism of the LN system is more effective at high strain rates. Therefore, LN material systems have the potential to be applied as the next generation of passive protection systems.

Chapter 4

Effect of Sample Structure on Dynamic Behavior of LN

This chapter presents the effect of sample structure on the performance of liquid nanofoam (LN) under dynamic loading conditions. LN samples has been prepared in two different configurations, one with the heterogeneous layered structure and the other with a macroscopically homogeneous liquid marble structure. The mechanical behavior of these two types of LN was examined by quasistatic compression tests and dynamic impact tests. We demonstrated that although both types of LN exhibited comparable quasi-static energy absorption capacity, the liquid marble form of LN showed better performance under dynamic impacts. The material presented in this chapter was published in *AIP Advances* [156].

4.1 Introduction

As discussed previously, LN system is composed of two phases: a hydrophobic nanoporous material which contains large volume fraction of nanometer pores [56], and a nonwetting liquid in which the nanoporous material is immersed. For a single nanopore, it has been demonstrated that the LN system possesses both high energy absorption efficiency and ultra-fast energy dissipation rate [54,88]. However, despite its excellent energy absorbing capabilities under quasi-static conditions, the bulk LN system's performance is limited under dynamic impacts due to its heterogeneity. Naturally, the hydrophobic nanoporous particles cannot be uniformly dispersed into the liquid phase due to their surface property. As a result, in LN samples, the nanoporous particles often aggregate and form separate layers of particles and liquid. In this configuration, the nanoporous particles are not immediately accessible by the liquid phase. As a result, the liquid

infiltration process is much compromised and the energy absorption performance of LN at elevated strain rates is reduced.

To solve this heterogeneity problem of LN, we have converted its structure to the liquid marble form, which is formed when a liquid droplet is brought into contact with and entirely encapsulated by hydrophobic particles spontaneously [157–160]. Vigorous mixing a large amount of liquid with a hydrophobic nanoporous material will result in the formation of a nanoporous particle stabilized LN system, which contains millions of liquid marbles [158,159]. The liquid marble system converts the solid-liquid two-phase system to a macroscopically homogeneous system. We hypothesize that the energy absorption capacity of the LN can be increased by reconfiguration of the material into a liquid marble form.

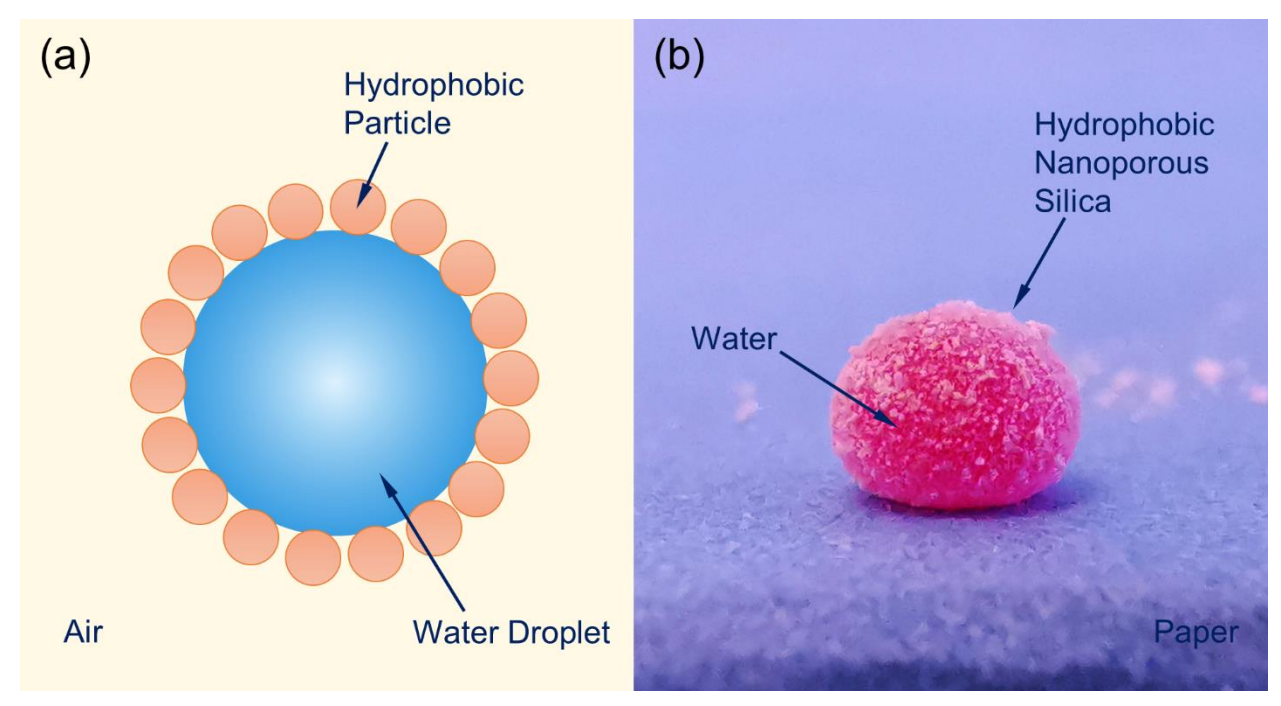


Figure 4-1: Liquid marble (a) Schematic of a liquid marble in which water is stabilized with hydrophobic particles (b) Snapshot of a liquid marble composed of water and hydrophobic nanoporous silica. The diameter of a liquid marble ranges from micron level to millimeter level.

To test this hypothesis, we have prepared the LN sample in two different configurations, one with the heterogeneous layered structure and the other with a macroscopically homogeneous liquid

marble structure. By examining the mechanical behavior of the LN in the liquid marble form as well as the LN in the layered structure at quasi-static and intermediate strain rates, we demonstrate that the liquid marble form possesses a superior energy absorption performance. Therefore, reconfiguration of LN into the liquid marble form offers a promising approach for the protection from blunt impact and the design of next-generation energy absorbers.

4.2 Materials and Methods

4.2.1. Materials and Sample Preparation

Nanoporous silica (SP-1000-20, Daiso Inc.) and saturated lithium chloride (LiCl) solution (46 wt %) were used as the nanoporous material and the liquid phase. The average particle size of the nanoporous silica was about 20 µm. The specific nanopore volume and average pore size were measured to be 0.76 cm³/g and 120 nm respectively by Mercury Porosimeter (AutoPore IV 9500, Micromeritics, Inc.). The nanopore surface of as-received silica gel was hydrophilic; therefore, the aqueous solution could enter the nanopores spontaneously in the ambient environment. Consequently, the deformability of such LN was nearly zero. In order to increase the hydrophobicity of the silica gel, a monolayer of silyl groups was grafted onto the nanopore surfaces [161]. First, 1 g of silica gel was dried at 100 °C and then mixed with 40 mL of anhydrous toluene. The mixture was stirred for 3 h at 90 °C, after which 10 mL of chloro(dimethyl)octylsilane and 1 mL of pyridine were injected into the mixture at room temperature. The surface treatment took place at 95 °C with gentle stirring for 5 h. The treated silica gel was filtered, washed thoroughly with ethanol, and dried at 70 °C in air for at least 24 h before use.

LN samples in two different configurations were prepared for both quasi-static and dynamic tests. The layered LN sample, denoted as LN-L, was prepared by adding 0.2 g of the treated silica gel and 0.6 g of saturated LiCl solution successively. Since the surface of the treated silica gel was

hydrophobic, the silica gel was not wettable to the saturated LiCl solution, and thus the LN sample exhibited a two-layer structure. The LN sample in the liquid marble form, denoted as LN-M, contained same amount of the surface treated silica gel and saturated LiCl solution. After mixing, the liquid droplets were encapsulated by the hydrophobic particles by vigorous agitation. Since no chemical reaction occurs, the chemical composition of LN sample is not affected [158,162]. Therefore, the stability of the LN sample totally depends on the degradation of the silyl layer on the silica surfaces, which can take years or even decades. No property change of both LN samples was observed during the period of this study, i.e. several weeks. For quasi-static compressive tests and dynamic impact tests, both LN samples were sandwiched by two stainless steel pistons equipped with O-rings and sealed in a stainless-steel testing cell (Figure 2-4). The cross-sectional area of the pistons, A_2 , was 286 mm². The initial length of both LN samples, l_0 , was 5 mm.

4.2.2. Quasi-Static Compression Test

The quasi-static compression tests were conducted by a universal tester (Floor Model 5982, Instron, Inc.). The LN sample was compressed at a constant speed of 2 mm·min⁻¹. As the external force gradually increased to 4.3 kN, the crosshead of the Instron machine was forced back at the same rate. The loading-unloading process was repeated for 3 cycles. The applied pressure was calculated as

$$P = \frac{F}{A_2} \tag{4-1}$$

where F was the external force applied by the Instron machine. The specific system volume change was calculated as

$$\Delta V = \frac{A_2 \cdot \Delta l}{m}$$
 4 – 2

where Δl and m were the thickness change of LN sample and the mass of the silica gel, respectively.

4.2.3. Dynamic Impact Test

The dynamic behavior of both LN samples was characterized by a lab-customized drop tower (Figure 2-10). To minimize the friction between O-rings and pistons, during all dynamic tests, vacuum grease was applied on the O-rings as lubricant. The LN sample was impacted by the drop weight at various incident speeds of 0.65 m·s⁻¹, 0.90 m·s⁻¹ and 1.25 m·s⁻¹. The incident speed of dynamic tests was controlled by adjusting the free drop height. The deceleration history of the drop weight was measured by an accelerometer (353B03, PCB Group, Inc.) attached to the drop weight and recorded by an oscilloscope (PXIe-5105, NI Corp.) at the sampling rate of 10⁶ samples/s. No liquid leaking was observed during all tests. The external pressure applied on the LN sample was calculated as

$$P = \frac{m_w \cdot a}{A_2} \tag{4-3}$$

where a was the deceleration of drop weight and m_w was the mass of the drop weight which was 3.81 kg. The thickness change of the LN sample was calculated as

$$\Delta l = \iint a \, \tau \, d^2 \tau \tag{4-4}$$

where τ was time. The strain rate was calculated as

$$\varepsilon = \frac{v}{l_0} \tag{4-5}$$

where \overline{v} was the average speed of the drop weight associated with the liquid infiltration process.

4.3 Results and Discussions

4.3.1. Quasi-Static Behavior of LN

The quasi-static behavior of LN samples with two different configurations, the liquid marble form (LN-M) and the layered form (LN-L) has been characterized by pressure-induced infiltration tests at the strain rate of 6.6×10^{-3} s⁻¹. The liquid infiltration behaviors of both types of LN samples are exactly the same (Figure 4-2). In the first loading cycle, as the applied pressure increases to 0.9 MPa, the slope of the loading curves decreases. The change in slope corresponds to the event that the liquid molecules start to infiltrate into the hydrophobic nanopores. The infiltration pressure is governed by the classic Laplace-Young equation

$$P_{in} = \frac{2\gamma \cdot \cos\theta}{r} \tag{4-6}$$

where γ is the effective solid-liquid interfacial tension, θ is the contact angle, and r is the effective nanopore radius [78]. When the external pressure reaches 4.5 MPa, all the nanopores are filled with liquid molecules, and the slope of the loading curve correspondingly increases dramatically. The loading curve in between 0.9 MPa and 4.5 MPa has the minimum slope and is defined as the liquid infiltration plateau. The specific volume change associated with the liquid infiltration plateau is referred as the infiltration volume with the value of 0.7 cm³/g which is consistent with the pore volume of the silica gel measured by mercury porosimetry. The enclosed area under the hysteretic loading-unloading curve is the energy absorption capacity of the LN samples. The identical behavior of the two types of LN samples suggest that under the quasi-static loading condition, the structure of the LN has no effect on the energy absorption capacity of the material.

At the end of the first loading cycle, a second loading is applied immediately. The initial infiltration pressure increases to 1.2 MPa while the specific volume change associated with the

liquid infiltration plateau decreases to 0.45 cm³/g. Despite the reduction in energy absorption capacity compared with the first loading cycle, the loading-unloading behavior is still hysteretic, suggesting that the LN system is reusable to some extent. This is consistent with our previous results that the nanoporous structure is not damaged in such tests because its strength is an order of magnitude higher than the applied peak pressure [163]. In other words, the nanoporous structure is not crushed, and the liquid infiltration is the main working mechanism for energy absorption.

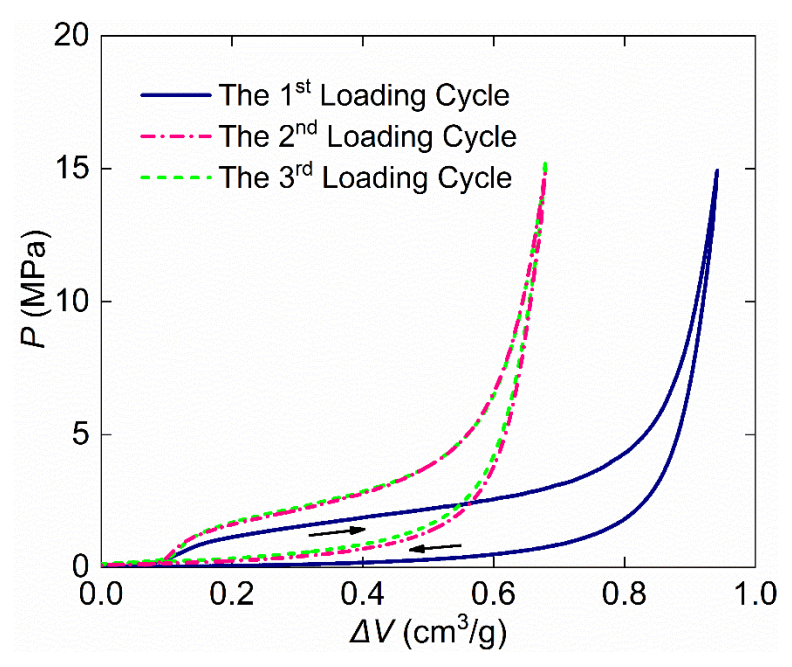


Figure 4-2: Typical sorption isothermal curves for both LN samples under quasi-static compression test.

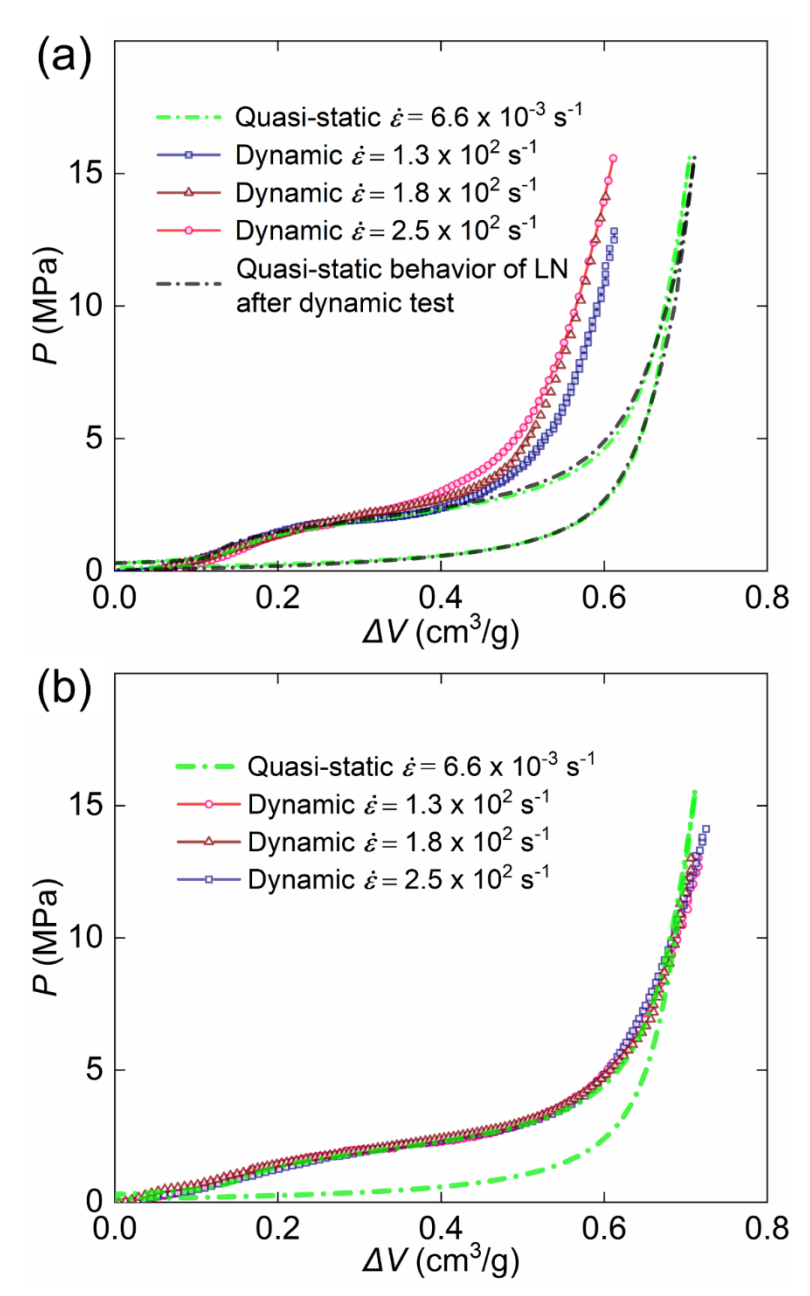


Figure 4-3: Typical dynamic loading curves of LN samples. (a) The LN-L sample (b) The LN-M sample.

From the second loading cycle on, the LN samples do not exhibit further reduction in energy absorption capacity, i.e. the LN samples are fully reusable, as suggested by the overlapped loading-unloading curves between the second and the third cycles (Figure 4-2). This property eliminates the need of using a new sample for each dynamic test and allows us to use one pre-compressed LN sample (i.e. sample after the first loading-unloading cycle) throughout the tests.

4.3.2. Dynamic Behavior of LN

The dynamic behavior of the LN samples with both configurations was characterized at strain rates of 120 s⁻¹, 180 s⁻¹, and 250 s⁻¹. During unloading, the drop weight bounced back faster than the upper piston, that is, the thickness change of the LN sample upon unloading cannot be captured. Therefore, only the loading curves of the dynamic tests are recorded (Figure 4-3).

The dynamic infiltration behavior of the LN-L sample is strain rate sensitive as its deformability shows a remarkable decrease at elevated strain rates (Figure 4-3a). When the strain rate is 120 s⁻¹, the specific volume change associated with the liquid infiltration plateau is 0.35 cm³/g, which is 78% of that in quasi-static tests. As the strain rate further increases to 250 s⁻¹, the deformability of the sample decreases to 0.28 cm³/g, which is 62% of the full energy absorption capacity of the LN. Despite the change in the system deformability, the infiltration pressure range (0.9~4.5 MPa) is not affected by the increased strain rates. After all the dynamic tests, the LN-L sample is compressed under quasi-static compressive loading for one more cycle. The liquid infiltration performance is exactly the same as the one before dynamic impacts (Figure 4-3a). In contrast to the reduction in energy absorption capacity of the LN-L sample, the dynamic behavior of LN-M is strain rate insensitive (Figure 4-3b). Both the total deformability as well as the liquid infiltration pressure range remain the same as measured in the quasi-static compression test. These results suggest that the LN-M sample is more efficient than the LN-L sample at increased strain rates, and the energy absorption capacity of the LN is fully activated in its liquid marble form.

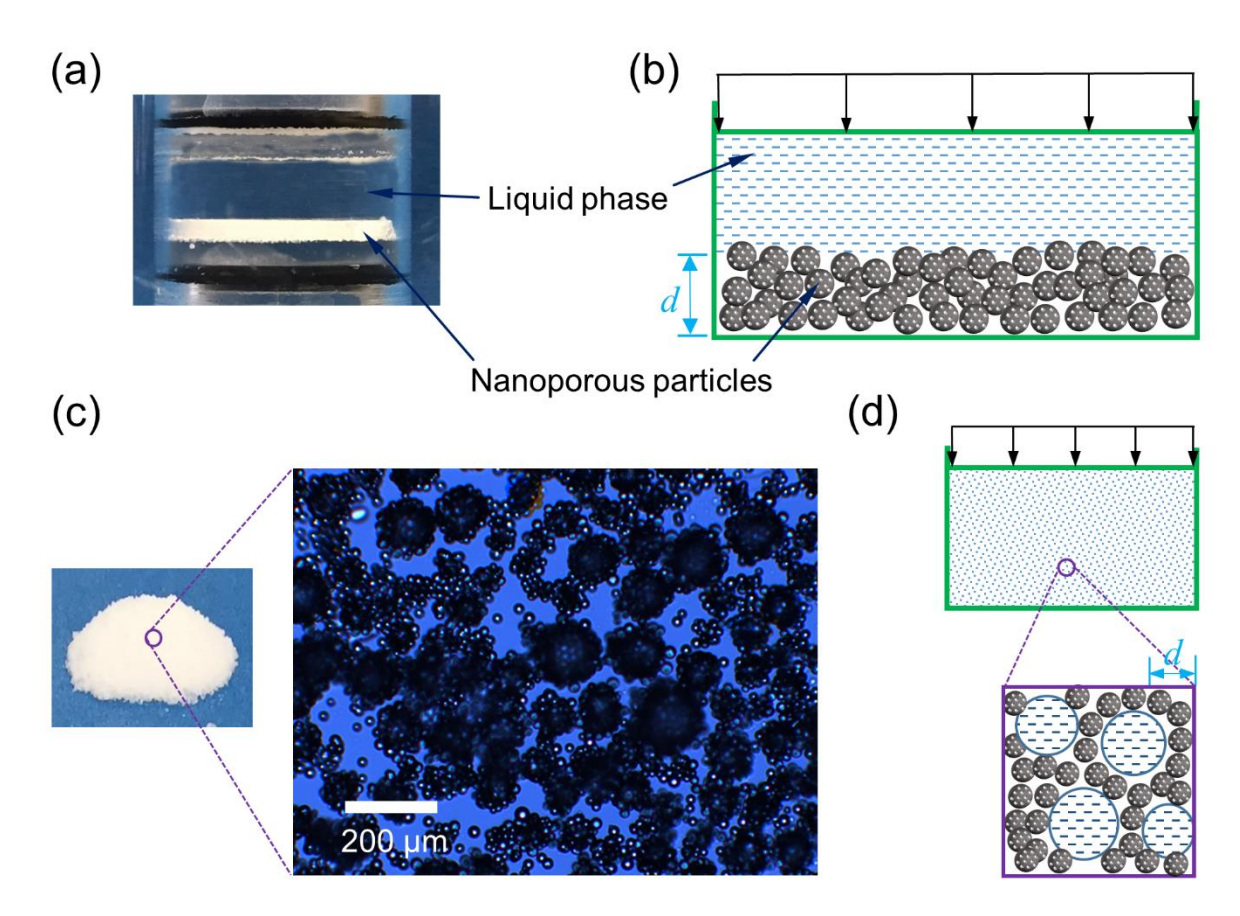


Figure 4-4: (a) Snapshot of LN-L sample (b) Schematic of LN-L sample structure (c) Snapshot and microscopy image of LN-M sample (d) Schematic of LN-M sample structure.

4.3.3. Effect of Sample Structure

The only difference between LN-L and LN-M is the sample configuration (Figure 4-4). The LN-L sample contains two layers, one liquid layer and one hydrophobic silica gel layer (Figure 4-4a and Figure 4-4b). The distance between the nanopores and the liquid phase, d, increases from zero to several millimeters as the depth of the silica gel layer increases. In comparison with the heterogeneous layered structure of LN-L, the LN-M sample has a macroscopically homogenous structure and the maximum value of d is only a few microns (Figure 4-4c and Figure 4-4d). As the LN samples are loaded quasi-statically, there is sufficient time for the liquid to reach the nanopores' open ends; that is, all the nanopores are accessible before the liquid infiltration starts. As a result,

the liquid is driven into all the nanopores and both LN samples exhibit the same quasi-static infiltration behavior and energy absorption capacity.

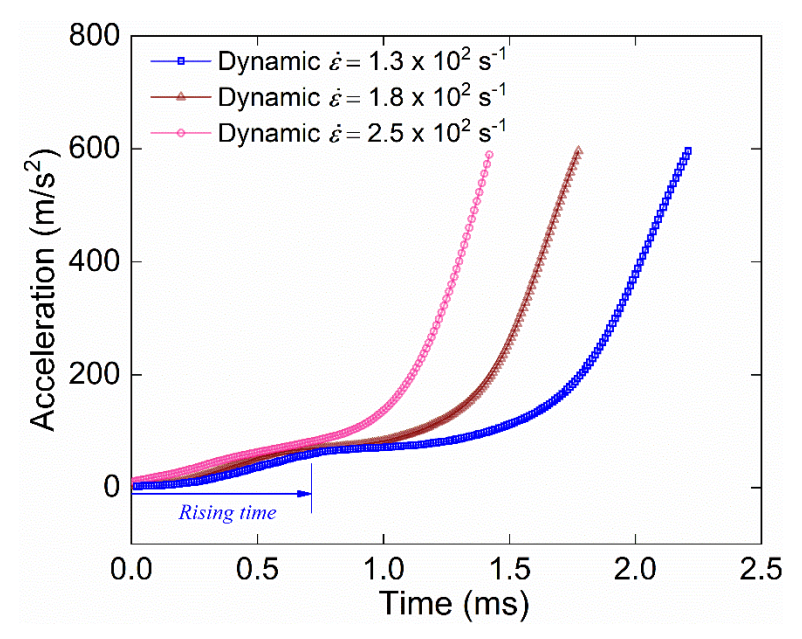


Figure 4-5: Typical acceleration history of LN-L sample under dynamic impacts. The rising time is defined as the time from the initiation of external impact to the beginning of liquid infiltration.

By contrast, under dynamic impact, the complete external loading cycle lasts only a few milliseconds and the rising time of the external loading from zero to 1.2 MPa, t_r , is less than millisecond (Figure 4-5). During the loading process, the minimum activation time, t_0 , needed for the liquid to reach all the open ends of nanopores in the LN-L sample is equivalent to the time need for the liquid to completely fill the air gaps between the hydrophobic particles. It is estimated as

$$t_0 = \frac{1 - f \cdot d_{max}}{v} \tag{4-7}$$

where f is the volume fraction of the silica gel and d_{max} is the initial thickness of the silica gel layer.

In the LN-L sample, d_{max} is 3 mm. If the particles are closely packed (the actual volume fraction of the particles is much lower due to the hydrophobic surface property and structural randomness), f is 74%. As the LN-L sample is impacted at 0.65 m·s⁻¹, the minimum required activation time is

about 1.2 millisecond, which already exceeds the rising time of the external loading. Since both the rising time of the external loading and the minimum required activation time of LN-L are proportional to $1/\bar{v}$, $t_0 > t_r$ at all impact speeds. Consequently, only part of the nanoporous silica gel particles is involved in energy absorption under intermediate strain rate.

The assumption of the above calculation is that liquid infiltration is not activated before all the air gaps are filled by the liquid phase. However, at higher strain rates, the stress equilibrium condition which is always satisfied under quasi-static tests, is no longer valid and the local pressure at the impact end builds up first due to the inertia effect caused by the heterogeneous configuration [129,130,164]. As the nanoporous particles at the top of the silica gel layer have immediate contact with the bulk liquid phase, liquid infiltration process is activated and finished locally before the liquid fills all the air gaps. As a result, there is 78% of the nanoporous silica gel involved in the energy absorption (Figure 4-3a). As the incident speed increases, the inertia effect is more significant, and less nanopores are activated during the loading process. Therefore, the energy absorption capacity of the LN-L further reduces to 62% (Figure 4-3a).

In the LN-M sample, the size of the air gaps between the liquid phase and the nanoporous particles, d, is reduced from millimeters to microns by the macroscopically homogeneous configuration (Figure 4-4b). As a result, the LN-M sample is fully activated after all the air gaps are filled by the liquid phase in less than 0.01 millisecond which is calculated as t_0 . The activation time of the LN-M sample is two orders of magnitude lower than the rising time of the external impact, which also mitigates the inertia effect. Therefore, all the nanopores are exposed to the liquid phase immediately and involved in the liquid infiltration process under impact. The energy absorption capacity of LN is fully activated at different strain rates ranging from quasi-static to 10^2 s⁻¹ in the liquid marble configuration.

4.4 Summary

To summarize, the liquid infiltration behavior of LN samples with two different sample configurations, the layered form and the liquid marble form, has been characterized by quasi-static compression tests and drop tower tests. The infiltration behavior and energy absorption capacity under quasi-static compression are the same for both configurations. However, under dynamic tests, the layered form LN shows a reduced deformability as well as energy absorption capacity, which is attributed to a long activation time and inertia effect due to the heterogeneous structure. By contrast, in the liquid marble form of LN, the nanoporous particles and liquid droplets are uniformly distributed and all the nanopores are accessible upon impact, leading to the ultra-fast reaction of the LN. Therefore, the overall liquid infiltration behavior of the liquid marble form LN sample is not affected by the considerably increased strain rate. These findings suggest that the LN in the liquid marble form can perform as an efficient energy absorption system under blunt impact.

Chapter 5

LN-Functionalized Thin-Walled Structure – Small-Scale

This chapter presents the reinforcement effect of liquid nanofoam (LN) on small scale thin-walled tubes. LN was employed as a novel filling material in thin-walled tubes, creating a liquid–solid "interfacial bonding". The crushing behavior of LN-filled tube (LNFT) has been characterized by quasi-static compression and dynamic impact tests. Results show that the strengthening coefficient of the LNFTs was 3.8, much higher than that of best solid foam-filled tubes. The improved reinforcement effect indicates that the filler-tube wall interaction is much enhanced at the liquid-solid interface, which demonstrates the "perfect bonding" between LN and the tube wall. These findings provide new concepts in designing novel composite materials and structures. The material presented in this chapter was published in *Composite Structures* [165].

5.1 Introduction

Interfacial bonding is of fundamental importance to the performance of composite materials and structures, such as fiber reinforced polymeric composites [166], laminated composite structures [167,168], honeycomb sandwich structures [169], hydrogel-elastomer hybrid materials [170], among others. Tailoring the interfacial bonding between different components in the composites provides exquisite control of their mechanical [171], thermal [172], electrical [173] properties and environmental stability [174]. In particular, interfacial bonding between the tube wall and the filler material in foam-filled thin-walled tube plays an important role in its crushing performance. Thin-walled tubes have been widely used as energy absorbing devices in crashworthiness applications due to their light weight, low cost and high energy absorption capacity [14,15]. To improve the

mechanical properties and energy absorption capacity of thin-walled tubes, researches have been focused on reinforcing the empty tube by metallic foam fillers [24,27,29,30,175,176]. Santosa et al. [177] investigated the reinforcement effect of interfacial bonding by numerical simulations and found that the presence of adhesive bonding can increase the average post-buckling strength of foam-filled tubes by enhancing filler-tube wall interaction. Furthermore, they experimentally demonstrated that the foam strengthening coefficient increased from 1.8 to 2.8 as the adhesive was applied [178], which was further confirmed by Toksoy et al. [25] and Bonaccorsi et al. [26].

The interfacial bonding between the foam and the tube wall can be achieved by two different methodologies, either by applying an adhesive or by direct foaming inside the hollow tube. Although adhesive can create bonding at the interface, the curing process is either time-consuming [25,178] or require additional heat treatment [179]. Direct *in situ* foaming can facilitate the formation of interfacial bonding during the foaming process. However, the performance of the filled tube has large variation due to poor quality control and process-induced structural defects [26]. Importantly, the interfacial bonding created by both methods inevitably contains imperfections, leading to a lower post-buckling strength of foam-filled tubes than theoretical value [177].

Another promising method to produce interfacial "bonding" between the filler and the tube wall is to employ liquid fillers. Due to their intrinsic high fluidity, liquids fit well with the tube wall shape, resulting in "perfect bonding" at the liquid-solid interface. Consequently, the filler-tube wall interaction can be stabilized, and the tube wall is reinforced during the complete deformation process. However, as most liquids are nearly incompressible, the reinforcement effect will be at the cost of total deformability of the system.

In the last decade, a highly compressible liquid-based system, liquid nanofoam (LN), was developed for high-performance of protection [85,156,161,180–182]. In the LN, hydrophobic nanoporous particles are dispersed in a non-wettable liquid phase. Due to the capillary effect, the hydrophobic nanopores remain empty at ambient condition. As sufficient load is applied, the capillary resistance is overcome and the liquid molecules are forced into the nanopores. Due to the ultra-large surface area of nanoporous materials, tremendous amount of energy can be absorbed [56]. Given these advantages, LN is a promising filler for thin-walled tubes. Recently, a few investigations have been conducted with regard to the quasi-static [183,184] and dynamic [185] behaviors of LN-filled tube (LNFT). However, the dominant reinforcing mechanism, e.g. the liquid-solid interaction between LN and the tube wall, remains unclear. In this study, we systematically examine the underlying mechanism of the strengthening effect of the LN on thin-walled steel tubes. We experimentally demonstrate that "perfect bonding" between the LN and the tube wall leads to much enhanced liquid-solid interaction. We also validate that the liquid-solid interaction increases the strain rate sensitivity of LNFTs under dynamic impacts.

5.2 Materials and Methods

5.2.1. Materials and Sample Preparation

The thin-walled stainless steel tube (304F10500X006SL, MicroGroup) used in this study had outer diameter (D), wall thickness (t) and height (h_0) of 12.7 mm, 0.15 mm and 25.4 mm, respectively. The thin-walled stainless steel tube was filled with different fillers, i.e. water or LN. The water-filled tube was prepared by completely filling the tube with deionized water, while the LNFT was filled with a pre-compressed LN to minimize the amount of air bubbles trapped in the LN. After filling, the steel tubes were sealed by two metal endcaps using epoxy adhesive (50112, J-B Weld). Figure 5-1 shows a representative LNFT sample. The effective height of the tube between the two

endcaps (h) was 20.3 mm. During all experiments, no liquid leakage was observed before tube wall burst. Empty steel tube sealed by the same endcaps was used as reference.

The LN used in current study contains a nanoporous silica and DI water. The nanoporous silica (60759, Sigma-Aldrich) was denoted as SG90 (See SEM photo in Figure 2-5). The particle size and average nanopore size of it were 40-63 µm and 7.8 nm [127], respectively. The as-received SG90 had modified surface, which was non-wettable to water.

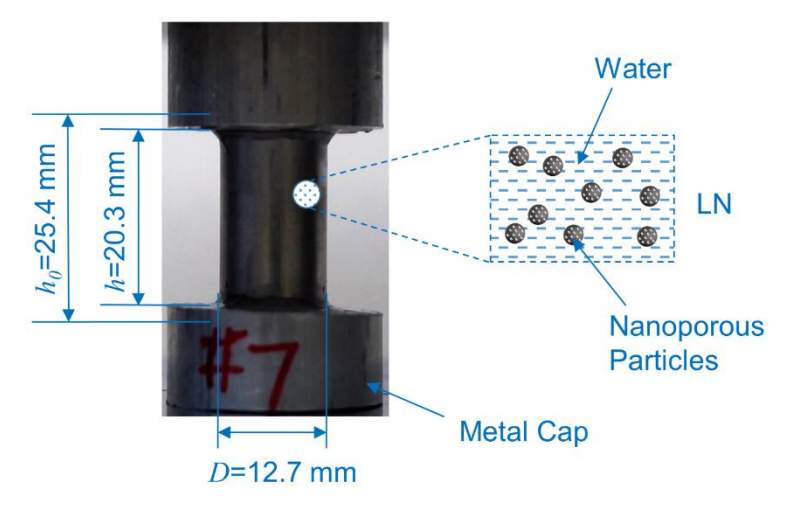


Figure 5-1: A typical LNFT sample with outer diameter of 12.7 mm and effective height of 20.3 mm.

5.2.2. Test Procedures

The mechanical behavior of empty, water-filled, and LN-filled steel tubes were characterized by a series of quasi-static compression and drop weight impact tests. At least three specimens were tested for each type of tubes. The quasi-static compression tests were conducted by a universal tester (Floor Model 5982, Instron, Inc.) at a constant speed of 2 mm/min. The nominal stress is calculated as

$$\sigma = \frac{F}{A_3}$$
 5 – 1

where F is the external force applied by the Instron machine and A_3 is the cross-sectional area of steel tubes. The nominal strain is calculated as

$$\varepsilon = \frac{\delta}{h}$$
 5 – 2

where, δ is the crosshead displacement.

The dynamic behavior of the steel tubes was characterized by a lab-customized drop tower apparatus (Figure 2-10). The impact speed of all dynamic tests, v, was maintained at 3.0 m/s by fixing the free drop height at 0.45 m. An accelerometer (353B03, PCB Group, Inc.) was attached to the 10 kg drop weight to measure the deceleration time-history which was recorded by a high-speed digitizer (PXIe-5105, NI Corp.) at the sampling rate of 10^6 samples/s. The nominal stress is calculated as

$$\sigma = \frac{m_w \cdot a \ \tau}{A_3}$$
 5 – 3

where, m_w is the drop weight and $a(\tau)$ is the measured deceleration of the drop weight at time τ . The displacement is calculated as

$$\delta = \iint a \, \tau \, d^2 \tau \tag{5-4}$$

The incident speed is confirmed by calculating

$$v = \int a \, \tau \, d\tau \tag{5-5}$$

5.3 Results

5.3.1. Liquid Infiltration Behavior of LN

The solid curve in Figure 5-2 shows a typical quasi-static mechanical behavior of the LN. As the LN was compressed at low pressure, the initial system volume change was slow. When the applied external pressure was in the range of 15 MPa and 30 MPa, a sudden volume change was observed, which indicated that liquid molecules were compressed into nanopores as the capillary effect of the hydrophobic nanopore surface was overcome. The total 0.55 cm³/g specific volume change,

which was consistent with gas adsorption analytical results [127], was defined as the effective pore volume of SG90. Upon unloading, the pressure dropped abruptly, leading to a highly hysteretic behavior of the LN system. As shown in Figure 5-2 (the dynamic curve), the liquid infiltration behavior of the LN, i.e. the liquid infiltration pressure as well as the effective pore volume, was strain rate insensitive under current dynamic impact condition.

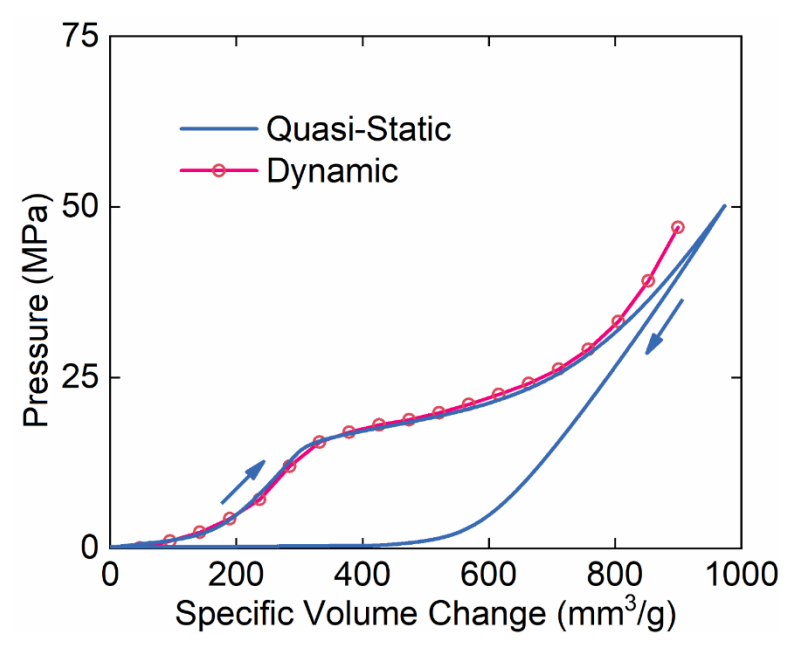


Figure 5-2: Typical sorption isothermal curves of LN under quasi-static compression test and dynamic impact test.

5.3.2. Quasi-Static Buckling Behavior of LNFT

Typical stress-strain curves and snapshots of the tube buckling modes are shown in Figure 5-3. The empty tube showed a sharp linear increase of stress at the beginning, after which the buckling was initiated at about 13 MPa (Figure 5-3a). As the buckling continued, the stress dropped abruptly, and a broad post-buckling stress plateau was formed. Figure 5-3b shows the buckling mode of the empty tube. The empty tube deformed with a diamond mode [186], in which non-axisymmetric folds formed sequentially from the top to the bottom of the tube.

For the water-filled tube, as the tube wall was supported by the liquid filler, it yielded and buckled outwards in a concertina mode [186] as shown in Figure 5-3c. Due to the negligible compressibility of water, the inner pressure built up immediately. Therefore, the water-filled tube was more rigid than empty one and failed at much smaller strain of 0.15. After the crack initiation, the tube continuously deformed as the filled water was squeezed out of the tube. The crack propagated with the progressive deformation of the tube, which weakened the post-buckling strength of the steel tube.

For the LNFT, the initial buckling behavior was similar to that of empty tube due to the tiny air bubbles trapped in between the SG90 particles and DI water. In this process, the tube wall was not reinforced by the LN filler and buckled in a non-axisymmetric diamond mode, as shown in the first snapshot of Figure 5-3d. At 0.1 nominal strain, the reinforcement effect of the LN filler started to take effect as water-filled tube. Once the nominal internal stress reached 10 MPa, the liquid infiltration process of the sealed LN was activated. Consequently, the LNFT became highly compressible and a broad reinforced post-buckling stress plateau was observed. The width of the stress plateau (w) was dependent on the mass ratio (R_m) of SG90 to water. When R_m was 0.3, wwas 50% of the initial height of the LNFT. By increasing R_m to 0.55, w was increased to 60% of the initial tube height. The width of plateau was not proportional to the amount of SG90, as the water amount was insufficient to fill all the nanopores in the LN with ${\cal R}_m=0.55.$ Since the tube wall was supported by the internal hydrostatic pressure, it buckled outwards in a concertina mode, as shown in Figure 5-3d. Upon completion of the liquid infiltration process, the LN became incompressible and the LNFT behave like the water-filled tube till burst. The average postbuckling strength, σ_0 , is calculated as

$$\sigma_0 = \frac{\int \sigma d\delta}{\delta}$$
 5 - 6

where σ and δ are post-buckling strength and displacement, respectively.

The results of the quasi-static behavior of the tubes were summarized in Table 5-1. The LN filler ($R_m=0.3$) increased σ_0 by 3 times from 4.9 MPa to 15.5 MPa. As the R_m increased to 0.55, σ_0 further increased to 17.8 MPa. Compared with water filled-tube, the failure strain of LNFT increased from 0.15 to 0.61 and 0.68 for 0.3 R_m and 0.55 R_m , respectively. The considerably enhanced σ_0 and failure strain were attributed to the hydrostatic pressure built in the LN and the high compressibility of the LN. As a result, the specific energy absorption capacity of LNFT, i.e. the total amount of absorbed energy normalized by the total mass of corresponding tube, was 40% higher than that of empty tube. In solid foam-filled tubes, the increase in specific energy absorption capacity was less than 20% [24,179,187–189].

Table 5-1: Comparison of empty, water-filled, and LN-filled tubes under quasi-static compression tests.

| ε= | = 0 ~ 0 . 7 | Mass (g) | Average Post-Buckling Strength, σ_0 (MPa) | Failure Strain |
|-------|----------------------------------|----------|--|-----------------|
| Em | pty Tube | 1.27 | 4.9±0.2 | N/A |
| Water | -Filled Tube | 3.76 | 5.1±0.4 | 0.15 ± 0.05 |
| LNFT | $R_{m} = 0.3$ | 3.45 | 15.5±0.3 | 0.61±0.02 |
| | $R_m = 0.55$ | 3.36 | 17.8±0.3 | 0.68 ± 0.03 |

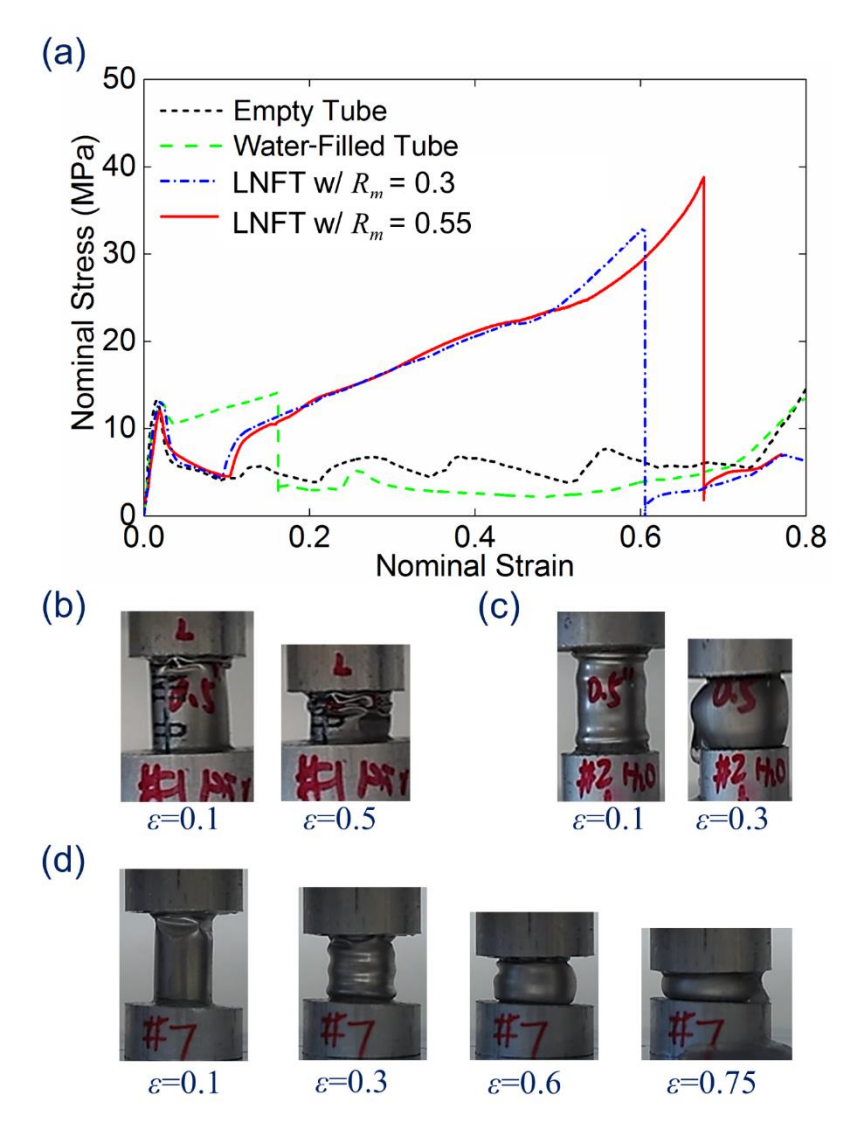


Figure 5-3: (a) Typical stress-strain curves of filled steel tubes (b-d) Snapshots of the buckling behavior of (b) Empty tube (c) Water-filled tube (d) LNFT.

5.3.3. Dynamic Buckling Behavior of LNFT

Figure 5-4 shows typical dynamic stress-strain curves of empty, water-filled, and LN-filled steel tubes. The dynamic stress-strain curve for the empty tube had the same number of stress peaks as the quasi-static one, indicating the empty tube had identical number of tube wall buckling folds at different strain rates. The average post-buckling stress of the plateau in dynamic impact increased by 4% compared to that of the quasi-static loading, probably due to the rate dependency behavior of the stainless steel [190].

The dynamic behavior of water-filled tube was observed to be rate sensitive too. The failure crack occurred at the nominal strain of 0.15 as indicated by the sudden stress drop in the constitutive behavior of the tube (Figure 5-4b). However, different from the quasi-static case, at higher strain rate, the post-buckling strength of the water-filled tube did not decrease due to the crack. This was mainly attributed to the quick self-sealing response of the tube, which was caused by the faster tube wall folding under dynamic impacts. Therefore, the average post-buckling strength of water-filled tube was higher under dynamic impact than quasi-static loading.

Figure 5-4c and Figure 5-4d represent typical dynamic stress-strain curves of LNFTs. For the $R_m=0.3$ (Figure 5-4c), the LN was activated at about 0.15 strain, after which the stress increased quickly. In comparison to the quasi-static compressive behavior, the post-buckling strength of the LNFT was higher under dynamic impact, which was not expected since both the liquid infiltration behavior and the empty tube wall buckling were nearly strain rate independent. Similar phenomenon was observed in the LNFT with $R_m=0.55$ (Figure 5-4d). The failure strain of LNFT was slightly reduced by about 0.05 compared to the quasi-static value.

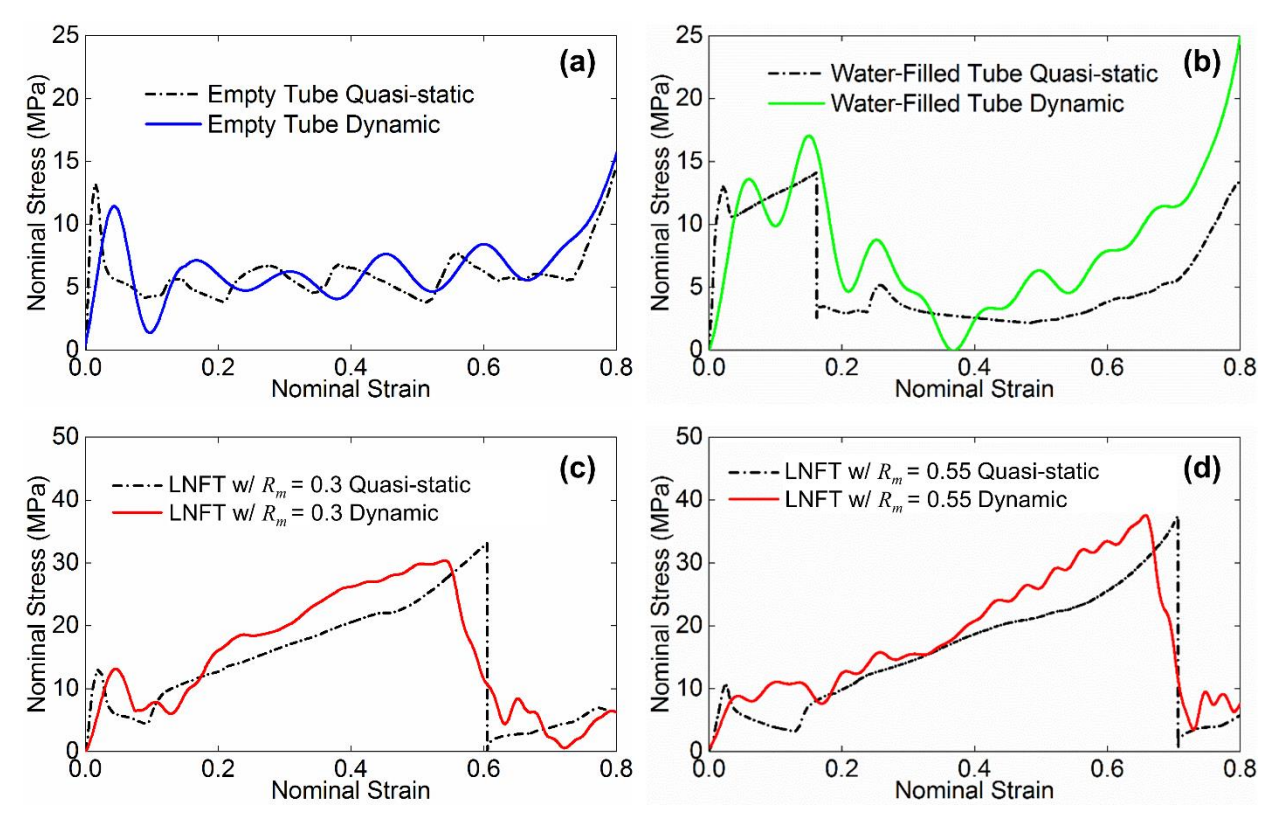


Figure 5-4: Typical stress-strain curves of tubes under dynamic tests (a) Empty tube (b) Water-filled tube (c) LNFT with R_m =0.3 (d) LNFT with R_m =0.55.

Table 5-2: Comparison of empty, water-filled, and LN-filled tubes under dynamic tests.

| $arepsilon=0	ext{\sim}0.7$ | | Mass (g) | Average Post-Buckling Strength, σ_0 (MPa) | Failure Strain | |
|----------------------------|-------------|----------|--|----------------|--|
| Empty Tube | | 1.27 | 5.1±0.3 | N/A | |
| Water-Filled Tube | | 3.76 | 5.7±0.4 | 0.15 ± 0.06 | |
| LNFT | $R_m = 0.3$ | 3.45 | 17.5±0.3 | 0.55±0.03 | |
| | $R_m=0.55$ | 3.36 | 20.1±0.3 | 0.64 ± 0.03 | |

The results of the dynamic tests of steel tubes were summarized in Table 2. The σ_0 of empty tube was 5.1 MPa, while the σ_0 of LNFT with $R_m=0.3$ was 17.5 MPa, which was increased by 240%. σ_0 increased to 20.1 MPa when the R_m increased to 0.55.

5.4 Discussion

5.4.1. LN-Tube Wall Interaction

In the LNFT, the LN increases σ_0 without affecting the deformability of the tube due to the unique liquid infiltration behavior of the LN. By analyzing the combination of the post-buckling strength and the deformability of the LNFT, i.e. the energy absorption capacity, strong liquid-solid interaction exists at the LN and the tube wall interface. As shown in Figure 5-5, under quasi-static compression condition, the combined energy absorption capacity of the LN and the empty tube contributes only 52% to the energy absorption capacity of the LNFT. The 48% difference in the energy absorption capacity is attributed to the LN-tube wall interaction. Under dynamic conditions, the difference is further increased to 55%. Please note that the liquid infiltration behavior of the LN is strain-rate independent (Figure 5-2) and the buckling behavior of the empty tube is nearly insensitive to the strain rate (Figure 5-4a). Therefore, the increase in the dynamic energy absorption capacity of the LNFT demonstrates that the LN-tube wall interaction is strain rate sensitive.

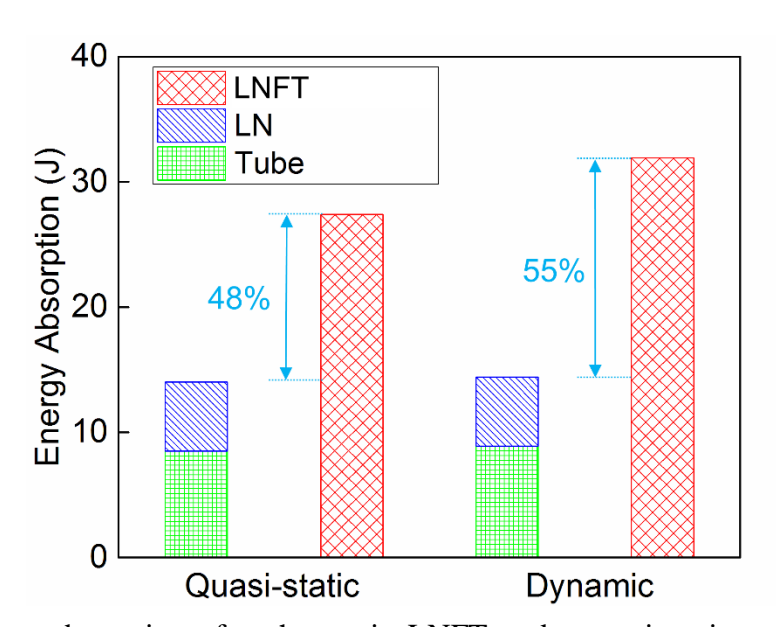


Figure 5-5: Energy absorption of each part in LNFT under quasi-static compression tests and dynamic tests.

The LN-tube wall interaction can be attributed to two main effects: (1) Suppression of inward buckling and (2) Densification effect in folds. Figure 5-3b and Figure 5-3d explain the effect of the suppression of inward buckling. The empty tube wall buckles inwards in a diamond mode. The localized deformation is due to the large stress concentration coefficient generated by the inward folding. In the LNFT, the LN filler completely suppresses the progressive inward buckling and promotes multiple outwards buckling simultaneously (Figure 5-3a and Figure 5-3d). The resulted plastic expansion of the tube wall, i.e. the strain hardening effect, accounts for the increase in the energy absorption capacity of the LNFT, which has been validated by Liu et al. [191,192] in foamfilled tubes.

For the densification effect in folds, it has been reported that the densification of solid foam in folds can increase the load transfer between the tube wall and the filler [179]. However, the deformation of solid foams is based on the cell-wall buckling which is neither smooth nor stable. In addition, delamination in solid foam-filled tubes cannot be avoided when the compressive strain is large. In LNFTs, the load drop caused by folding collapse is prevented because the load transfer effect in the LN is significantly improved and stabilized by the uniform hydrostatic pressure built-up in the LN filler in compliance with the progressive buckling. This is because of the smooth liquid infiltration plateau of the LN (Figure 5-2) and the increased interfacial area between filler and tube wall due to the fluidity of the LN.

The increased liquid-solid interaction in LNFT at high strain rate is attributed to the following possible effects: Firstly, the bulk modulus of water in the LN becomes higher under high speed impact [193,194], thus, the reinforcement effect on the tube wall increases. Secondly, the strain rate effect of tube wall is amplified by both the reinforcement effect of the LN filler and the

changed buckling mode. Thirdly, higher order buckling mode [185,195] is triggered by the internal hydrostatic pressure associated with the LN.

5.4.2. Effect of Liquid-Solid Interfacial Bonding

To further investigate the effect of interfacial bonding on the filler-tube wall interaction, solid foam-filled tubes were prepared for comparison. The solid polyethylene (PE) foam (Ethafoam 900, Sealed Air) was cut to shape and directly inserted into the empty tube without any further treatment. The PE foam-filled tube was characterized both quasi-statically and dynamically.

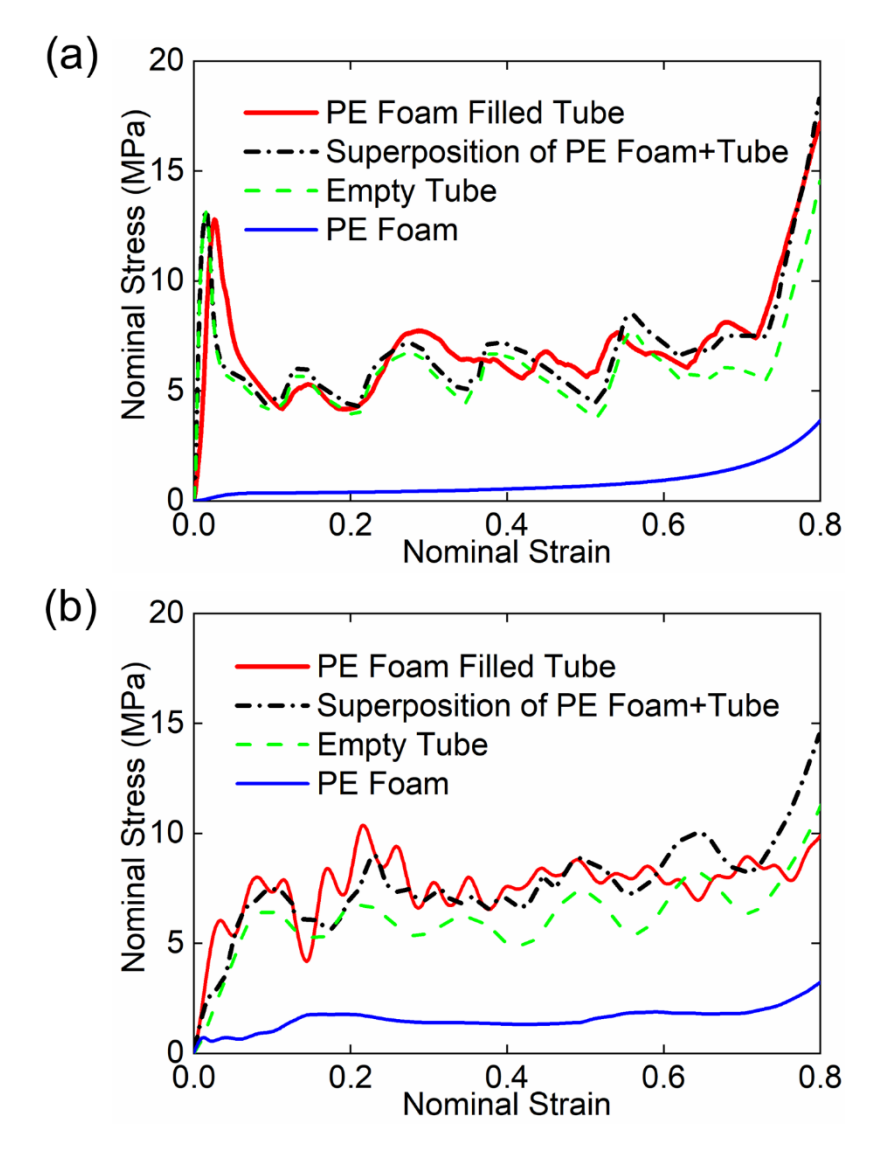


Figure 5-6: Typical stress-strain curves of PE foam-filled tubes (a) under quasi-static compression tests (b) under dynamic tests.

In comparison, it was observed that the quasi-static buckling performance of the PE foam-filled tube was equivalent to the superposition of the individual crushing behaviors of the PE foam and the empty tube (Figure 5-6a). This observation was further verified through energy absorptions capacity. The energy absorption capacities of the PE foam and the empty tube were 0.73 J and 8.5 J, respectively. The energy absorption capacity of the PE foam-filled tube was 9.2 J, which equaled to the summation of energy absorption capacities of the PE foam and the empty tube. Similarly, the superposition rule was valid for the PE foam-filled tube under dynamic impacts (Figure 5-6b). Therefore, in such a solid foam-filled tube there was negligible filler-tube wall interaction.

To evaluate the effect of interfacial bonding on the filler-tube wall interaction, the filler-tube wall interaction is quantified. Based on the numerical simulation conducted by Santosa et al. [178], the following equation is applied to evaluate the average post-buckling strength of foam-filled tubes,

$$\sigma_{0ft} = \sigma_{0e} + C\sigma_{0f} \tag{5-7}$$

where, σ_{0ft} , σ_{0e} and σ_{0f} represent the average post-buckling strength for foam-filled tube, empty tube and filler, respectively. The constant C is the strengthening coefficient, which indicates the strength of filler-tube wall interaction. To compare our results with previous studies in this area, we summarize the strengthening coefficients of several foam-filled tubes in Figure 5-7. In the current study, the PE foam-filled tube and the LNFT have C values of 0 and 3.8±0.3, respectively.

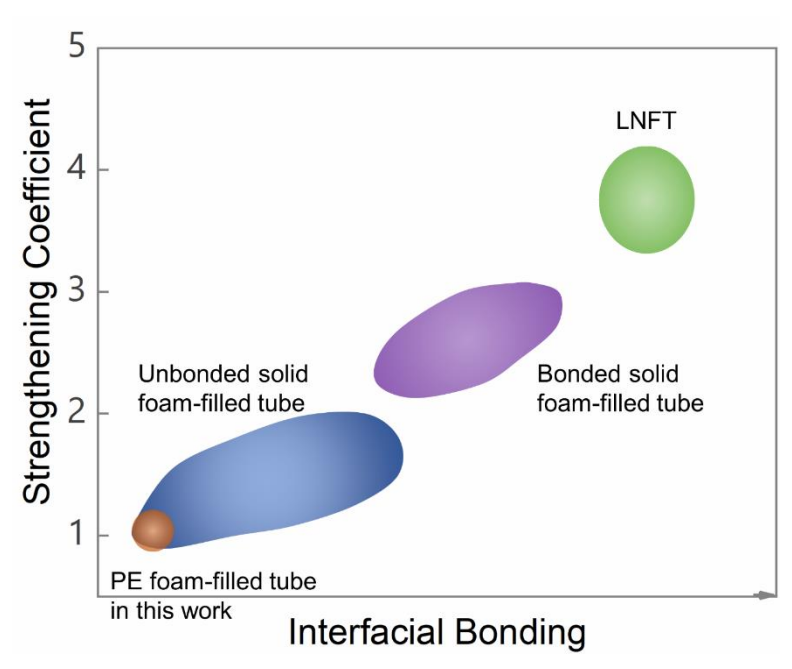


Figure 5-7: Comparison of *C* in foam-filled tubes, including LNFT in this work, bonded solid foam-filled tube [25,26,28,177–179], unbonded solid foam-filled tube [24,27,29,30,175,176,178,179] and PE foam-filled tube in this work.

Previous studies [25,26,28,179] have demonstrated that the filler-tube wall interaction increases when the strength of the interfacial bonding increases, which is also reflected by the linear relationship between the strengthening coefficient and the interfacial bonding strength (Figure 5-7). For the tube filled with PE foam, there is no interfacial bonding and the PE foam has a relatively low strength compared with the thin-walled steel tube. The deformation behavior of the PE foam-filled tube is dominated by the inward buckling mode (Figure 5-8a). Therefore, the strengthening coefficient and the filler-tube wall interaction are nearly zero. When the tube is filled with solid foam with higher strength, such as metallic foam, the deformation pattern of foam-filled tube changes to axisymmetric modes (Figure 5-8b). Even without interfacial bonding, typical strengthening coefficient of the foam-filled tube becomes 1.8 as additional energy dissipation mechanisms are involved in the buckling process, including the suppression of inward buckling and the interfacial friction between filler and the tube wall [16,30,196]. If the interfacial bonding is improved by adhesive, more energy dissipation mechanisms are involved, such as load transfer

from the tube wall to the filler and the breakage of the interfacial bonding (Figure 5-8b). Thus, typical strengthening coefficient further increases to 2.8, revealing the enhanced filler-tube wall interaction. By replacing the solid foam filler to the LN, the strengthening coefficient increases to 3.8, indicating that the liquid-solid interaction is much stronger than the best solid foam-tube wall interaction. This nearly "perfect bonding" is attributed to the fluidity and the liquid infiltration behavior of the LN. The LN accommodates the deformed tube wall shape and is always "bonded" to the tube wall, as the deformation of the tube wall progresses (Figure 5-8c).

The difference between strengthening coefficients of bonded foam-filled tube and LNFT is the solid-solid bonding imperfection. In metallic foam-filled tube, the solid foam filler detaches from the tube wall when the local stress reaches a critical value, due to the stiffness mismatch between the filler and the tube wall as well as the stress concentration effect generated by the interfacial imperfections [25,26,28]. The detached tube (Figure 5-8b) simply ensembles the behavior of unbonded foam-filled tube, resulting in a reduced performance [178]. In contrast, the outward buckling folds of LNFT are always filled with the LN, which eliminates delamination. Therefore, the LN reinforces the tube wall during the buckling process.

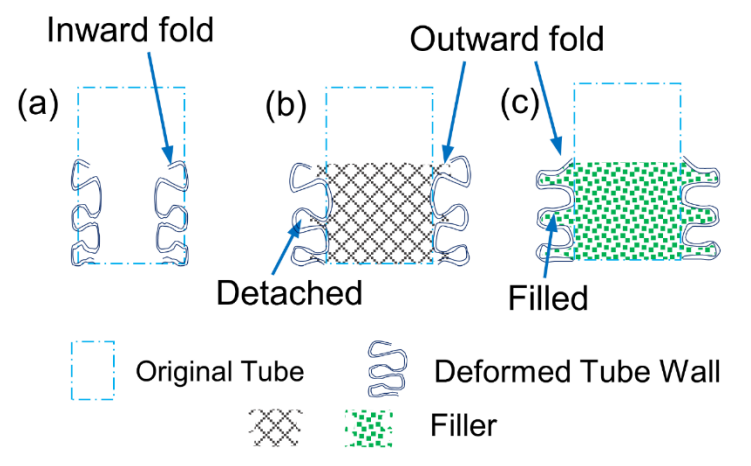


Figure 5-8: Schematic of the filler-tube wall interaction of (a) Empty tube (b) Solid foam-filled tube with imperfect interfacial bonding (c) LNFT or solid foam-filled tube with perfect interfacial bonding.

The improvement of the strengthening coefficient in LNFT indicates that promoting the fillertube wall interaction is an effective method to improve the crashworthiness of thin-walled
structures, since the tube wall buckling mechanism dominates the energy absorption performance
of the composite structure over others, such as friction, debonding, etc. This is consistent with the
findings of Ref. [197], in which more local plastic deformation were triggered, leading to increase
in energy absorption. In LNFT, damage localization can be overcome due to the enhanced load
transfer between the LN filler and the tube wall, which triggers multiple outwards tube wall
buckling at the same time and dramatically increases the strengthening coefficient and the energy
absorption capacity of the LNFT.

5.5 Conclusion

In this chapter, we have experimentally investigated the post-buckling behavior of the LNFT at different strain rates. Based on the direct comparison of strengthening coefficient and energy absorption capacities of tubes with different types of fillers, the following conclusions can be drawn:

- (1) The LN filler significantly promotes the average post-buckling strength of the tube under both quasi-static and dynamic conditions;
- (2) In LNFT, the LN suppresses the inward buckling mode of empty tube and exhibits better load transfer between filler and tube wall than solid foam fillers;
- (3) The strengthening coefficient of LNFT is 3.8, which is much higher than that of best solid foam-filled tube;
- (4) The LN-tube wall interaction is much stronger than solid foam-tube wall interaction. In addition, the liquid-solid bonding is nearly perfect at the LN-tube wall interface.

In short, the LN is a promising filling material for thin-walled tubes to enhance the post-buckling performance as well as the energy absorption capacity of the LNFT. The findings of this study have merit in potential future applications in next generation light-weight and small-scale cellular structures for vehicle crashworthiness.

Chapter 6

LN-Functionalized Thin-Walled Structure – Large-Scale

Chapter 5 presents the reinforcement effect of liquid nanofoam (LN) on small-scale thin-walled tubes under impact with relatively low incident energy. In practical applications in automobile industry, the impact energy is much higher, and thus large-scale structures are desired. This chapter presents an experiment investigation on the dynamic behavior of large-scale thin-wall tubes reinforced by LN. Results show by increasing the incident speed from quasi-static condition (10⁻³ m/s) to dynamic range (6.7 m/s), the energy absorption capacity of LNFTs is increased by 54% without increasing the working pressure of the system. The rate sensitive behavior of LNFTs suggests that LNFTs can be used as advanced energy absorber whose impact mitigation capability is adaptive to the impact energy levels. These findings pave the way for applications of these new liquid nanofoam filled thin-walled structures for vehicle crashworthiness and infrastructure protection.

6.1 Introduction

Over last decades, enormous efforts have been made to develop Advanced Energy Absorption Materials and Structures (AEAMS) [198]. AEAMS can mitigate the kinetic and strain energies associated with the impact when subjected to external loadings, and thus mitigate personnel injuries or key facilities damages. Among many other AEAMS, thin-walled structures, e.g. thin-walled metallic tubes, have been widely used as conventional energy absorbing devices due to their light weight and high energy absorption capacity [14,15]. The axial folding of the tube wall is known as the main working mechanism. However, the tube wall buckling initiation requires a

relatively large stress, after which the average stress of post-buckling plateau drops abruptly. The specific energy absorption of empty tube is dominated by the post-buckling stress. Therefore, the specific energy absorption is much lower than the theoretical limit which is proportional to the initial buckling stress. In past years, extensive research has been focused on metallic foam-filled thin-walled tubes and it has been demonstrated that filler-tube interaction can effectively improve the energy absorption and mechanical properties of the resulted hybrid tube under both quasi-static [24,27,28] and dynamic [29,30] conditions. However, due to the mechanical properties mismatch between the metallic foam filler and the tube wall, delamination between filler and tube wall is inevitable at large deformation [26]. Therefore, the interaction effect between filler and tube wall is weakened, leading to a reduced energy absorption capacity.

Recently, a highly compressible liquid system, liquid nanofoam (LN) [57,121,156,199], has been employed as an advanced filler to improve the energy absorption performance of thin-walled tubes [165,185,200]. LN composes of hydrophobic nanoporous materials and a non-wettable liquid. Due to capillary effect, the liquid stays outside the nanopores at ambient condition. As an external load is applied, the liquid is forced into the nanopores and tremendous amount of energy is dissipated [56]. Since LN is in liquid form, it can always fit well with the buckled tube wall at all strain levels; that is, a "perfect bonding" can be created between LN and tube wall, leading to an improved interaction effect. Previous studies on liquid nanofoam filled tubes (LNFTs) have demonstrated that the specific energy absorption of empty tube under both quasi-static compression and dynamic impact can be improved by the LN filler [183,184] and the dominant reinforcing mechanism, e.g. filler-tube wall interaction, has been extensively studied in [165]. However, those studies are limited to small-scale demonstration and the incident energy is relatively low. This chapter focuses on the mechanical response of large-scale LNFTs subjected

to external impact with relatively high incident energy. Results show that the energy absorption performance of the larges-scale LNFTs is considerably enhanced, especially under dynamic conditions.

6.2 Materials and Methods

6.2.1. Materials and Sample Preparation

Thin-walled aluminum (Al 6061) tube was purchased from McMaster (Product No. 9056k85). The outer diameter, wall thickness and height of the Al tube were $R=38.1\ mm$, $t=1.63\ mm$ and $h_0=101.6\ mm$, respectively. The thin-walled Al tube was filled with LN and then sealed by attaching both ends with two metal caps equipped with O-rings. The effective height of the tube was $h=81.3\ mm$. Empty Al tube was used as reference. During all experimental processes, no liquid leakage was observed at the sealing part of the Al tubes. Figure 6-1 shows a typical LNFT sample.

The LN used in this study contained a nanoporous silica (60759, Sigma-Aldrich) and 15 wt% ethanol aqueous solution. The particle size and average nanopore size of the nanoporous silica were $40-63~\mu m$ and 7.8~nm [127], respectively. The as-received nanoporous silica had C8 modified surface, which was non-wettable to the aqueous solution. The nanoporous structure can be found in Figure 2-5.

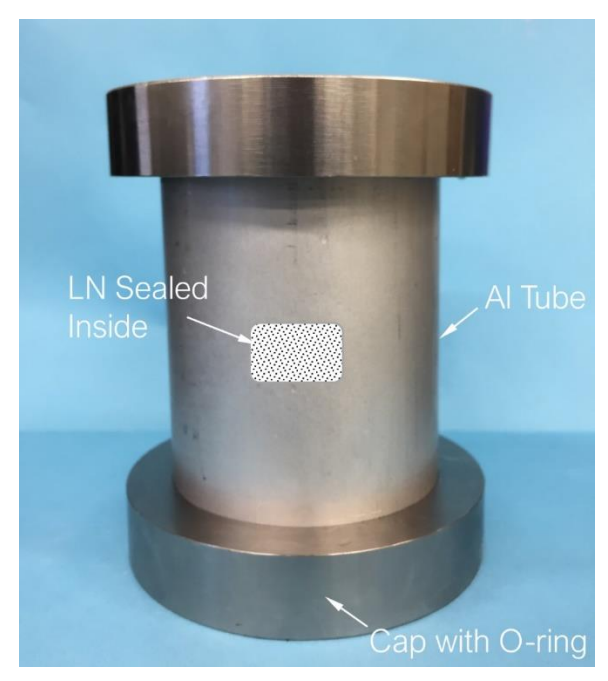


Figure 6-1: A typical large-scale LNFT sample with outer diameter of 76.2 mm and effective height of 81.3 mm. The LNFT was sealed by two metallic caps equipped with O-rings.

6.2.2. Test Procedures

The quasi-static infiltration behavior of the LN was characterized by quasi-static pressure-induced infiltration tests by an Instron 5982 universal tester at a constant loading rate of 2 mm/min. The LN specimen was sealed in a stainless-steel testing cell. The applied force was gradually increased from 0 kN to 6.3 kN, after which the Instron crosshead was moved back at the same speed.

The mechanical behavior of empty and LN filled Al tubes were characterized by a series of quasi-static compression and gas gun impact tests. The quasi-static compression tests were conducted by using an MTS system at a constant loading rate of 2 mm/s. The experimental setup of quasi-static compression test can be found in Figure 2-4.

The dynamic behavior of the Al tubes was characterized by a gas gun apparatus at Ford Motor Company. The incident speed and carriage weight of gas gun tests were 6.7 m/s and 181.55 kg, respectively. A load sensor was attached on the bottom of the sample to measure its load time-

history F-t. An accelerometer was attached to the carriage to measure the deceleration time-history a-t. The displacement is calculated as

$$\delta = \iint a \, \tau \, d^2 \tau \tag{6-1}$$

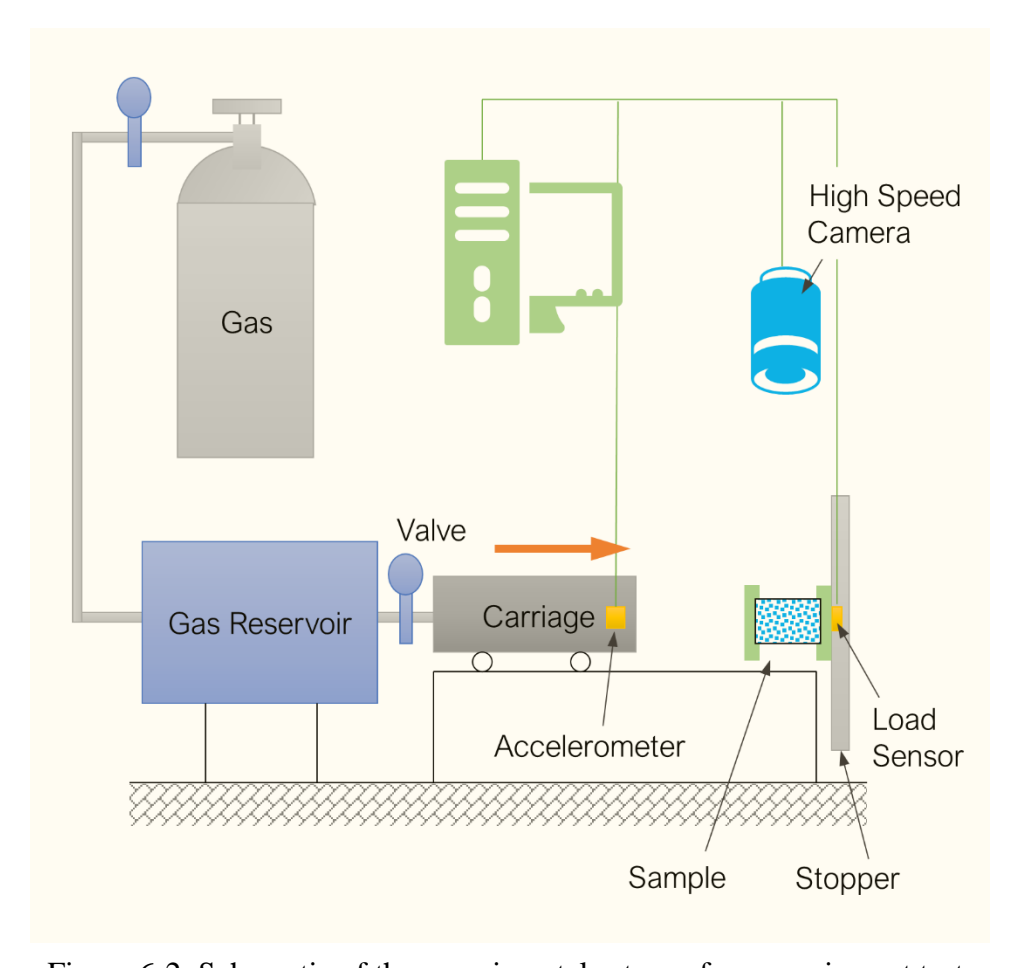


Figure 6-2: Schematic of the experimental set-up of gas gun impact test.

The nominal stress is calculated as

$$\sigma = \frac{F}{A_4} \tag{6-2}$$

where ${\cal A}_4$ is the cross-sectional area of Al tubes. The nominal strain is calculated as

$$\varepsilon = \frac{\delta}{h} \tag{6-3}$$

The buckling mode of the Al tubes under gas gun impact was recorded by high speed cameras.

6.3 Results

6.3.1. Liquid Infiltration Behavior of LN

Figure 6-3 shows typical quasi-static pressure induced infiltration behavior of the LN. Initially, the LN system volume decreased slowly when the applied external pressure was relatively low since liquid infiltration was not triggered due to the capillary resistance. When the pressure increased to about 5 MPa, the slope of the curve decreased remarkably and a stress plateau was observed. The plateau indicated that the capillary effect of the hydrophobic nanopore was overcome and the liquid molecules were driven into the nanopores. As the external pressure reached around 12 MPa, all nanopores were filled with liquid and the infiltration plateau ended. Therefore, the working pressure of LN ranged from 5 MPa to 12 MPa. The effective pore volume, which was the volume change during liquid infiltration, was around 450 mm³/g. Upon unloading, the pressure dropped abruptly, leading to a highly hysteretic behavior of the LN system.

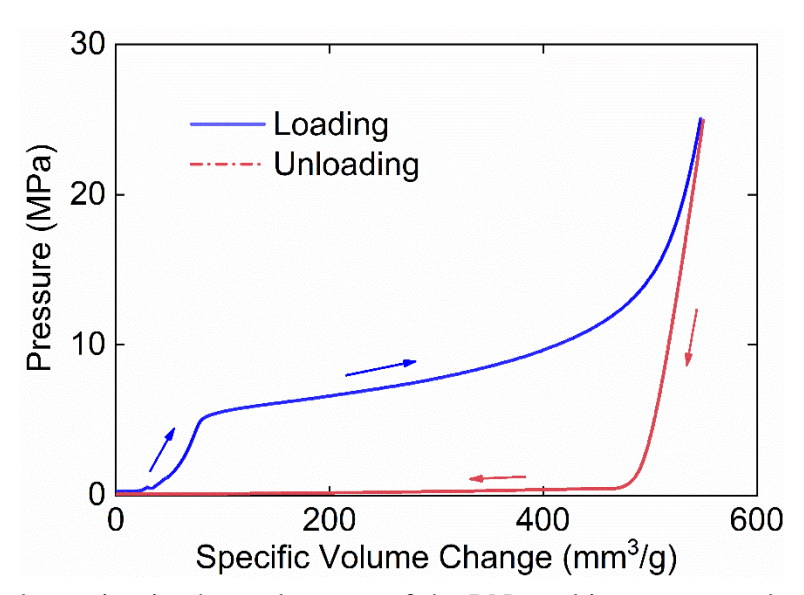


Figure 6-3: Typical sorption isothermal curves of the LN used in current study under quasi-static compression test.

6.3.2. Quasi-Static Behavior of LNFT

Typical stress-strain curves and snapshots of the tube buckling modes are shown in Figure 6-4. The empty tube wall buckling was initiated at 25 MPa, after which the stress level dropped to around 10 MPa and a wide stress plateau was formed (Figure 6-4a). Figure 6-4b shows the buckling mode of the empty tube. The empty tube deformed with a diamond mode, which was consistent with the literature [30,187,196]. Non-axisymmetric folds with 3 corners per lobe formed sequentially along the tube length.

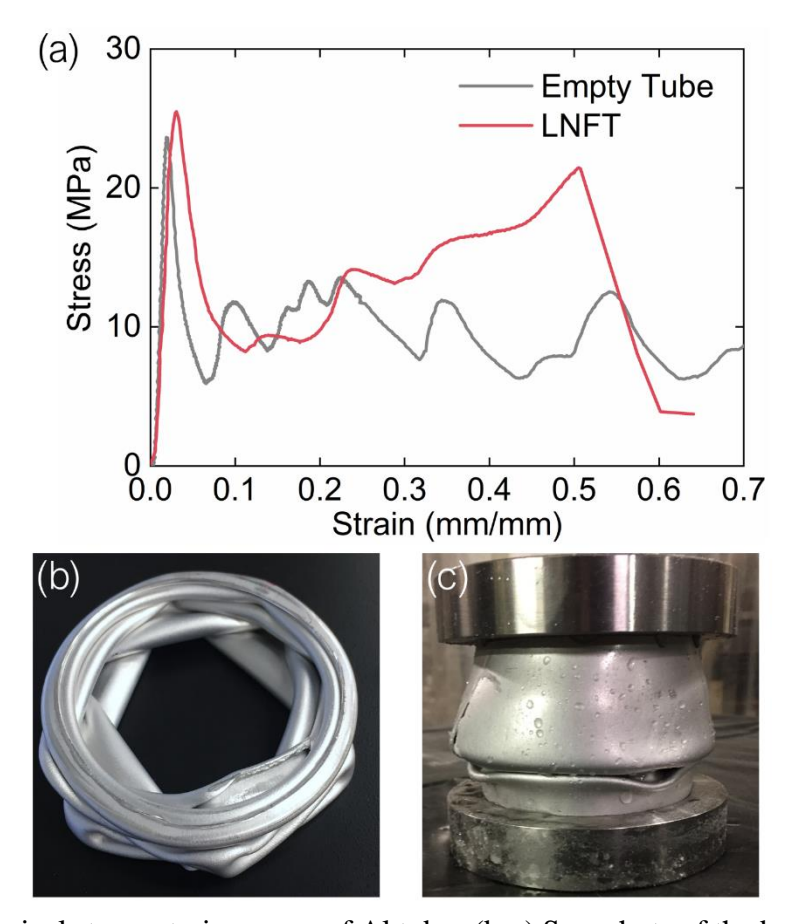


Figure 6-4: (a) Typical stress-strain curves of Al tubes (b-c) Snapshots of the buckling behavior of (b) Empty tube (c) LNFT.

As the tube was filled by LN, the buckling initiation was not affected. The stress drop after buckling initiation resulted from the small amount of air bubbles trapped in the LN. At strain of 0.2, the LN filler started to take effect and the nominal stress increased to about 13 MPa. The system then became highly compressible and an enhanced post-buckling stress plateau was observed. The width of the stress plateau was around 30% of the effective height of the LN tube. As the nominal stress increased to 20 MPa, the tube wall cracked, which led to leakage of the LN. From this point, the behavior of the LN-filled tube was similar to that of the empty tube as the solid-liquid interaction was nearly zero. Figure 6-4c shows the LNFT buckled in an axisymmetric concertina mode.

The results of the energy absorption of the tubes under quasi-static compression were summarized in Table 6-1. The energy absorption capacity was calculated by

$$E = \int F \ d\delta \tag{6-4}$$

The energy absorption capacity of empty tube at total strain of 0.5 was 1843 J, while the value of LNFT was 2678 J. Therefore, the energy absorption capacity was improved by 45%. The increase of energy absorption capacity of LNFT is due to the enhanced liquid-solid interaction between LN and tube wall as well as the high compressibility of LN.

Table 6-1: Comparison of empty and LN-filled tubes under quasi-static compression tests.

| $arepsilon=0{\sim}0.5$ | Strain at Burst | Average Post-Buckling Strength, σ_0 (MPa) | $\boldsymbol{E}\left(\mathbf{J}\right)$ | $m{E_{LN}}\left(\mathbf{J} ight)$ |
|------------------------|-----------------|--|---|-----------------------------------|
| Empty Tube | N/A | 10.2 | 1843 | N/A |
| LNFT | 0.5 | 14.7 | 2678 | 243 |

6.3.3. Dynamic Behavior of LNFT

Figure 6-5 shows typical dynamic stress-strain curves of empty Al tubes. The average post-buckling stress of empty tubes in gas gun impact test was 11.3 MPa, about 10% higher than that in quasi-static compression tests. This was due to the rate sensitivity of the Al material [201].

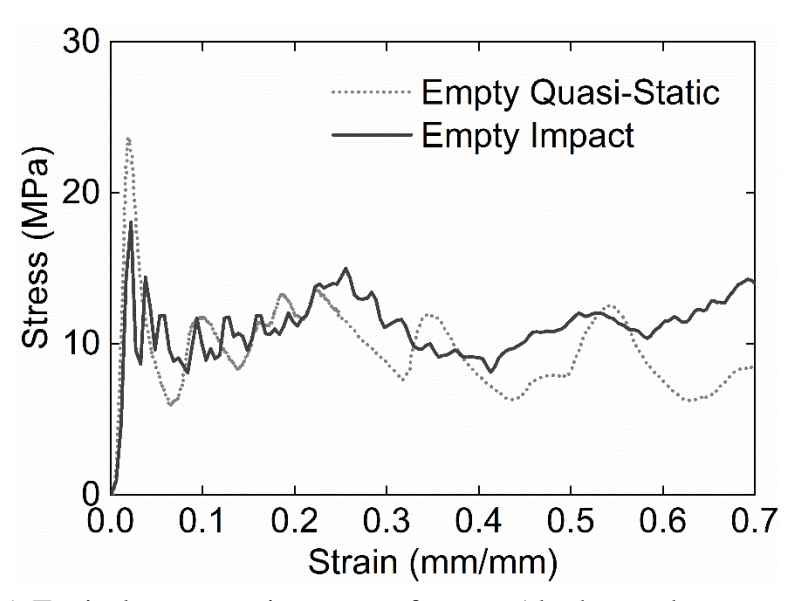


Figure 6-5: Typical stress-strain curves of empty Al tubes under gas gun impact.

Figure 6-6 shows the snapshots of empty Al tube under gas gun impact. The buckling mode was similar to that in quasi-static compression tests, in which the tube buckled inwards in a diamond mode.

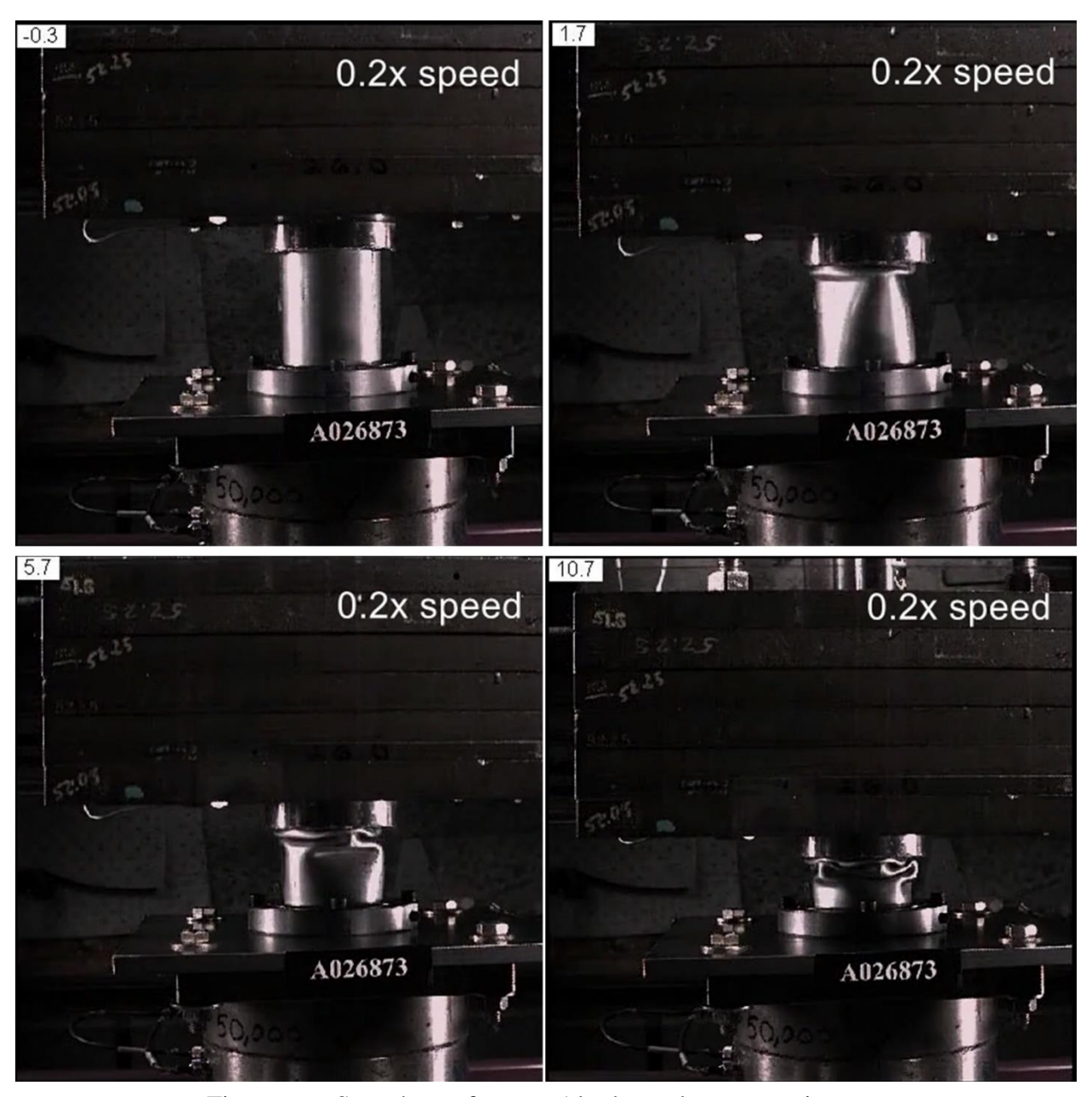


Figure 6-6: Snapshots of empty Al tube under gas gun impact.

Figure 6-7 shows typical dynamic stress-strain curves of LNFTs. Under gas gun impact, the LN took effect at about 0.15 strain, after which the stress level increased dramatically. The post-buckling strength of the LNFT under gas gun impact was 19.3 MPa, much higher than that in the quasi-static compression tests. The 36% increase was due to the rate sensitive behavior of LNFT. At 0.6 strain, all the incident energy was mitigated by the LNFT. Surprisingly, the LNFT was not

burst; that is, there remained energy absorption capacity in the LNFT. This was further demonstrated by evaluating the remain nanopore volume of the LN in LNFTs after tests. As shown in Figure 6-8, after quasi-static compression test, the LN had 25% of pore available, while after gas gun impact, the remaining pore volume was about 40%.

The results of the gas gun impact tests of Al tubes were summarized in Table 6-2. The energy absorption capacity of LNFT under gas gun impact was 4130 J, which was 54% higher than that in quasi-static compression tests.

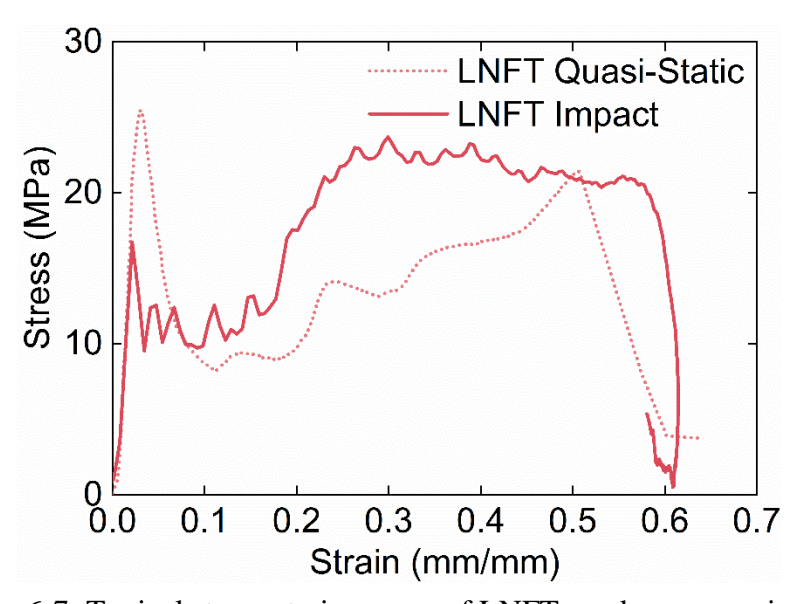


Figure 6-7: Typical stress-strain curves of LNFTs under gas gun impact.

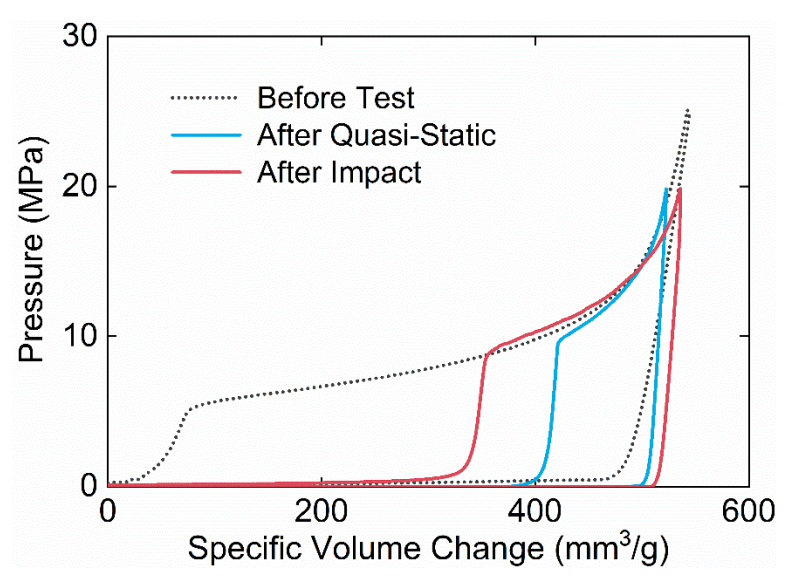


Figure 6-8: Typical sorption isothermal curves of the LN in LNFTs after quasi-static compression test and gas gun impact test.

Table 6-2: Comparison of empty and LN-filled tubes under gas gun impact.

| $arepsilon=0{\sim}0.6$ | Strain at Burst | Average Post-Buckling Strength, σ_0 (MPa) | $\boldsymbol{E}(J)$ | $m{E}_{LN}\left(\mathbf{J} ight)$ |
|------------------------|-----------------|--|---------------------|-----------------------------------|
| Empty Tube | N/A | 11.3 | 2349 | N/A |
| LNFT | N/A | 19.3 | 4130 | 205 |

Figure 6-9 shows the snapshots of LNFT under gas gun impact. The buckling mode was quite close to that in quasi-static compression tests. First, an outward fold was generated in a concertina mode. As the impact progressed, the second fold was formed. Further impact led to the expansion of the second fold and the cross-sectional area of the LNFT increased quickly. Clearly, the buckling behavior of LNFT was dominated by the second fold.

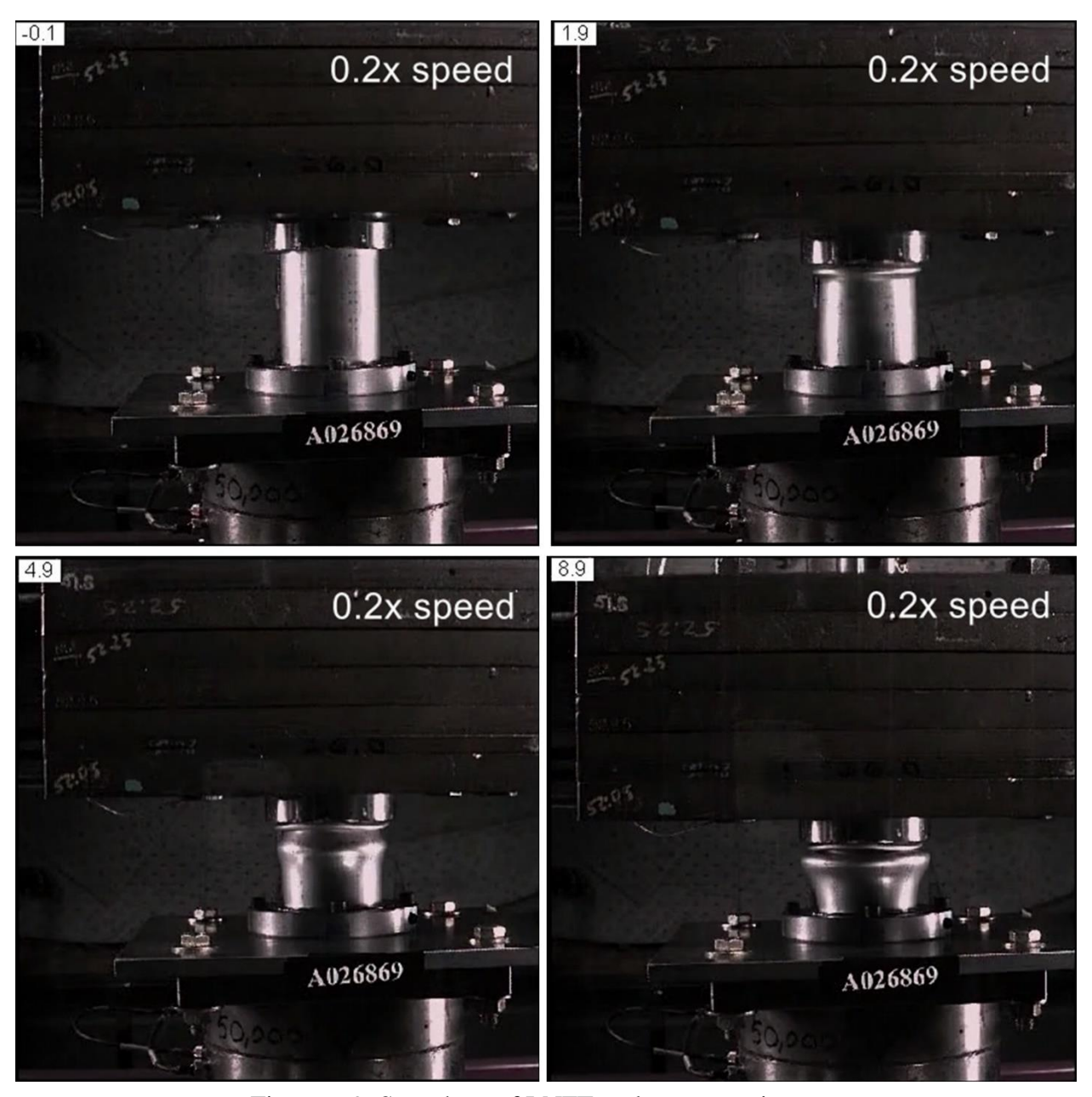


Figure 6-9: Snapshots of LNFT under gas gun impact.

6.4 Discussion

6.4.1. LN-Tube Wall Interaction

As demonstrated in the chapter 5, there exists strong liquid-solid interaction between LN and tube wall, which can significantly improve the energy absorption capacity of LNFT. According to

Santosa et al. [178], the LN-tube wall interaction can be quantified by the strengthening coefficient C,

$$\sigma_{0ft} = \sigma_{0e} + C\sigma_{0f} \tag{6-5}$$

where, σ_{0ft} , σ_{0e} and σ_{0f} are the average post-buckling strength for foam-filled tube, empty tube and filler, respectively. Since the tube and LN have same nominal volume, we have

$$E_{LNFT} = E_e + CE_{LN} \tag{6-6} \label{eq:energy}$$

where, E_{LNFT} , E_e and E_{LN} are the energy absorption capacity of LNFT, empty tube and LN, respectively.

Based on the energy absorption results in Table 6-1, the *C* of LNFT under quasi-static compression test is calculated as 3.5. The value is consistent with the results of small-scale LNFTs in the previous chapter. The large strengthening coefficient indicates higher filler-tube wall interaction, which is attributed to the nearly "perfect bonding" between LN and tube wall due to its fluidity and liquid infiltration behavior [165]. As the tube wall buckling progresses, the LN can always adapt to the deformed tube wall and maximize its interaction with the tube wall.

The LN contributes to improve the filler-tube wall interaction by two main mechanisms: (i) load transfer effect from the tube wall to the LN and (ii) suppression of inward buckling [165]. Figure 6-3 and Figure 6-4 explain the load transfer effect between LN and tube wall. The LN possesses smooth stress plateau and it considerably increases the contact area between LN and tube wall due to its fluidity. Consequently, the load transfer between LN and tube wall is significantly improved by the evenly distributed hydro-static pressure of LN, which prevents load drop due to the collapse of tube wall folds.

Figure 6-4c shows the suppression of inwards buckling by LN. This has increased the effective cross-sectional area to bear more load. More importantly, the extent of plastic deformation of the

tube wall is remarkably promoted, resulting in higher strain hardening of the metallic tube wall. That is, the outwards buckling triggers the potential energy absorption capacity of the tube wall material.

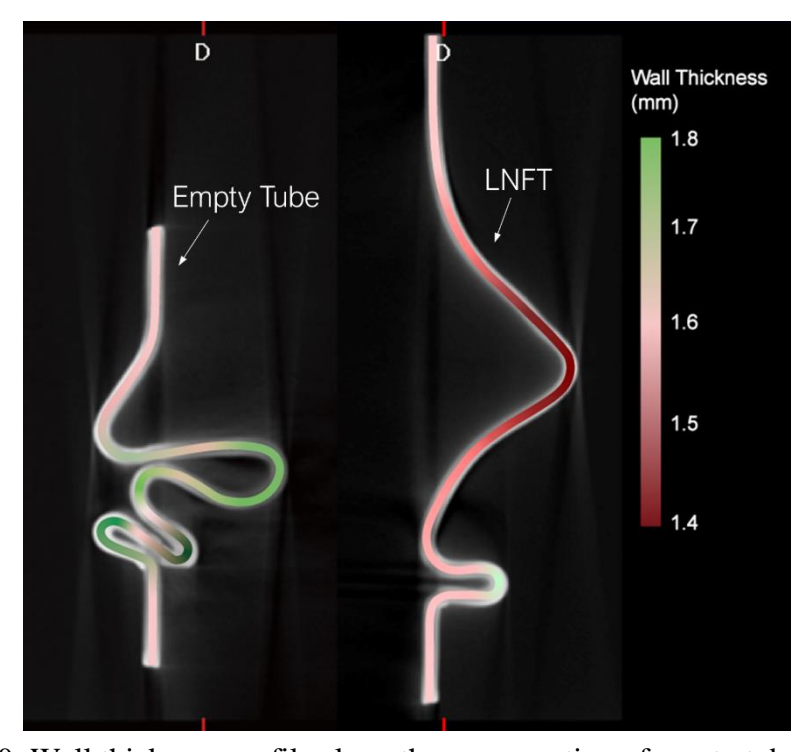


Figure 6-10: Wall thickness profile along the cross-section of empty tube and LNFT.

The improved plastic expansion of the tube wall has been validated by the micro-CT imaging results. The tube wall profiles of the empty tube and the LNFT after tests are captured by a micro-CT imaging system (Model QuantumGX, PerkinElmer Inc.) and the wall thickness along the profiles is measured (Figure 6-10). The original wall thickness is 1.63 mm as indicated by the white color. The wall thickness of empty tube increases at folds with a maximum value of 2.31 mm and decreases to about 1.60 mm between adjacent folds. The thickness changes imply that the tube undergoes a combination of two deformation modes: severe compression at folds and slight tension between folds. The extent of thickness changes indicates that the compression at folds is dominant, while the majority of tube wall, i.e. tube wall between adjacent folds, shows little deformation. As the tube is filled with LN, the first fold (lower one) is similar to that in empty tube

due to the small amount of air trapped in LN. As the LN starts to take effect, the second fold (upper one) is formed. The buckling of LNFT is in axisymmetric mode. The wall thickness of LNFT decreases with a minimum value of 1.41 mm. Therefore, the tube wall deformation is dominated by tension mode. More importantly, over 90% of the tube wall is heavily stretched. Therefore, the plastic deformation of the tube wall is significantly improved in LNFTs compared with empty tubes.

6.4.2. Effect of Incident Speed

As previously discussed, the LNFTs show strong rate sensitivity (Figure 6-7) while the rate dependency of empty tube is only secondary (Figure 6-5). Assuming the energy absorption capacity of LN only composes of liquid infiltration into nanopores, the strengthening coefficient C is calculated as 8.7 based on Equation (6-6) and the results in Table 6-2. The C=8.7 under gas gun impact $(v=6.7\ m/s)$ is much higher than that in quasi-static (C=3.5, v=2mm/s) compression tests in current study and those in both quasi-static (C=3.5, v=2mm/min) and dynamic $(C=4.2, v=3.0\ m/s)$ tests in the previous chapter, indicating the assumption that only liquid infiltration into nanopores involves in the energy absorption mechanism of LN is invalid. There must exist additional energy absorption mechanism of the LN at such high incident speed.

Compared with quasi-static compression tests and dynamic impact test in both this study and in previous chapter, the incident speed as well as the incident energy in gas gun impact is much enhanced. The additional energy absorption mechanism associated with LN at higher incident speed and incident energy is the non-dissipative nanofluidic energy capture mechanism in LN [155,193,194,202]. Upon impact, once the P_{in} of LN is reached, the capillary resistance is overcome and the liquid molecules infiltrate into the nanopores rapidly. The highly compacted

intercalated liquid molecules is driven towards the end the nanopores as external impact progresses, carrying massive potential energy into the nanopores. Due to the mechanical impedance mismatch between the trapped liquid molecules and the rigid nanopore wall, the wave transmission is suppressed at the liquid-solid interface. Thus, the incident wave energy of the external impact is temporarily stored in the nanopores as the potential energy of the intruded liquid molecules. While the liquid infiltration is driven by the external impact at a higher flow rate, the liquid defiltration can only rely on the solid-liquid interfacial tension, leading to a much lower flow rate. Therefore, the captured potential energy is released into other forms of energy slowly and the incident energy is mitigated. The energy capture capacity increases dramatically with the incident speed, suggesting that the energy absorption capacity of LNFTs can be further enhanced at higher incident speeds. This adaptive impact mitigation ability endows LNFTs to be used as advanced energy absorber in impact conditions with different energy levels.

6.5 Summary

In this chapter, we have experimentally investigated the energy absorption capacity of large-scale LNFT at different incident speeds. The comparison of the energy absorption capacities and the strengthening coefficients between empty tubes and LNFTs allows the following conclusions to be drawn:

- The LN can improve the energy absorption capacity of the tube under both quasi-static compression and dynamic impact conditions;
- (2) The reinforcing mechanism includes load transfer effect between LN and tube wall and suppression of inwards buckling;
- (3) The LNFTs show strong rate sensitivity. As the incident speed increases, the energy absorption capacity of LNFTs is considerably enhanced;

(4) Nanofluidic energy capture mechanism of LN is involved at higher incident speed, which significantly promotes the energy absorption capacity of LN as well as LNFTs.

In summary, LN is demonstrated to be an effective filler for thin-walled tubes to enhance its energy absorption capacity, especially at elevated strain rates. The findings warrant future applications of LN under high speed impact, such as vehicle crash and even blast scenarios.

Chapter 7

LN-Functionalized Strong and Tough Hydrogel

This chapter presents an experimental study of the reinforcement and toughening effects of liquid nanofoam (LN) on a soft material - hydrogel. We employed the LN to develop novel hybrid hydrogel. The hypothesis is that by integrating nanoporous particles into the liquid-based hydrogel, LN will be formulated and encapsulated in the 3D polymer network, and thus the mechanical strength and toughness of the hybrid hydrogel will be significantly enhanced simultaneously. To test this hypothesis, hydrogels containing nanoporous silica particles have been synthesized. The extremely large energy dissipation capacity of LN-based on the liquid infiltration mechanism has been successfully converted into the toughness of the resultant hybrid hydrogel. In addition, nanoporous particles with functionalized outer surface also perform as both chemical and physical cross-linkers to reinforce the hydrogel polymer network. Its compressive strength, tensile strength, toughness, and morphology have been characterized by various experimental techniques including confined and unconfined compression tests, tensile tests and SEM imaging. Our results show that both the mechanical strength and toughness have been remarkably enhanced. This study provides the first working mechanism to independently control the strength and toughness of hydrogel, which offers a new design strategy of next-generation "soft and wet" materials with high strength and toughness.

7.1 Introduction

Hydrogels consist of 3D cross-linked polymer networks and large amount of water (>50%). Due to their unique biocompatible and biomimetic properties, hydrogels have great potential and

promise for many biomedical and industrial applications, such as wound dressing [203], scaffolds in tissue engineering [204], drug delivery [205], sensors [206], and many others. Many applications of hydrogels, such as artificial tissues and hydrogel-based soft machines, require them to carry significant loads or undergo large deformation. However, swelling of hydrogel in water usually reduces its strengths, leading to a relatively brittle structure.

During the past decades, intensive efforts have been devoted to the development of strong, tough and highly stretchable hydrogels. Many hydrogels have shown significant improvement on the toughness compared with their conventional counterpart, such as double-network hydrogel [207–209], hydrogel with reversible cross-linker [210], hydrophobically associated hydrogels [211], topological hydrogel [212], nano-composite hydrogel [213], etc. Despite their successes, it remains challenging to combine several extraordinary mechanical properties within one material, due to structural heterogeneity and lack of energy dissipation mechanisms. More importantly, nearly all researches are focused on the solid matrix network, while the water phase, which takes up most of the material, has long been ignored.

Here we propose to use LN to functionalize the water phase in the hydrogel for toughening and to physically or chemically crosslink the matrix network of the hydrogel for strengthening. Figure 7-1 shows the proposed working mechanism of LN-functionalized hydrogel. Upon external loading, the polymer chains of neat hydrogel will fracture to dissipate energy. As the hydrogel is reinforced by LN, physical and chemical crosslink will be generated between polymer chains and nanoporous particles; thus, the mechanical strength of the hydrogel can be improved and the polymer matrix can bear more load. Before the polymer chains fracture, liquid will infiltrate into the nanopores, dissipating massive energy to release the stress in the polymer network. Therefore, the toughness of the hydrogel can be significantly enhanced.

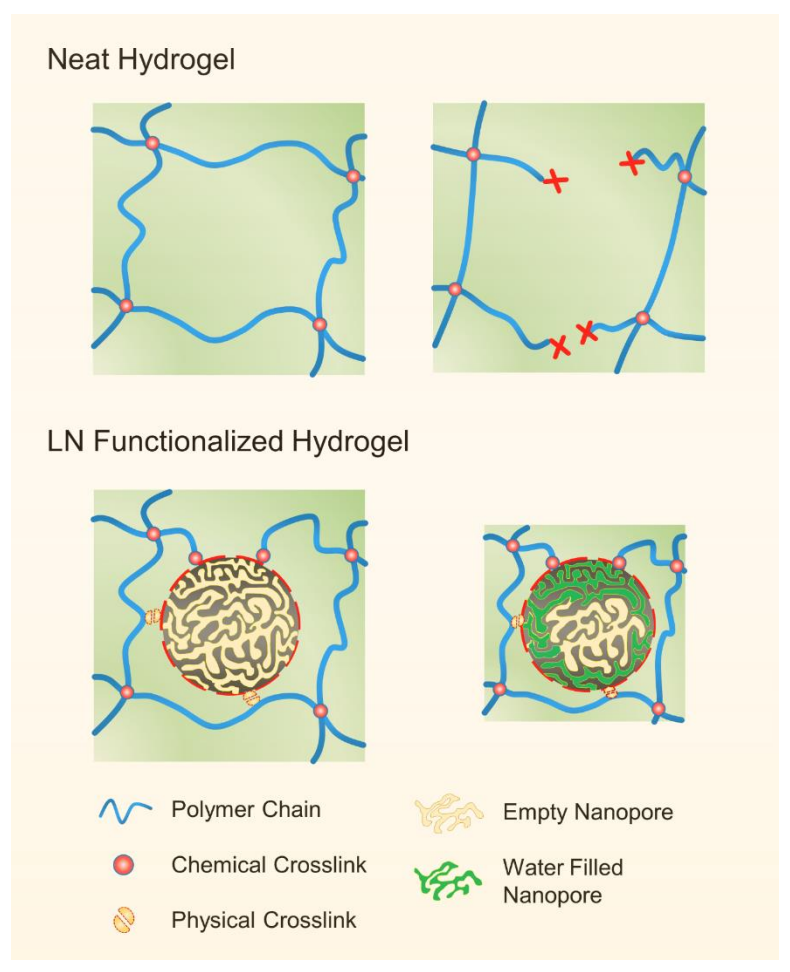


Figure 7-1: The schematic of the working mechanism of LN-functionalized hydrogel.

7.2 Materials and Methods

7.2.1. Materials and Sample Preparation

Materials: N,N'-methylenebis (acrylamide) (MBAA, 99.0%, Sigma Aldrich) was recrystallized from methanol before use. Acrylamide (AAm, 99%, Sigma Aldrich), potassium persulfate (KPS, 99%, Alfa Aesar) and Pluronic F127 (PEO₉₉-PPO₆₅-PEO₉₉, Sigma Aldrich) were used as received. The nanoporous material used in this study was a hydrophobic silica SP120 (SP-120-10, Daiso Corp.). The pore size of SP120 was around 12 nm and the particle size was about 10 μm.

Synthesis of PAAm hydrogels: Hydrogels were synthesized via a one-step sequential free radical polymerization. Firstly, various amount of silica gel SP120, 1.78 g AAm and 0.038 g

surfactant F127DA were mixed in 5 mL water. After bubbling under a nitrogen atmosphere for at least 30 min, 0.1 mol% of the initiator potassium persulfate (KPS) with respect to AAm were added into the mixture. Using a syringe, the solution was injected into a mold fabricated by spacing two glass plates with a silicone rubber spacer. The mold was heated at 50 °C for 12 h in a water bath for the polymerization and gelation.

7.2.2. Test Procedures

Scanning electron microscopy (SEM) imaging: The hydrogel samples were quenched by liquid nitrogen, and then freeze dried to maintain the porous structure of the polymer network. The dry hydrogel was coated with a layer of platinum before scanning with a Carl Zeiss EVO LS25 Scanning Electron Microscope.

Compression test: The test samples were cylindrical with a diameter of 15 mm and thickness of 8 mm. The unconfined compression tests were conducted by an Instron 5982 universal tester at a constant loading rate of 2 mm/min. The confined compression tests were conducted by placing the sample into a testing cell (Figure 2-4), which was then compressed by the Instron machine.

Tension test: The test samples were cut into dumb bell shape with a gauge length of 20 mm, a width of 5 mm and a thickness of 1.5 mm. The loading speed was 500 mm/min.

7.3 Results and Discussions

7.3.1. Quasi-Static Behavior of LN

Figure 7-2 shows typical sorption isothermal curves for the silica gel used in current study SP120 in F127 aqueous solution. Since the sorption isothermal curves of all subsequent cycles are nearly identical to that of the second cycle, only the curves of first two cycles are shown here.

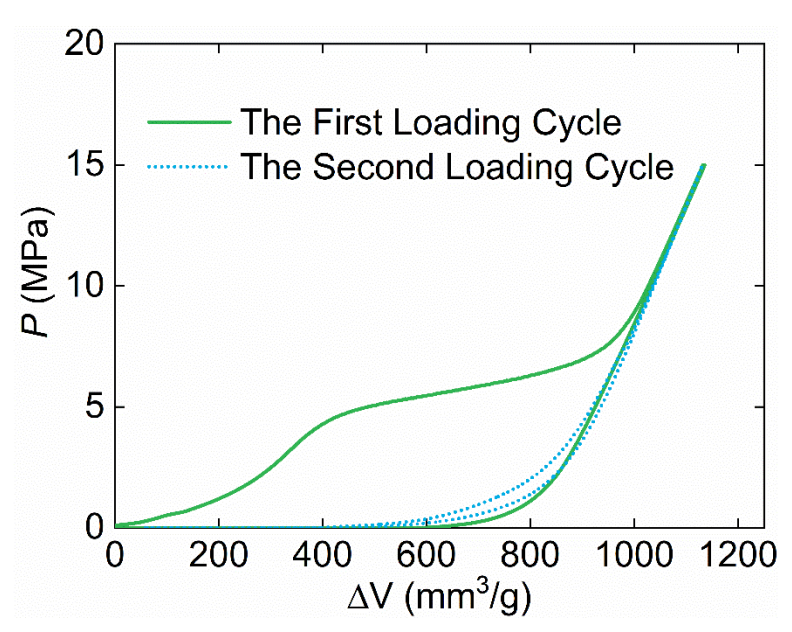


Figure 7-2: Typical sorption isothermal curves of the silica gel SP120 in F127 aqueous solution.

As shown in Figure 7-2, in the first loading cycle, as the external pressure is sufficiently high to overcome the energy barrier, the liquid can be driven into the nanopores, leading to the formation of a liquid infiltration plateau. From Figure 7-2, the infiltration pressure of the LN, P_{in} , in first loading cycle is about 5 MPa. The specific volume change of liquid infiltration, ΔV_{sp} , is around 0.6 cm³/g. During the second loading cycle, no liquid infiltration can be observed, indicating the nonoutflow of liquid during the first unloading. As the liquid infiltration plateau is clearly observed in the first loading cycle, we have validated that the nanopores contained by SP120 are available for toughness improvement in the synthesized LN-functionalized hydrogels.

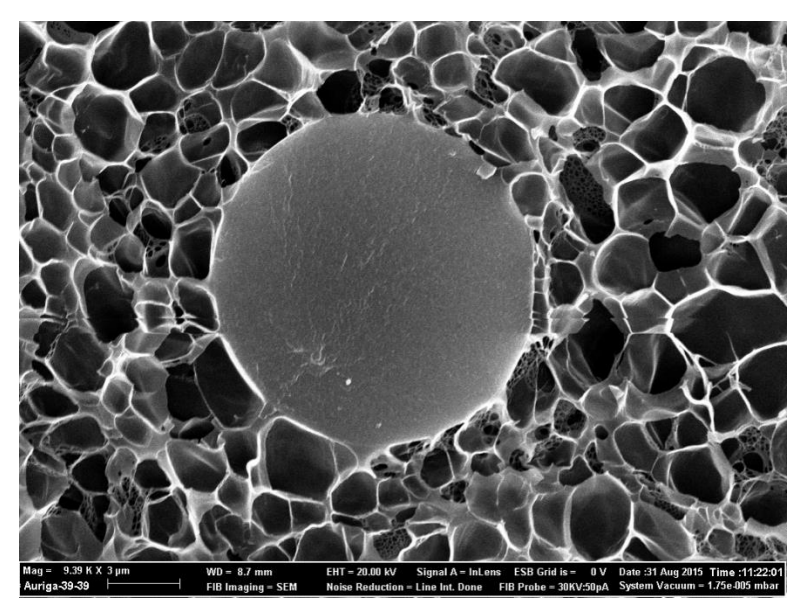


Figure 7-3: SEM image of LN (SP120 in F127 aqueous solution) functionalized PAAm hydrogel.

7.3.2. Morphology

Figure 7-3 shows the porous microstructure of LN-functionalized hydrogel. It can be observed that the nanoporous particle SP120 has been successfully incorporated into the polymer network without distortion. Importantly, the polymer chains are connected with the particle via chemical or physical crosslinks, indicating that the reinforcement effect is due to the enhanced polymer-particle interaction.

7.3.3. Mechanical Properties

The unconfined compressive stress-strain curves of LN-functionalized PAAm hydrogels are shown in Figure 7-4. It can be observed that the silica gel reinforced PAAm hydrogels possessed excellent compressive properties. The fracture stress of LN-functionalized PAAm hydrogel (2 wt%) is 28 MPa, leading to nearly 200% increase, compared with neat PAAm hydrogels (10 MPa). These results are in good agreement with the morphological observations exemplified in Figure 7-3, where the nanoporous particles behave as physical or chemical crosslinkers. As shown in Figure 7-4, further increasing the amount of silica gel SP120 leads to the decrease of the fracture stress of PAAm hydrogel since too much nanoporous particles affect the polymerization process.

As the true fracture stress, by considering the large lateral expansion of the specimen during test, is relatively low compared with the P_{in} of silica gel SP120, liquid infiltration is not triggered in this unconfined compression test and no plateau can be observed.

Figure 7-5 shows the LN-functionalized hydrogel can undergo 90% of strain without fracture and recover to its initial state. This has demonstrated that the hydrogel can be applied to cyclic loading conditions.

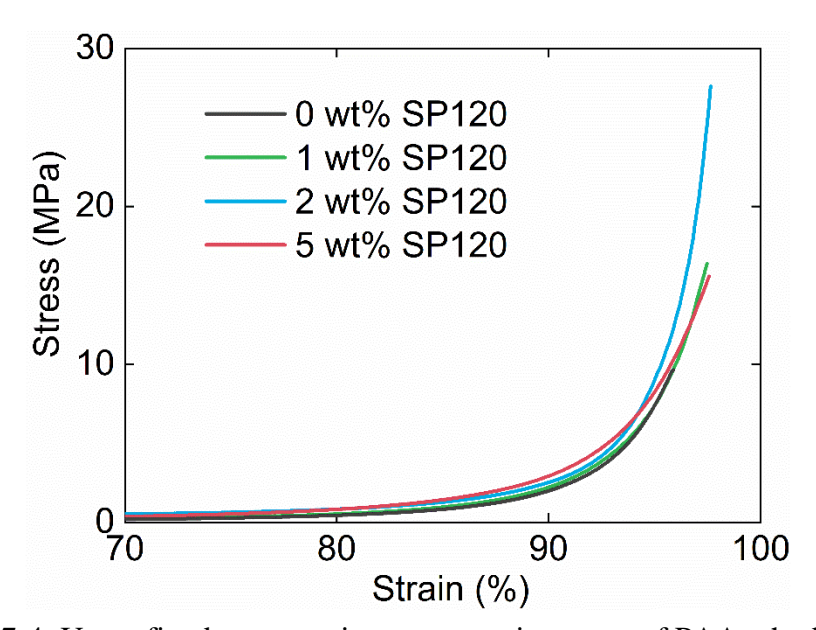


Figure 7-4: Unconfined compressive stress-strain curves of PAAm hydrogels.

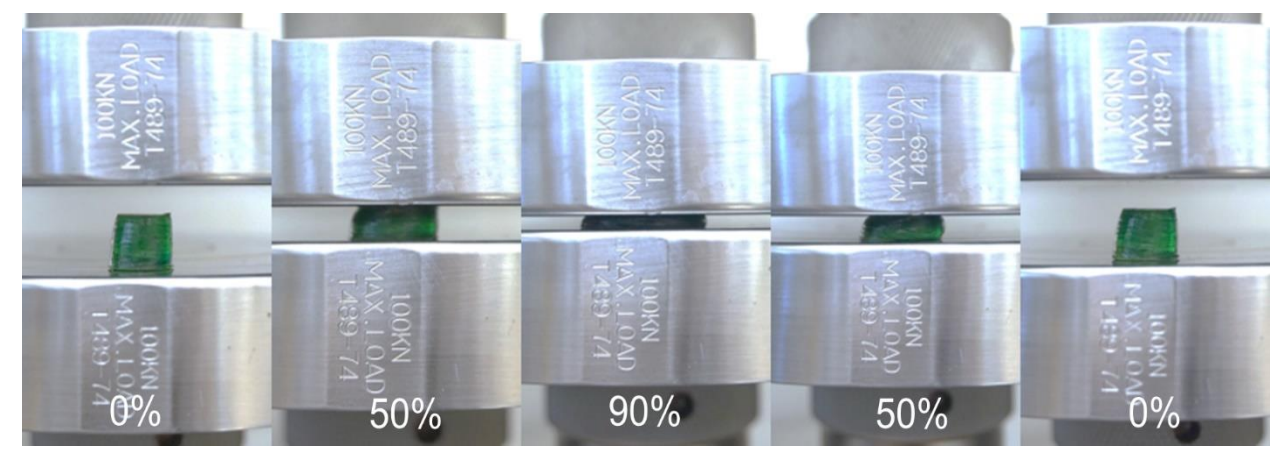


Figure 7-5: The recovery ability of LN-functionalized PAAm hydrogels under unconfined compression.

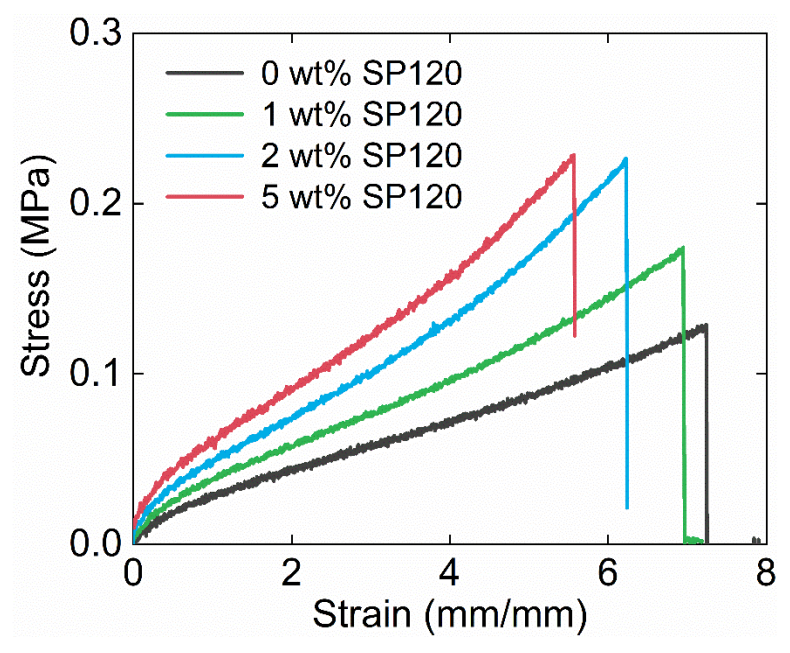


Figure 7-6: Tensile stress-strain curves of PAAm hydrogels.

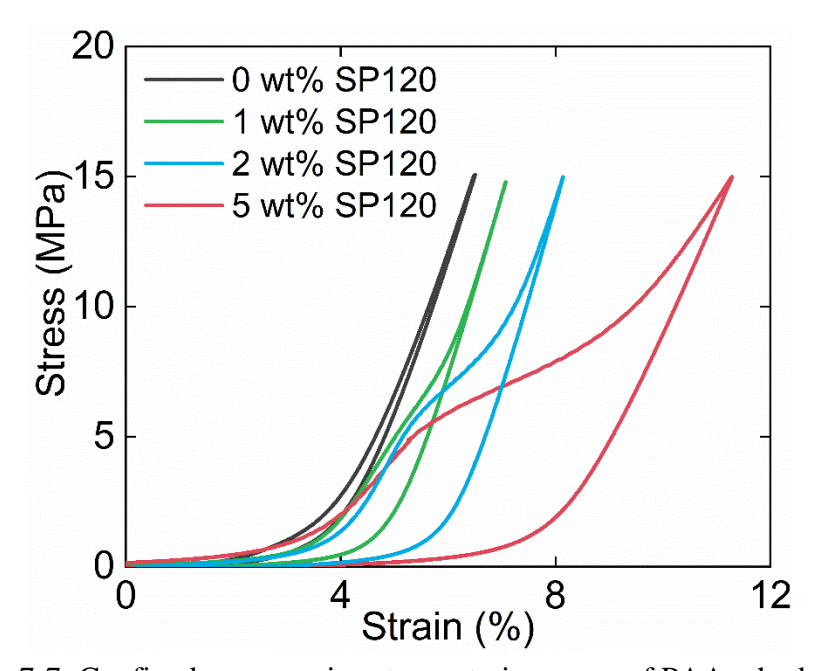


Figure 7-7: Confined compressive stress-strain curves of PAAm hydrogels.

The tensile stress-strain curves of LN-functionalized PAAm hydrogels are shown in Figure 7-6. The tensile strength has been improved by adding silica gel SP120. The fracture stress of LN-functionalized PAAm hydrogel (2 wt%) is 0.22 MPa, leading to 70% increase, compared with neat

PAAm hydrogels (0.13 MPa). The results are consistent with the compression tests as well as the observed microstructure of the material.

Figure 7-7 shows the confined compressive stress-strain curves. When an isotropic hydrostatic pressure is applied, the hydrogel deforms and the system free energy increases as the strain energy is stored. If there exist small voids in the material, the liquid molecules tend to diffuse from the high-energy region (the hydrogel network) to the low-energy region (the small voids). As the neat PAAm hydrogel is compressed, since there is no voids in the network, the sorption isotherm curve increases quite linearly except for the initial concave section; upon unloading, the curve almost coincide with the loading curve. Therefore, the neat PAAm hydrogel shows little energy absorption capacity under hydrostatic pressure condition. As the LN-functionalized PAAm hydrogel is compressed, initially when the pressure is low, liquid molecules cannot overcome the capillary resistance to infiltrate into the nanoporous silica, the sorption isotherm curve increases quite linearly. As the pressure reaches 5 MPa, the slope of the sorption isotherm curve decreases suddenly, indicating that the pressure induced infiltration begins. Due to the pore size distribution, the plateau shows a positive slope. When the pressure reaches 9 MPa, most of the pores are saturated and the system compressibility decreases rapidly. The pressure range of the infiltration plateau coincide with that of silica gel SP120 in F127 aqueous solution as shown in Figure 7-2, suggesting that this process is dominated by the confined water molecules infiltrating into nanopores. The unloading behavior is quite linear, similar to the F127 solution-based nanoporous system. The curve is highly hysteretic, resulting in huge amount of absorbed energy (Figure 7-8). By increasing the amount of silica gel SP120, the width of the infiltration plateau is increased accordingly. After the confined compressive test, the hydrogels do not fracture (Figure 7-9).

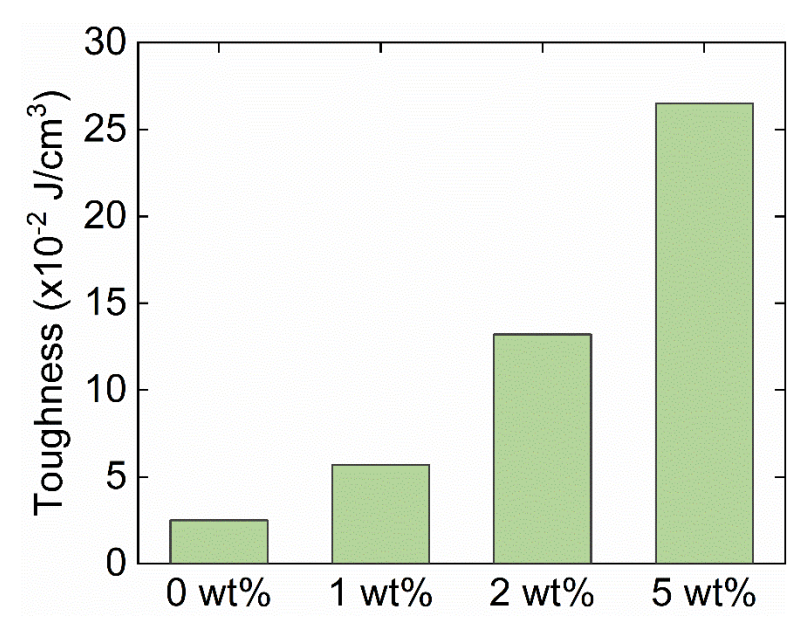


Figure 7-8: The toughness of LN-functionalized PAAm hydrogels.

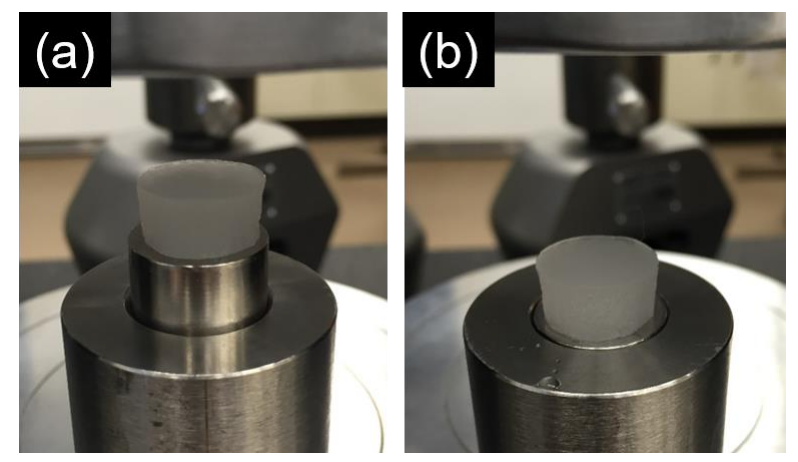


Figure 7-9: LN-functionalized PAAm hydrogels (a) before confined compression test (b) after confined compression test.

7.4 Summary

In this chapter, we have experimentally investigated the performance of LN-functionalized hydrogels. By various experimental techniques including confined and unconfined compression tests, tensile tests and SEM, we have demonstrated:

(1) LN is formulated and encapsulated in the 3D polymer network by integrating nanoporous particles into the liquid-based hydrogel;

- (2) Nanoporous particles also perform as both chemical and physical cross-linkers to reinforce the hydrogel polymer network;
- (3) Toughness of the hybrid hydrogel will be significantly enhanced due to the liquid infiltration mechanism.

In short, the LN is a promising filling material for hydrogels to independently control the strength and toughness, which shed light on the design of next-generation "soft and wet" materials with combined superior mechanical properties.

Chapter 8

LN-Functionalized Seat Belt Retractor System

This chapter presents a novel design of liquid nanofoam (LN)-functionalized seat belt retractor system. LN has been employed as the load-bearing component to allow for additional seat belt payout in the retractor system. The new retractor system have been demonstrated to be much more tunable compared with traditional torsion bar. It can be potentially developed into personalized belt retractor systems for better occupant protection.

8.1 Introduction

The increasing demand for advanced transportation has led to enormous growth in the numbers of vehicles in modern society. Inevitably, vehicle crashes are also increasing and have become one of the leading causes of death. Therefore, numbers of researchers have been devoted to traffic safety and occupant protection. In a vehicle, the seat belt system (Figure 8-1a) is one of the most important safety devices. During a collision or sudden stop, the seat belt system will secure the passenger against harmful movement. Wearing a seat belt can dramatically reduce the risk of death and serious injury (Figure 8-2). In a seat belt system, the seat belt retractor (Figure 8-1b) is the key component which controls the belt behavior. During a crash, the seat belt retractor will lock up. A torsion bar (Figure 8-1c), which is subjected to nonlinear twisting mode of deformation, is usually used to allow for additional seat belt payout after the retractor is locked.

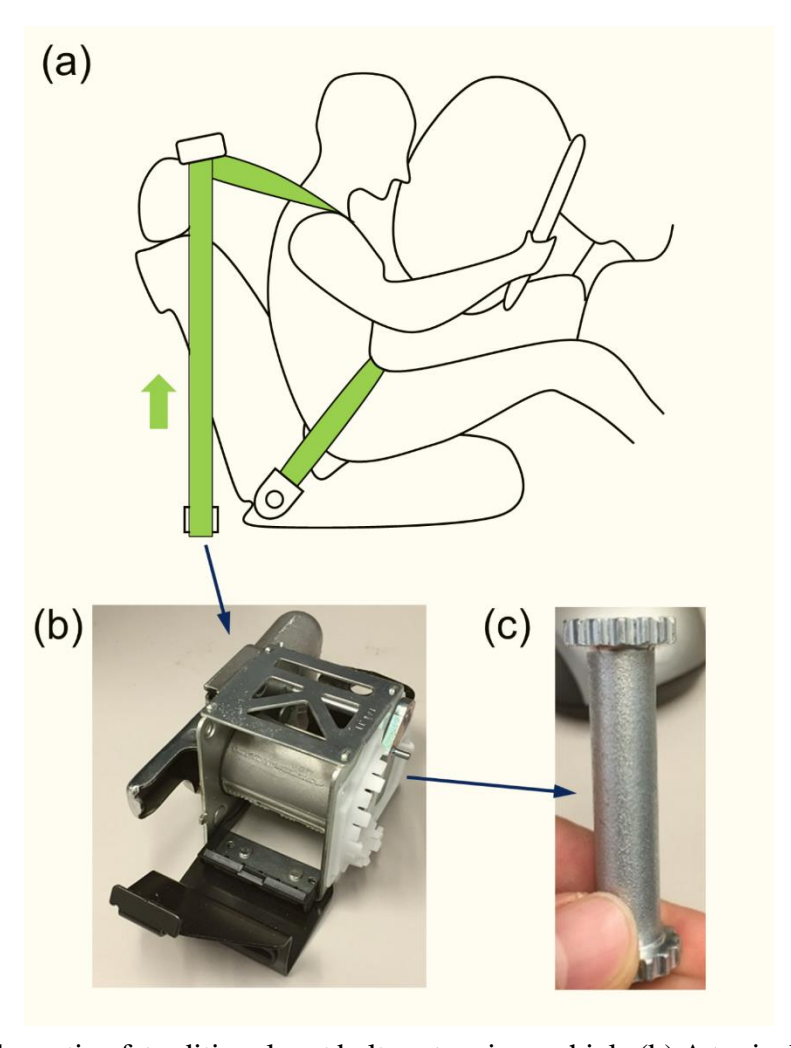


Figure 8-1: (a) Schematic of traditional seat belt system in a vehicle (b) A typical seal belt retractor (c) A typical torsion bar.

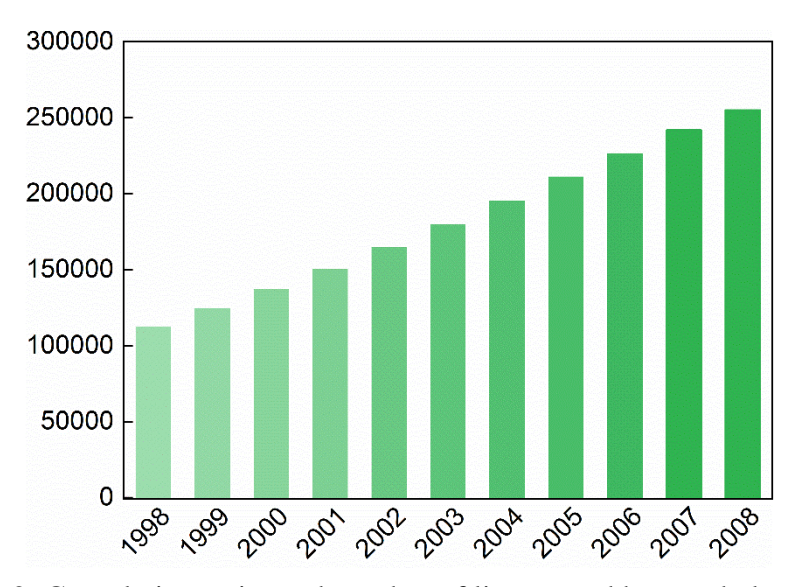


Figure 8-2: Cumulative estimated number of lives saved by seat belt use [214].

However, there are several problems in current seat belt retractor system.

- (1) Since the torsion bar is metallic and it deforms plastically during a crash, it is only good for one-time use.
- (2) More importantly, it is usually difficult and expensive to design an adaptive torsion bar in current seal belt system.

Here we propose to use LN to substitute current metallic torsion bar due to the following advantages of LN.

- (1) High tunability. The LN has controllable performance and the control parameters include pore size [78,215], surface coverage [56,115,216], viscosity of the liquid phase [82,217], temperature [110,149,152,218–220], ion concentration of the liquid phase [116,180,221,222], etc.
- (2) Small size. The size of nanoporous particles is in the micron level. Importantly, the LN shape can adapt to systems with any shape.
- (3) Reusability. With proper surface treatment of the nanoporous materials, the LN can be fully reusable.

8.2 Design

8.2.1. Design of LN-Functionalized Seat Belt Retractor System

The proposed solution is to use LN-functionalized device instead of a traditional torsion bar to allow load limiting without any plastic deformation once the retractor is locked during crashes. Note that this design only replaces the torsion bar and keeps other parts of a traditional retractor unaltered. As shown in Figure 8-3, the LN-functionalized device consists of a chamber containing LN and a threaded piston. The piston is partially screwed into the chamber, leading to the compression of the LN. The LN chamber engages with the housing through a gear mechanism.

This ensures the LN chamber will rotate as the spool is pulled. In current design the other end of the piston is locked up to demonstrate the working performance after the retractor is locked. (Note that in final product, this end is engaged to the inertia locking mechanism. In normal operation, this end is also completely free to rotate. Therefore, when the seat belt is slowly pulled, both LN chamber and piston rotate and the piston will not screw into the LN chamber.)

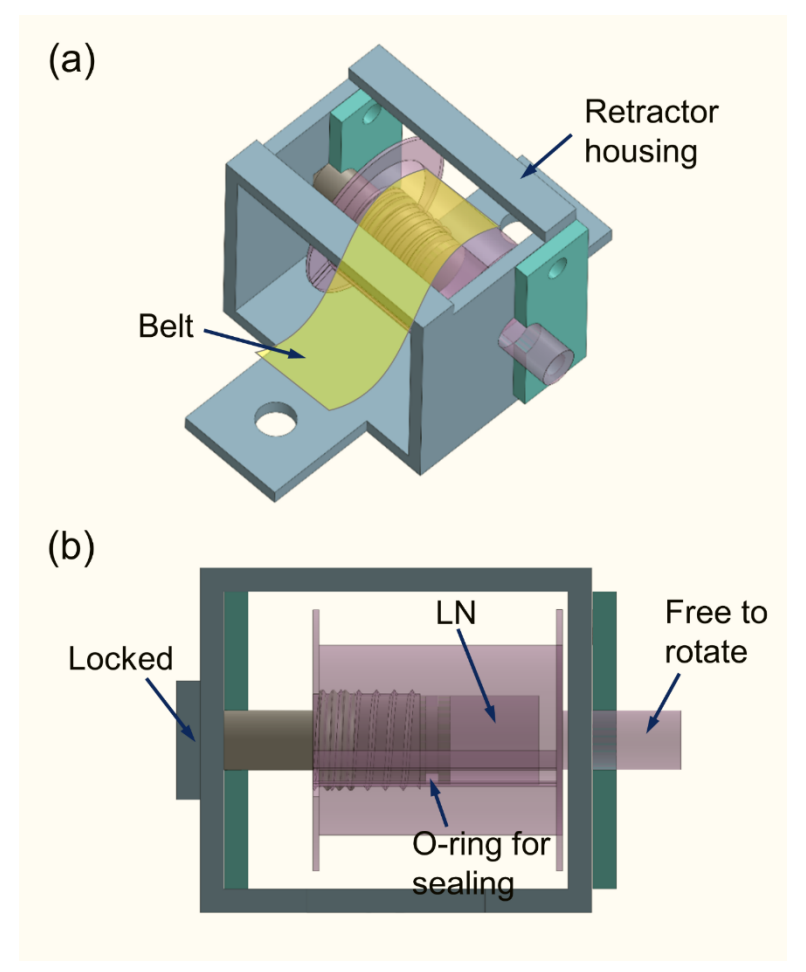


Figure 8-3: The LN-functionalized seat belt retractor assembly (a) with retractor housing and belt (b) a front view.

As the seat belt retractor locks up during a crash, the piston cannot rotate with the LN chamber and the spool. As such, the LN chamber will rotate towards the piston, causing the piston screwed into the LN chamber. Consequently, the LN inside will be subjected to hydrostatic pressure. When the pressure reaches the P_{in} of the LN, the load will be maintained around a constant value.

Continuing movement of the occupant leads to additional seatbelt payout. When the pores are filled with liquid, the LN becomes incompressible. The spool rotation will stop and no further seat belt payout is allowed.

8.2.2. Selection of LN for Desire Belt Retraction

The working load limit of the seat belt retractor, F_1 , is determined by the working pressure, P_{in} , of LN, as shown in Figure 8-4.

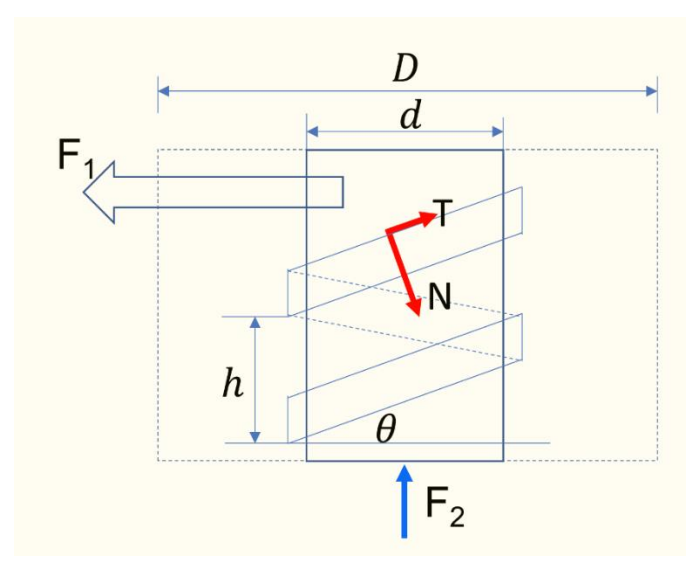


Figure 8-4: Schematic of the force relation in the LN-functionalized seat belt retractor.

Here, we have

$$F_1 = \frac{d}{D} \ N \cdot sin\theta + T \cdot cos\theta \ = \frac{d}{D} N \ sin\theta + \mu \cdot cos\theta \ 8 - 1$$

$$F_2 = N \cdot cos\theta + T \cdot sin\theta = N \ cos\theta + \mu \cdot sin\theta \tag{8-2}$$

$$F_2 = P_{in} \cdot \frac{\pi d^2}{4} \qquad \qquad 8 - 3$$

Therefore,

$$\begin{split} F_1 &= \frac{\mu \cdot \cos\theta + \sin\theta}{\cos\theta - \mu \cdot \sin\theta} \cdot \frac{d}{D} \cdot F_2 \\ &= \frac{\mu \cdot \cos\theta + \sin\theta}{\cos\theta - \mu \cdot \sin\theta} \cdot \frac{d}{D} \cdot P_{in} \cdot \frac{\pi d^2}{4} \end{split}$$

$$\begin{split} &= \frac{\mu \cdot cos\theta + sin\theta}{cos\theta - \mu \cdot sin\theta} \cdot \frac{\pi d^3}{4D} \cdot P_{in} \\ &= \alpha \cdot P_{in} \end{split}$$
 8 - 4

The seal belt payout is determined by the nanopore volume of the LN by

$$\begin{split} L &= \frac{4D \cdot V_{sp}}{\pi d^3 \cdot sin\theta} \\ &= \beta \cdot V_{sp} \end{split}$$
 8 – 5

The dimensions of the LN-functionalized device and the LN selection can be optimized to achieve the required performance targets. Here we have selected two LN candidates to meet the requirements.

Table 8-1: The LN candidates used in this study.

| Silica Gel | Pore Size (nm) | Liquid Phase | P_{in} | ΔV_{sp} |
|------------|----------------|--------------|----------|-----------------------------|
| SP300 | 30 | 35 wt% LiCl | ~10 MPa | $0.7 \text{ cm}^3/\text{g}$ |
| SP120 | 12 | 46 wt% LiCl | ~30 MPa | $0.7 \text{ cm}^3/\text{g}$ |

The mechanical properties of the LN candidates are shown in Figure 8-5.

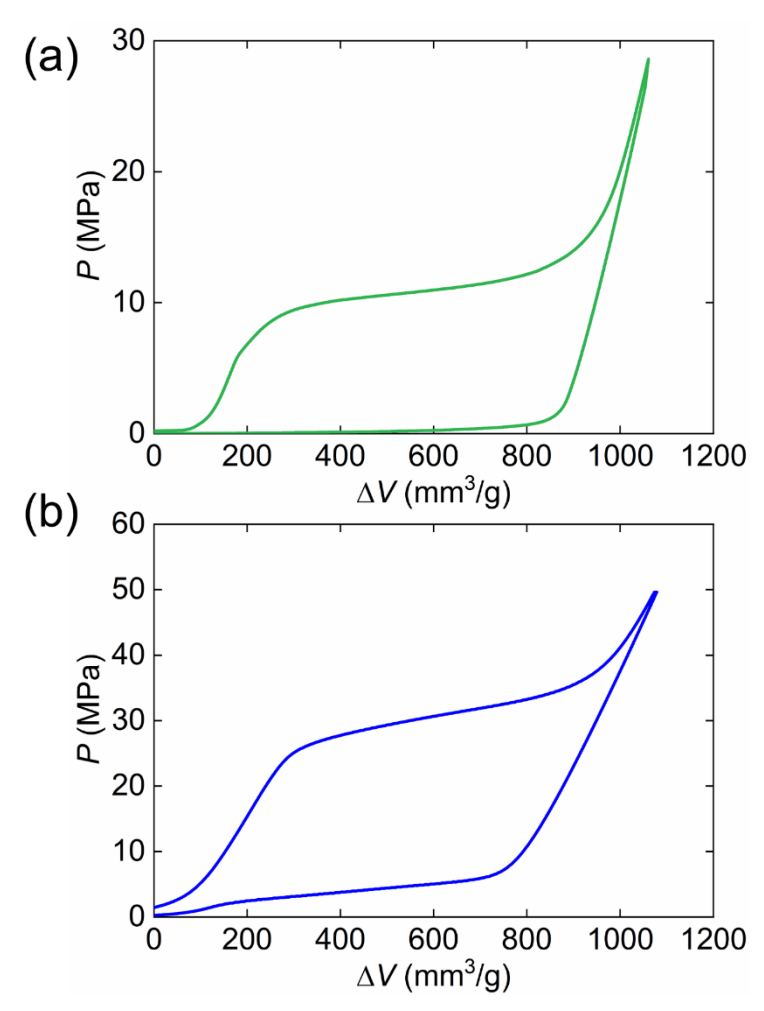


Figure 8-5: Typical sorption isothermal curves of the LN candidates (a) SP300-based LN (b) SP120-based LN.

8.3 Pulling Test Setup for LN-Functionalized Belt Retractor System

LN consisting of 1.5 g of silica gel and 4.5 g of liquid was added into the LN chamber and sealed by the piston equipped with O-rings. The belt pulling test was conducted by a universal tester (Floor Model 5982, Instron, Inc.) at a constant speed of 500 mm/min, as shown in Figure 8-6. The load F and the seat belt payout L were measured and recorded by the Instron machine.



Figure 8-6: Snapshot of the belt pulling test.

8.4 Results

Figure 8-7 shows the mechanical response of LN-functionalized seat belt retractor. As shown in Figure 8-7a, initially, the seat belt showed an elastic behavior since P_{in} of SP300 silica gel was not reached and the system behavior was the combination of the elastic nanoporous particles and liquid phase. As the external load reached a critical value 0.3 kN, the capillary effect of the nanoporous silica gel was overcome and the liquid was driven into the nanopores. Consequently, a force plateau was observed. Once all nanopores were filled, the system became incompressible and no more seat belt payout was allowed. The width of the force plateau, determined by the specific nanopore volume of the silica gel specimens, was the seat belt payout L. For SP300-based LN, $L=270\ mm$. The working load limit F, determined by the force plateau, was 0.3 kN. The

mechanical response of SP300 ensembled the behavior of traditional torsion bar-based seat belt system.

As the LN changed to SP120-based system (Figure 8-7b), F increased to 1.2 kN due to the increased P_{in} of SP120 silica gel. Since the specific nanopore pore volume of SP120 silica gel was similar to that of SP300 silica gel, the seat belt payout remained the same.

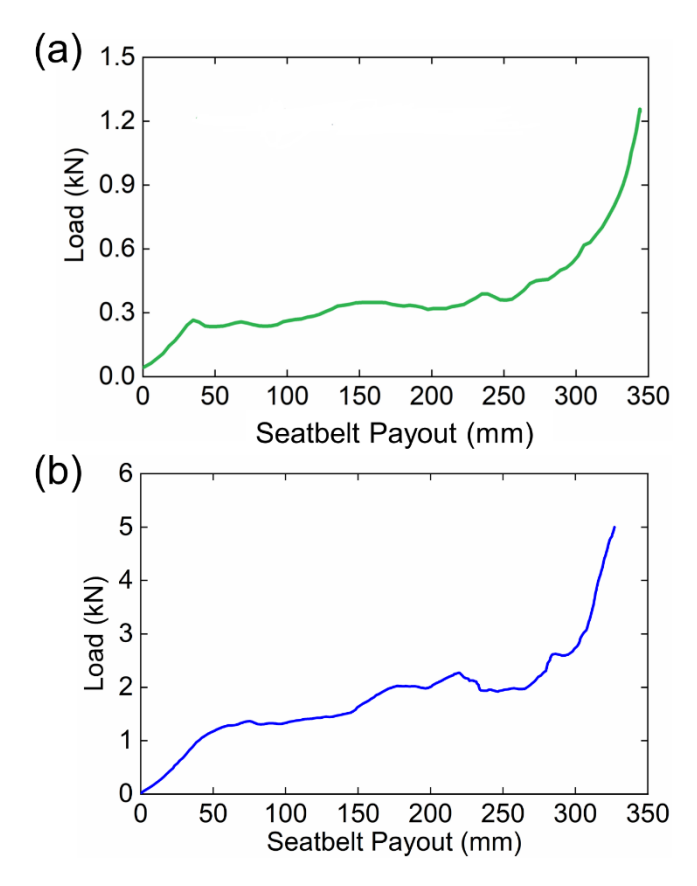


Figure 8-7: The mechanical response of LN-functionalized seat belt retractor (a) SP300-based LN (b) SP120-based LN.

Based on these results, the concept of LN-functionalized seat belt retractor has been validated. More importantly, it has been observed that as the LN material changed, the response of LN-functionalized seat belt retractor changed accordingly; that is, the LN-based system can be easily tuned.

8.5 Summary

In this chapter, we have presented a novel design of seat belt retractor system based on LN system. Through seat belt pulling test on the LN-functionalized seat belt retractor system, we have demonstrated:

- (1) The concept of LN-functionalized seat belt retractor system is valid and LN can be used as material to replace the traditional metallic torsion bar;
- (2) The LN-functionalized seat belt retractor system possesses high tunability compared with tradition metallic torsion bar;
- (3) LN can be applied in scenarios where the dominating load mode is torsion.

In short, the LN is an excellent functioning material in seat belt retractor system and many other similar applications. The results have merit in the design of advanced vehicle devices for occupant protection.

Chapter 9

Conclusions and Future Work

The research presented in this dissertation has led to knowledge on the dynamic behavior of LN system and the performance of LN-functionalized materials and structures. The research findings have provided new concepts for the development of advanced energy absorption materials and structures.

9.1 Contributions

Based on the results in this dissertation, the following conclusions can be drawn:

- (1) Dynamic behavior: Liquid infiltrates into nanopores, independent of the axial buckling stress of the nanopore and the activation of liquid infiltration as well as liquid flow in nanopores are faster than pore deformation. The much-enhanced liquid flow speed in nanoenvironment and the adaptive liquid infiltration speed are experimentally validated, providing mechanistic explanation for the high energy absorption efficiency of LN at high, blast impact-level. The research also suggests that the LN in the liquid marble form can perform as an efficient energy absorption system upon high strain rate impact due to its macroscopically homogenous structure.
- (2) LN-functionalized materials and structures: The LN filler can significantly promote the average post-buckling strength of the tube under both quasi-static and dynamic conditions due to enhanced LN-tube wall interaction. The strengthening coefficient of LNFT is much higher than that of best solid foam-filled tube because of the "perfect bonding" between LN and tube wall. As the incident speed increases, the energy absorption capacity of

LNFTs is considerably enhanced, suggesting LN is more efficient at elevated strain rates. LN can be formulated and encapsulated in hydrogel and improve both the strength and toughness of the hybrid hydrogel. LN applied in torsion mode is also demonstrated in the seat belt retractor system.

9.2 Limitations

While the LN system is proposed to work under any loading conditions, there are still limitation of the current research.

- (1) Dynamic behavior: The maximum incident speed of impact on LN in this dissertation is 3.0 m/s and the maximum strain rate is 5.8×10³ s⁻¹. The LN system may be subjected to more severe impact or even blast in real scenario.
- (2) LN-functionalized materials and structures: The maximum impact speed for LN tube is 6.7 m/s, which may be much larger in real case. The liquid infiltration in LN-functionalized hydrogel under unconfined compression tests has not been triggered.

9.3 Future Work

9.3.1. High Strain Rate Test

As previously mentioned, in practical applications, the LN system may experience impact with much higher strain rate. More importantly, results in previous chapters show that the LN system as well as LNFTs are rate sensitive (Figure 9-1a). Therefore, it is desirable to conduct dynamic test with higher strain rate. Split Hopkinson pressure bar [223–225] and blast test [226–228] are suitable experimental techniques for this purpose.

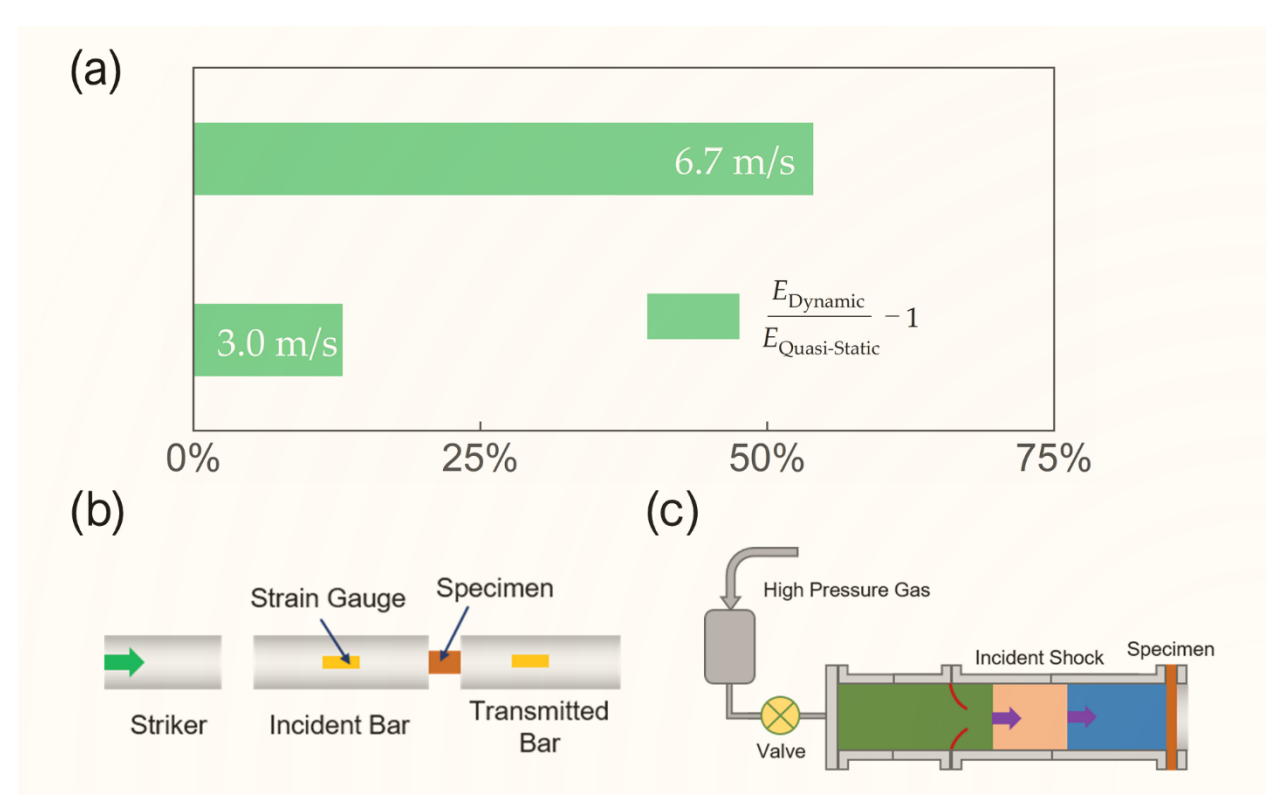


Figure 9-1: (a) Rate sensitivity in LNFTs. (b) Schematic of split Hopkinson pressure bar. (c) Schematic of experimental set-up of blast test.

9.3.2. Liquid Infiltration in Hydrogel under Unconfined Compression

As previous discussed, liquid infiltration in LN-functionalized hydrogel under unconfined compression tests has not been triggered. Therefore, the future goal is to trigger this liquid infiltration from four aspects as shown in Figure 9-2: select strong matrix, load sufficient amount of nanoporous particles, find LN system with lower P_{in} and develop effective method for dispersion.

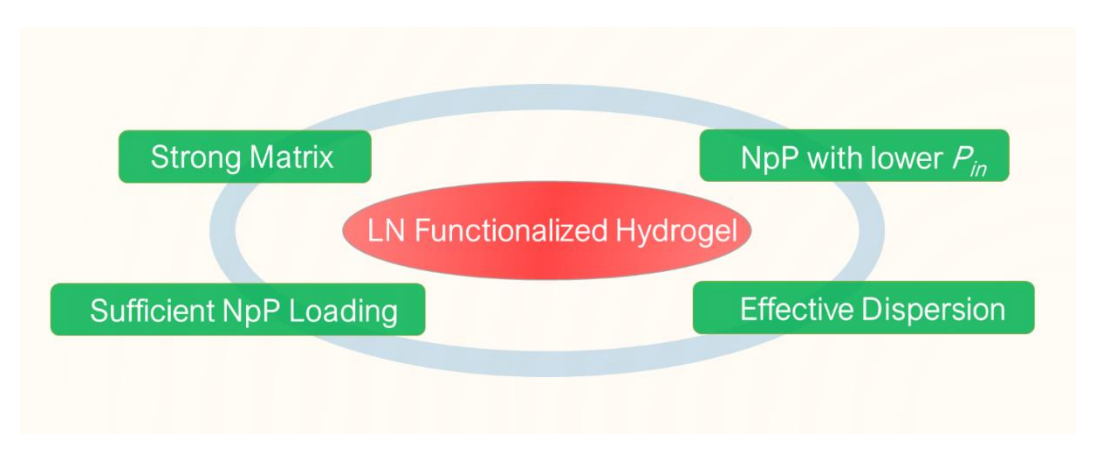


Figure 9-2: Triggering liquid infiltration in hydrogel under unconfined compression from four aspects.

APPENDIX

APPENDIX

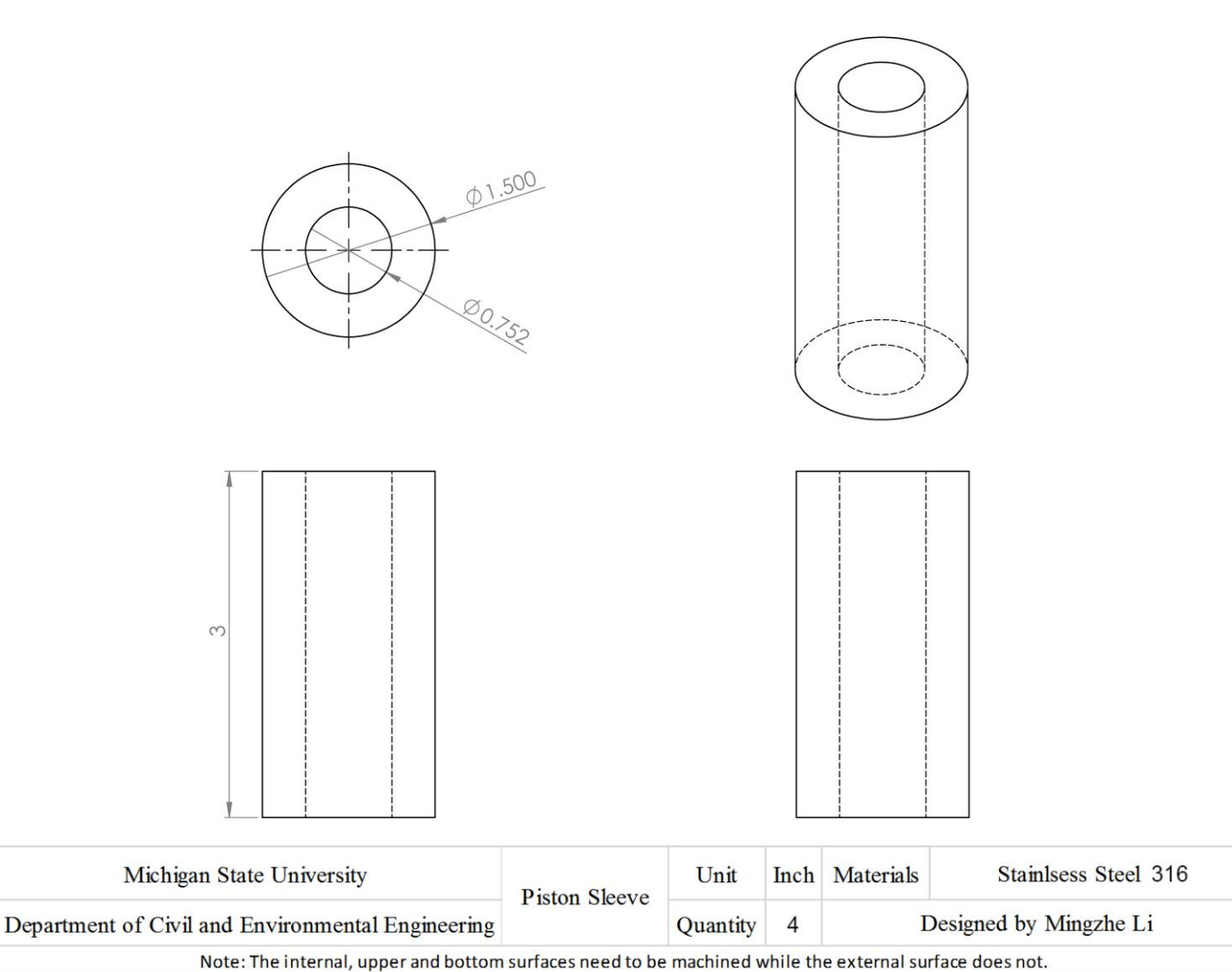
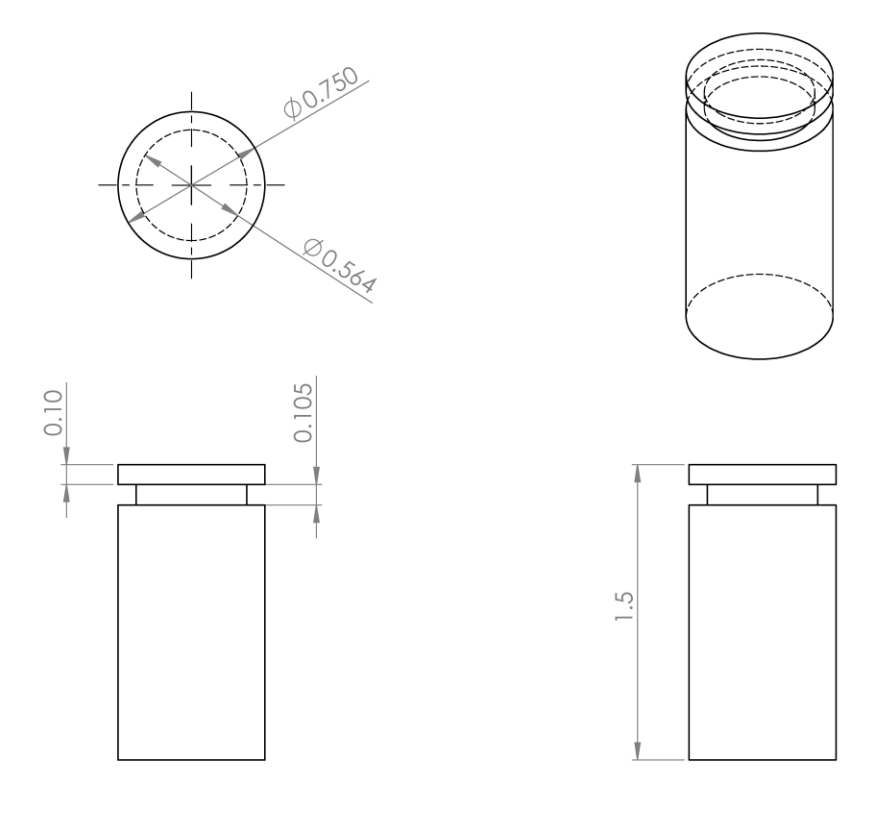


Figure A-1: Testing cell – piston sleeve.



| Michigan State University | Piston | Unit | Inch | Materials | Stainlsess Steel 316 |
|---|--------|----------|------|-----------|------------------------|
| Department of Civil and Environmental Engineering | | Quantity | 8 | | Designed by Mingzhe Li |
| Note: All surfaces need to be machined. | | | | | |

Figure A-2: Testing cell – piston.

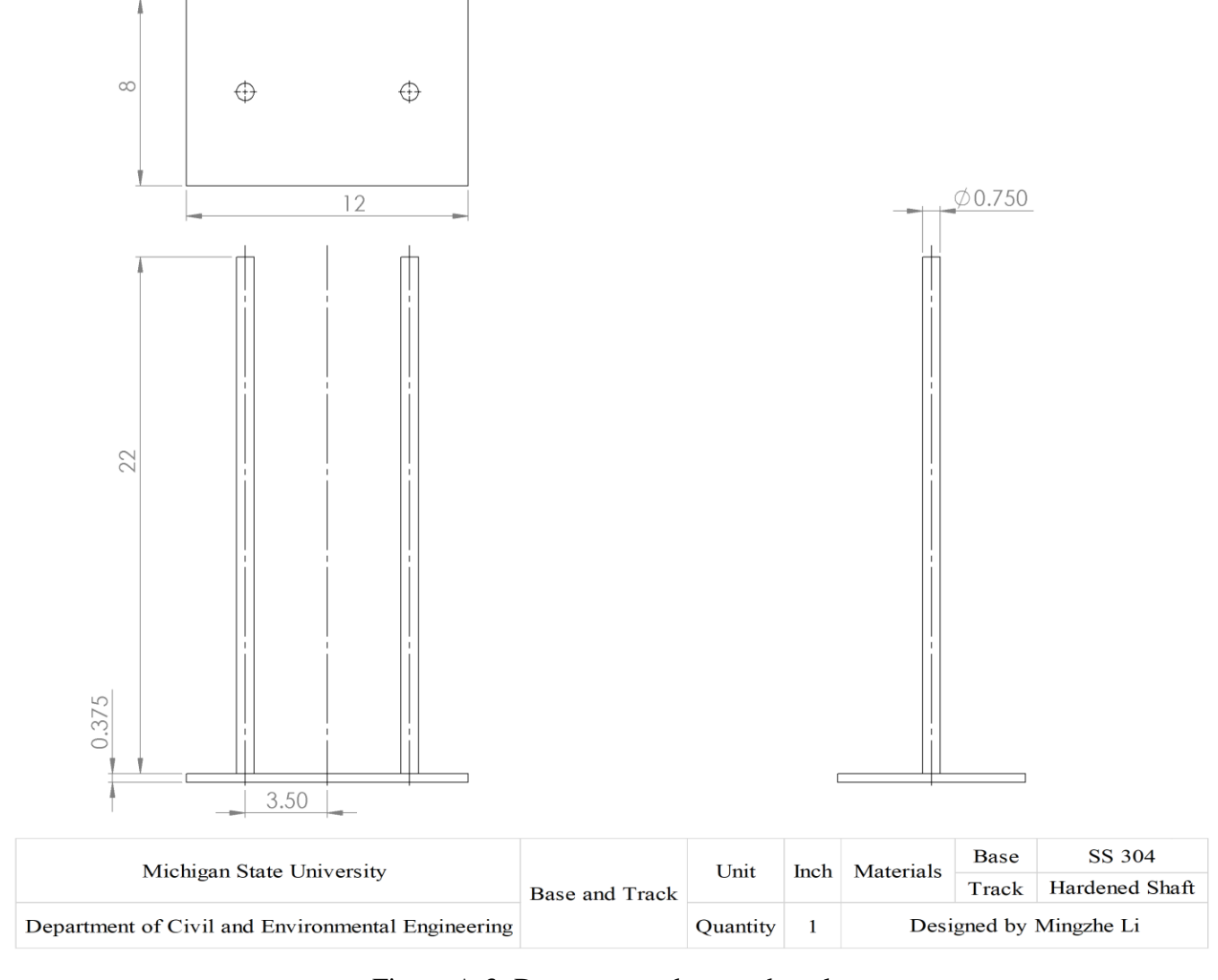


Figure A-3: Drop tower – base and track.

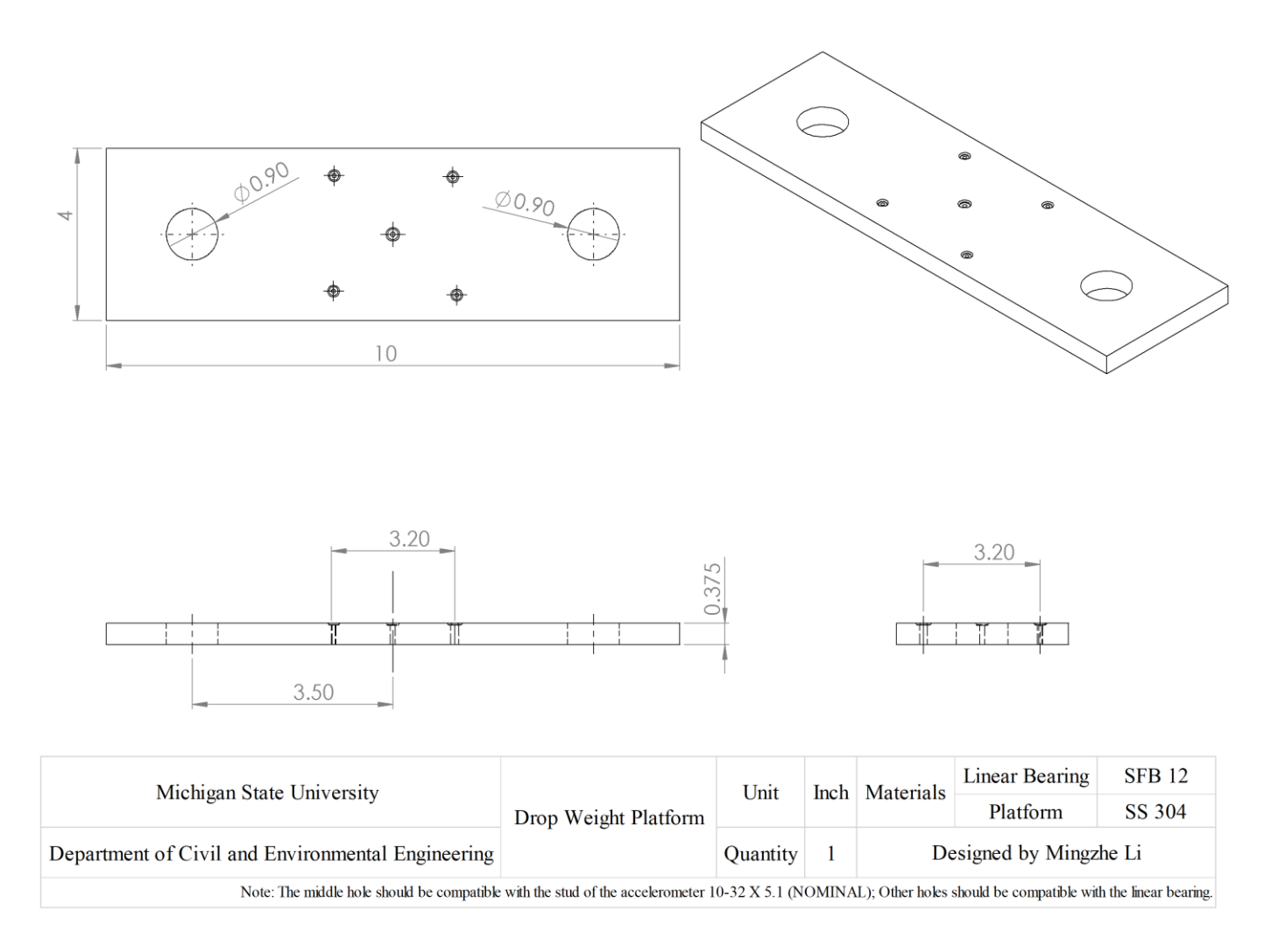


Figure A-4: Drop tower – drop weight platform.

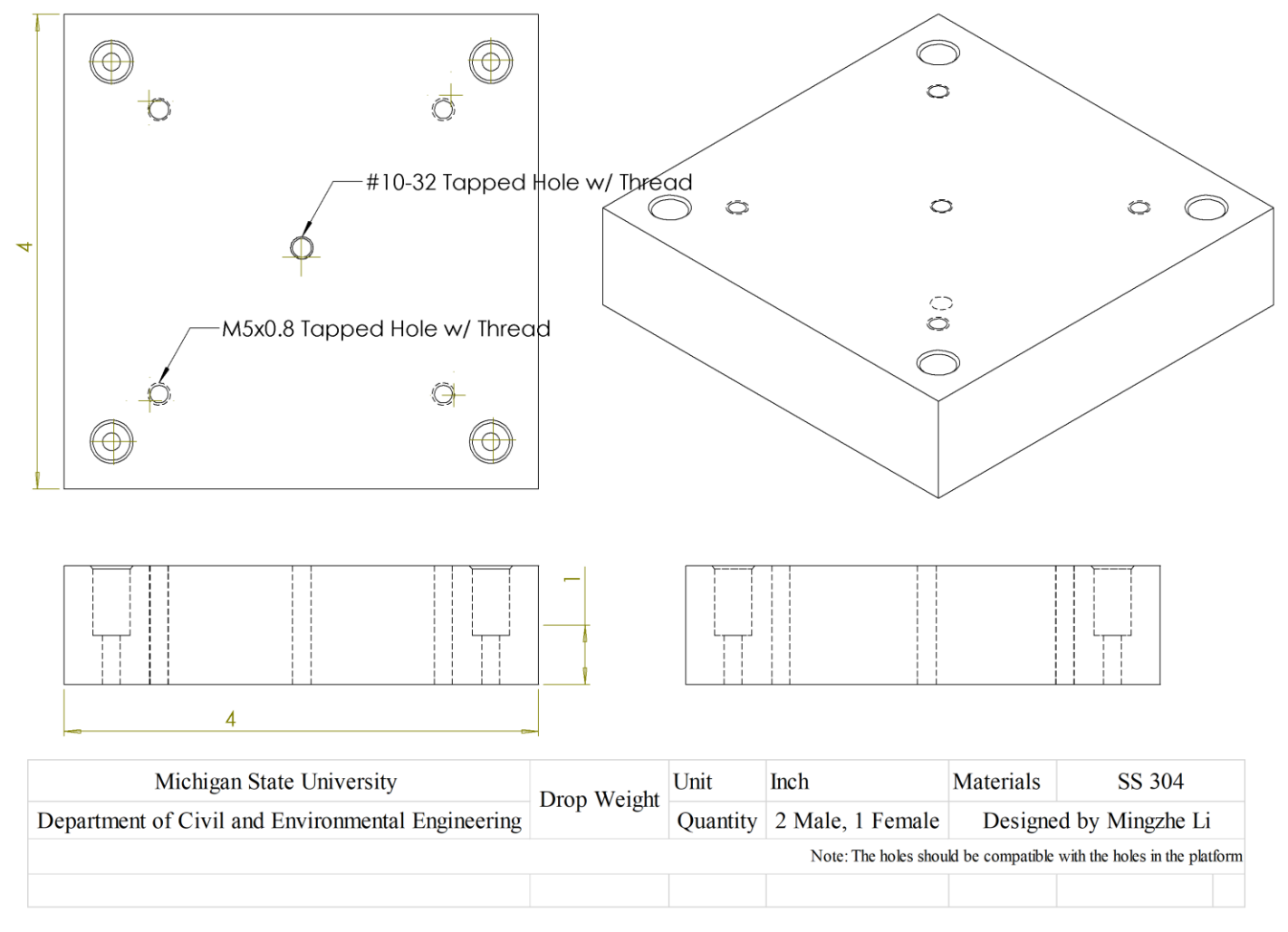


Figure A-5: Drop tower – drop weight.

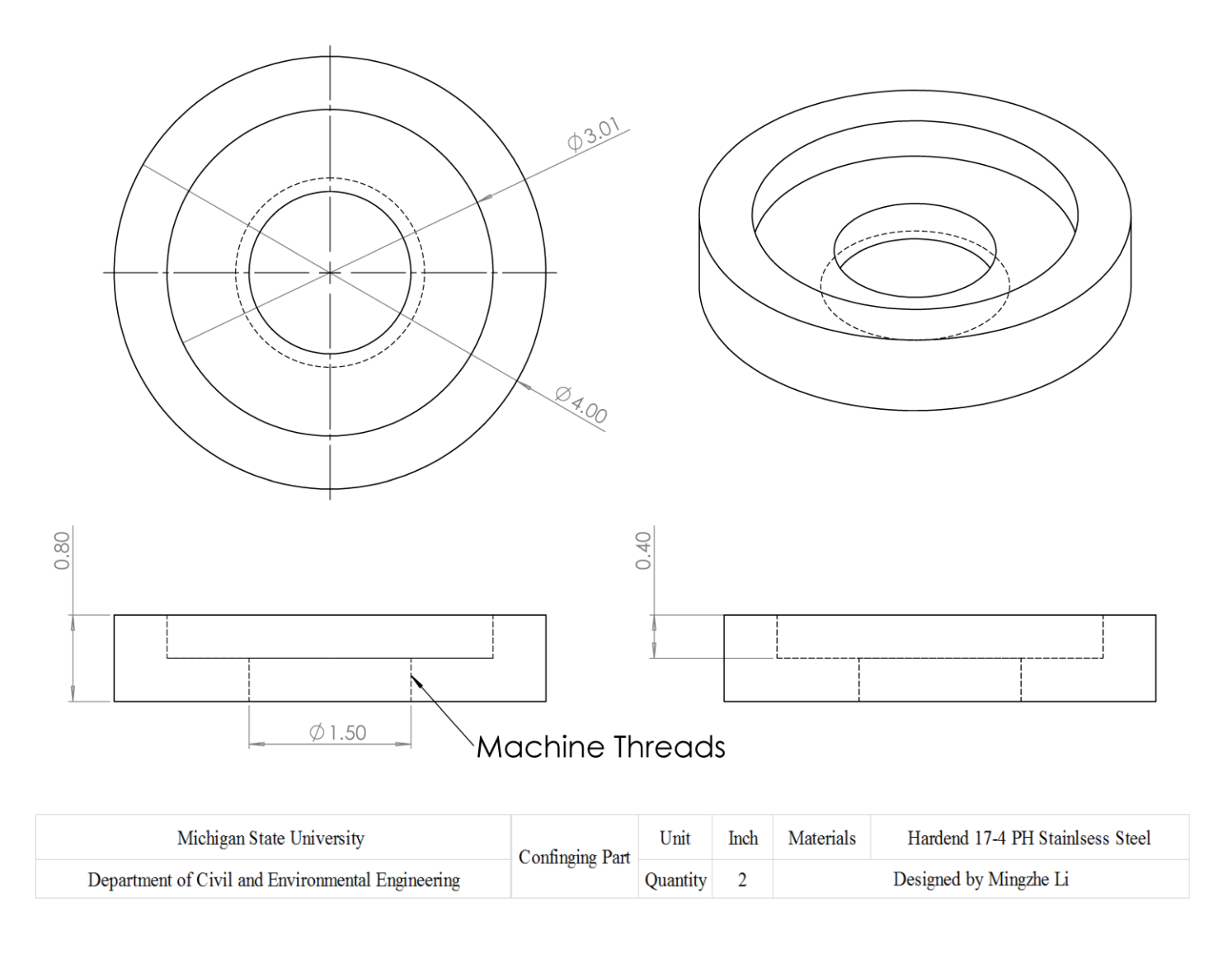


Figure A-6: Cap for large-scale tube – confining part.

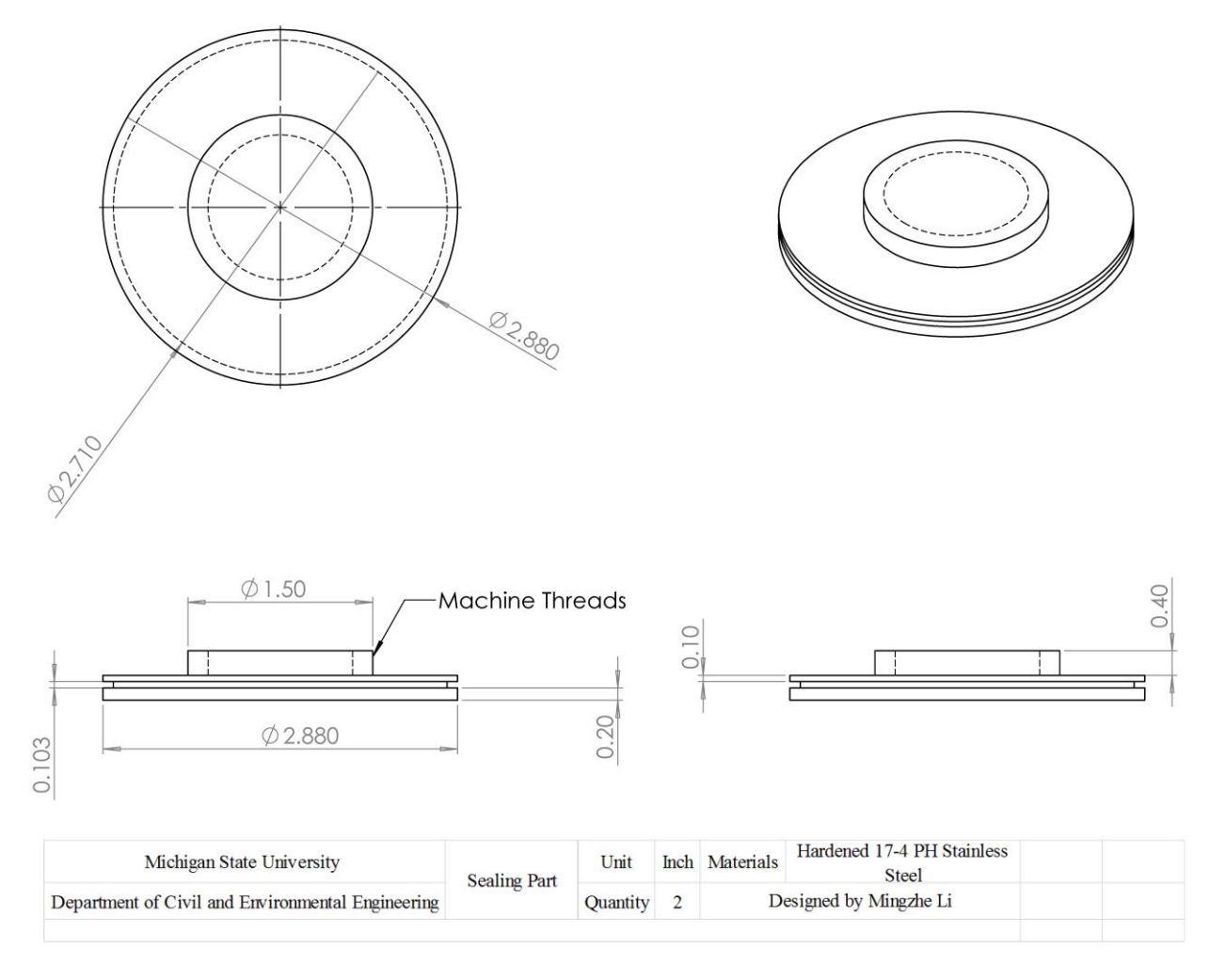


Figure A-7: Cap for large-scale tube – sealing part.

BIBLIOGRAPHY

BIBLIOGRAPHY

- [1] Dept of Transportation (US) National Highway Traffic Safety Administration (NHTSA) Center for Statistics, 2016, TRAFFIC SAFETY FACTS 2016 A Compilation of Motor Vehicle Crash Data from the Fatality Analysis Reporting System and the General Estimates System.
- [2] Dept of Transportation (US) National Highway Traffic Safety Administration (NHTSA), 2017, AUTOMATED DRIVING SYSTEMS 2.0: A VISION FOR SAFETY INTRODUCTORY MESSAGE.
- [3] Ajdari, A., Nayeb-Hashemi, H., and Vaziri, A., 2011, "Dynamic Crushing and Energy Absorption of Regular, Irregular and Functionally Graded Cellular Structures," *International Journal of Solids and Structures*, **48**(3–4), pp. 506–516.
- [4] Cui, L., Kiernan, S., and Gilchrist, M. D., 2009, "Designing the Energy Absorption Capacity of Functionally Graded Foam Materials," *Materials Science and Engineering A*, **507**(1–2), pp. 215–225.
- [5] Sack, A., Heckel, M., Kollmer, J. E., Zimber, F., and Pöschel, T., 2013, "Energy Dissipation in Driven Granular Matter in the Absence of Gravity," *Physical Review Letters*, **111**(1), pp. 1–5.
- [6] Daraio, C., Nesterenko, V. F., Herbold, E. B., and Jin, S., 2006, "Energy Trapping and Shock Disintegration in a Composite Granular Medium.," *Physical review letters*, **96**(5), p. 058002.
- [7] Evans, A. G., He, M. Y., Deshpande, V. S., Hutchinson, J. W., Jacobsen, A. J., and Carter, W. B., 2010, "Concepts for Enhanced Energy Absorption Using Hollow Micro-Lattices," *International Journal of Impact Engineering*, **37**(9), pp. 947–959.
- [8] Schaedler, T. A., Ro, C. J., Sorensen, A. E., Eckel, Z., Yang, S. S., Carter, W. B., and Jacobsen, A. J., 2014, "Designing Metallic Microlattices for Energy Absorber Applications," *Advanced Engineering Materials*, **16**(3), pp. 276–283.
- [9] Kostopoulos, V., Baltopoulos, A., Karapappas, P., Vavouliotis, A., and Paipetis, A., 2010, "Impact and After-Impact Properties of Carbon Fibre Reinforced Composites Enhanced with Multi-Wall Carbon Nanotubes," *Composites Science and Technology*, **70**(4), pp. 553–563.
- [10] Yan, L., and Chouw, N., 2013, "Crashworthiness Characteristics of Flax Fibre Reinforced Epoxy Tubes for Energy Absorption Application," *Materials and Design*, **51**, pp. 629–640.
- [11] Park, C., and Nutt, S. R., 2001, "Anisotropy and Strain Localization in Steel Foam," *Materials Science and Engineering A*, **299**(1–2), pp. 68–74.
- [12] Shen, J., Lu, G., and Ruan, D., 2010, "Compressive Behaviour of Closed-Cell Aluminium

- Foams at High Strain Rates," Composites Part B: Engineering, 41(8), pp. 678–685.
- [13] Zaiser, M., Mill, F., Konstantinidis, A., and Aifantis, K. E., 2013, "Strain Localization and Strain Propagation in Collapsible Solid Foams," *Materials Science and Engineering A*, **567**, pp. 38–45.
- [14] Wierzbicki, T., and Abramowicz, W., 1983, "On the Crushing Mechanics of Thin-Walled Structures," *Journal of Applied Mechanics*, **50**(4a), p. 727.
- [15] Chen, W., and Wierzbicki, T., 2001, "Relative Merits of Single-Cell, Multi-Cell and Foam-Filled Thin-Walled Structures in Energy Absorption," *Thin-Walled Structures*, **39**(4), pp. 287–306.
- [16] Baroutaji, A., Sajjia, M., and Olabi, A. G., 2017, "On the Crashworthiness Performance of Thin-Walled Energy Absorbers: Recent Advances and Future Developments," *Thin-Walled Structures*, **118**(May), pp. 137–163.
- [17] Marsolek, J., and Reimerdes, H. G., 2004, "Energy Absorption of Metallic Cylindrical Shells with Induced Non-Axisymmetric Folding Patterns," *International Journal of Impact Engineering*, **30**(8–9), pp. 1209–1223.
- [18] Bisagni, C., 2002, "Crashworthiness of Helicopter Subfloor Structures," *International Journal of Impact Engineering*, **27**(10), pp. 1067–1082.
- [19] Guillow, S. R., Lu, G., and Grzebieta, R. H., 2001, "Quasi-Static Axial Compression of Thin-Walled Circular Aluminium Tubes," *International Journal of Mechanical Sciences*, **43**(9), pp. 2103–2123.
- [20] Gupta, N. K., Sekhon, G. S., and Gupta, P. K., 2005, "Study of Lateral Compression of Round Metallic Tubes," *Thin-Walled Structures*, **43**(6), pp. 895–922.
- [21] Jing, Y. Y., and Barton, D. C., 1998, "The Response of Square Cross-Section Tubes under Lateral Impact Loading," *International Journal of Crashworthiness*, **3**(4), pp. 359–378.
- [22] Yu, X. H., Qiu, X. M., and Yu, T. X., 2015, "Analysis of the Free External Inversion of Circular Tubes Based on Deformation Theory," *International Journal of Mechanical Sciences*, **100**, pp. 262–268.
- [23] Yi Jin, S., Altenhof, W., and Kapoor, T., 2006, "An Experimental Investigation into the Cutting Deformation Mode of AA6061-T6 Round Extrusions," *Thin-Walled Structures*, 44(7), pp. 773–786.
- [24] Zarei, H. R., and Kröger, M., 2008, "Optimization of the Foam-Filled Aluminum Tubes for Crush Box Application," *Thin-Walled Structures*, **46**(2), pp. 214–221.
- [25] Toksoy, A. K., Tanoglu, M., Guden, M., and Hall, I. W., 2004, "Effect of Adhesive on the Strengthening of Aluminum Foam-Filled Circular Tubes," *Journal of Materials Science*, **39**(4), pp. 1503–1506.

- [26] Bonaccorsi, L., Proverbio, E., and Raffaele, N., 2010, "Effect of the Interface Bonding on the Mechanical Response of Aluminium Foam Reinforced Steel Tubes," *Journal of Materials Science*, **45**(6), pp. 1514–1522.
- [27] Hangai, Y., Saito, M., Utsunomiya, T., Kitahara, S., Kuwazuru, O., and Yoshikawa, N., 2014, "Fabrication of Aluminum Foam-Filled Thin-Wall Steel Tube by Friction Welding and Its Compression Properties," *Materials*, **6**(9), pp. 6796–6810.
- [28] Taherishargh, M., Vesenjak, M., Belova, I. V., Krstulović-Opara, L., Murch, G. E., and Fiedler, T., 2016, "In Situ Manufacturing and Mechanical Properties of Syntactic Foam Filled Tubes," *Materials and Design*, **99**, pp. 356–368.
- [29] Rajendran, R., Prem Sai, K., Chandrasekar, B., Gokhale, A., and Basu, S., 2009, "Impact Energy Absorption of Aluminium Foam Fitted AISI 304L Stainless Steel Tube," *Materials and Design*, **30**(5), pp. 1777–1784.
- [30] Hanssen, A. G., Langseth, M., and Hopperstad, O. S., 2000, "Static and Dynamic Crushing of Circular Aluminium Extrusions with Aluminium Foam Filler," *International Journal of Impact Engineering*, **24**(5), pp. 475–507.
- [31] Wang, Z., Liu, J., and Yao, S., 2018, "On Folding Mechanics of Multi-Cell Thin-Walled Square Tubes," *Composites Part B: Engineering*, **132**, pp. 17–27.
- [32] Seitzberger, M., Rammerstorfer, F. G., Gradinger, R., Degischer, H. P., Blaimschein, M., and Walch, C., 2000, "Experimental Studies on the Quasi-Static Axial Crushing of Steel Columns Filled with Aluminium Foam," *International Journal of Solids and Structures*, **37**, pp. 4125–4147.
- [33] Ahmad, Z., and Thambiratnam, D. P., 2009, "Crushing Response of Foam-Filled Conical Tubes under Quasi-Static Axial Loading," *Materials and Design*, **30**(7), pp. 2393–2403.
- [34] Wang, X., Shen, J., Zuo, Z. H., Huang, X., Zhou, S., and Xie, Y. M., 2015, "Numerical Investigation of Compressive Behaviour of Luffa-Filled Tubes," *Composites Part B: Engineering*, **73**, pp. 149–157.
- [35] Zhang, Y., Sun, G., Li, G., Luo, Z., and Li, Q., 2012, "Optimization of Foam-Filled Bitubal Structures for Crashworthiness Criteria," *Materials and Design*, **38**, pp. 99–109.
- [36] Abramowicz, W., 2003, "Thin-Walled Structures as Impact Energy Absorbers," *Thin-Walled Structures*, **41**(2–3), pp. 91–107.
- [37] Arwade, S. R., Schafer, B. W., Hajjar, J. F., Szyniszewski, S., and Smith, B. H., 2011, "Steel Foam for Structures: A Review of Applications, Manufacturing and Material Properties," *Journal of Constructional Steel Research*, 71, pp. 1–10.
- [38] Yao, Y., Wu, H., and Liu, Z., 2017, "Direct Simulation of Interstitial Heat Transfer Coefficient Between Paraffin and High Porosity Open-Cell Metal Foam," *Journal of Heat Transfer*, **140**(3), p. 032601.

- [39] Quell, A., Elsing, J., Drenckhan, W., and Stubenrauch, C., 2015, "Monodisperse Polystyrene Foams via Microfluidics A Novel Templating Route," *Advanced Engineering Materials*, **17**(5), pp. 604–609.
- [40] Ashby, M. F., 2006, "The Properties of Foams and Lattices," *Philosophical Transactions of the Royal Society A: Mathematical, Physical and Engineering Sciences*, **364**(1838), pp. 15–30.
- [41] Zarei, H., and Kröger, M., 2008, "Optimum Honeycomb Filled Crash Absorber Design," *Materials and Design*, **29**(1), pp. 193–204.
- [42] Daraio, C., Nesterenko, V. F., and Jin, S., 2004, "Highly Nonlinear Contact Interaction and Dynamic Energy Dissipation by Forest of Carbon Nanotubes," *Applied Physics Letters*, **85**(23), pp. 5724–5726.
- [43] Salari-Sharif, L., Valdevit, L., and Schaedler, T. A., 2014, "Energy Dissipation Mechanisms in Hollow Metallic Microlattices," *Journal of Materials Research*, **29**(16), pp. 1755–1770.
- [44] Schaedler, T. A., Jacobsen, A. J., Torrents, A., Sorensen, A. E., Lian, J., Greer, J. R., Valdevit, L., and Carter, W. B., 2011, "Ultralight Metallic Microlattices," *Science*, 334(6058), pp. 962–965.
- [45] Zhang, J., Supernak, P., Mueller-Alander, S., and Wang, C. H., 2013, "Improving the Bending Strength and Energy Absorption of Corrugated Sandwich Composite Structure," *Materials and Design*, **52**, pp. 767–773.
- [46] Koratkar, N. A., Suhr, J., Joshi, A., Kane, R. S., Schadler, L. S., Ajayan, P. M., and Bartolucci, S., 2005, "Characterizing Energy Dissipation in Single-Walled Carbon Nanotube Polycarbonate Composites," *Applied Physics Letters*, **87**(6), p. 063102.
- [47] Zinoviev, P. A., and Ermakov, Y. N., 2019, *Energy Dissipation in Composite Materials*, Routledge.
- [48] Sack, A., Heckel, M., Kollmer, J. E., Zimber, F., and Pöschel, T., 2013, "Energy Dissipation in Driven Granular Matter in the Absence of Gravity," *Physical Review Letters*, **111**(1), p. 018001.
- [49] Zhao, Z., Liu, C., and Brogliato, B., 2008, "Energy Dissipation and Dispersion Effects in Granular Media," *Physical Review E Statistical, Nonlinear, and Soft Matter Physics*, **78**(3), p. 031307.
- [50] Lee, Y. S., Wetzel, E. D., and Wagner, N. J., 2003, "The Ballistic Impact Characteristics of Kevlar® Woven Fabrics Impregnated with a Colloidal Shear Thickening Fluid," *Journal of Materials Science*, 38(13), pp. 2825–2833.
- [51] Lu, W., Kim, T., Zhao, C., Chen, X., and Qiao, Y., 2013, "Modified Infiltration of Solvated Ions and Ionic Liquid in a Nanoporous Carbon," *Applied Physics A: Materials Science and Processing*, **112**(4), pp. 885–889.

- [52] Sun, Y., Guo, Z., Xu, J., Xu, X., Liu, C., and Li, Y., 2015, "A Candidate of Mechanical Energy Mitigation System: Dynamic and Quasi-Static Behaviors and Mechanisms of Zeolite β/Water System," *Materials and Design*, **66**(PB), pp. 545–551.
- [53] Sun, Y., Lu, W., and Li, Y., 2014, "A Defiltration Control Method of Pressurized Liquid in Zeolite ZSM-5 by Silanol Introduction," *Applied Physics Letters*, **105**(12), p. 121609.
- [54] Hu, D., Jiang, H., Meng, K., Xu, J., and Lu, W., 2016, "The Impact Mitigation of a Heterojunction Nanotube-Water System: Behavior and Mechanism.," *Physical chemistry chemical physics: PCCP*, **18**(10), pp. 7395–403.
- [55] Lu, W., Punyamurtula, V. K., and Qiao, Y., 2011, "An Energy Absorption System Based on Carbon Nanotubes and Non-Aqueous Liquid," *International Journal of Materials Research*, **102**(5), pp. 587–590.
- [56] Lu, W., Han, A., Kim, T., Chow, B. J., and Qiao, Y., 2012, "Endcapping Treatment of Inner Surfaces of a Hexagonal Mesoporous Silica," *Journal of Adhesion Science and Technology*, **26**(12–17), pp. 2135–2141.
- [57] Li, M., Xu, L., and Lu, W., 2019, "Nanopore Size Effect on Critical Infiltration Depth of Liquid Nanofoam as a Reusable Energy Absorber," *Journal of Applied Physics*, **125**(4), p. 044303.
- [58] Daggumati, P., Matharu, Z., Wang, L., and Seker, E., 2015, "Biofouling-Resilient Nanoporous Gold Electrodes for DNA Sensing," *Analytical Chemistry*, **87**(17), pp. 8618–8622.
- [59] Saleh, O. A., and Sohn, L. L., 2003, "An Artificial Nanopore for Molecular Sensing," *Nano Letters*, **3**(1), pp. 37–38.
- [60] Vlassiouk, I., Takmakov, P., and Smirnov, S., 2005, "Sensing DNA Hybridization via Ionic Conductance through a Nanoporous Electrode," *Langmuir*, **21**(11), pp. 4776–4778.
- [61] Zhang, J., and Li, C. M., 2012, "Nanoporous Metals: Fabrication Strategies and Advanced Electrochemical Applications in Catalysis, Sensing and Energy Systems," *Chemical Society Reviews*, **41**(21), pp. 7016–7031.
- [62] Santos, A., Kumeria, T., and Losic, D., 2013, "Nanoporous Anodic Aluminum Oxide for Chemical Sensing and Biosensors," *TrAC Trends in Analytical Chemistry*, **44**, pp. 25–38.
- [63] Holt, J. K., Park, H. G., Wang, Y., Stadermann, M., Artyukhin, A. B., Grigoropoulos, C. P., Noy, A., and Bakajin, O., 2006, "Fast Mass Transport through Sub-2-Nanometer Carbon Nanotubes.," *Science (New York, N.Y.)*, **312**(5776), pp. 1034–7.
- [64] Stadermann, M., Park, H. G., Noy, A., Holt, J. K., Grigoropoulos, C. P., Fornasiero, F., and Bakajin, O., 2008, "Ion Exclusion by Sub-2-Nm Carbon Nanotube Pores," *Proceedings of the National Academy of Sciences*, **105**(45), pp. 17250–17255.

- [65] Majumder, M., Chopra, N., and Hinds, B. J., 2011, "Mass Transport through Carbon Nanotube Membranes in Three Different Regimes: Ionic Diffusion and Gas and Liquid Flow," *ACS Nano*, 5(5), pp. 3867–3877.
- [66] Jiang, L., Shi, Z., Liu, X., Zhang, W., Wang, D., Zhang, F., and Jin, J., 2013, "Ultrafast Separation of Emulsified Oil/Water Mixtures by Ultrathin Free-Standing Single-Walled Carbon Nanotube Network Films," *Advanced Materials*, **25**(17), pp. 2422–2427.
- [67] Nur, H., Manan, A. F. N. A., Wei, L. K., Muhid, M. N. M., and Hamdan, H., 2005, "Simultaneous Adsorption of a Mixture of Paraquat and Dye by NaY Zeolite Covered with Alkylsilane," *Journal of Hazardous Materials*, **117**(1), pp. 35–40.
- [68] Wang, L., and Xiao, F. S., 2015, "Nanoporous Catalysts for Biomass Conversion," *Green Chemistry*, **17**(1), pp. 24–39.
- [69] Ravikovitch, P. I., Haller, G. L., and Neimark, A. V., 1998, "Density Functional Theory Model for Calculating Pore Size Distributions: Pore Structure of Nanoporous Catalysts," *Advances in Colloid and Interface Science*, **76–77**, pp. 203–226.
- [70] Forster, P. M., and Cheetham, A. K., 2003, "Hybrid Inorganic–Organic Solids: An Emerging Class of Nanoporous Catalysts," *Topics in Catalysis*, **24**(1–4), pp. 79–86.
- [71] Vajtai, R., He, Y., Liu, Z., Lei, S., Zhang, X., Zhou, W., Ye, G., Gong, Y., Lou, J., Wang, Q., Keyshar, K., Li, B., and Ajayan, P. M., 2015, "Two-Step Growth of Two-Dimensional WSe2/MoSe2 Heterostructures," *Nano Letters*, **15**(9), pp. 6135–6141.
- [72] Wen, S., Mho, S. il, and Yeo, I. H., 2006, "Improved Electrochemical Capacitive Characteristics of the Carbon Nanotubes Grown on the Alumina Templates with High Pore Density," *Journal of Power Sources*, **163**(1 SPEC. ISS.), pp. 304–308.
- [73] Dunkel, C., Etienne, M., Oekermann, T., Smarsly, B. M., Boissière, C., Sallard, S., Wark, M., Schröder, M., and Walcarius, A., 2013, "Bimodal Mesoporous Titanium Dioxide Anatase Films Templated by a Block Polymer and an Ionic Liquid: Influence of the Porosity on the Permeability," *Nanoscale*, **5**(24), p. 12316.
- [74] Polarz, S., and Smarsly, B., 2002, "Nanoporous Materials," *Journal of Nanoscience and Nanotechnology*, **2**(6), pp. 581–612.
- [75] Lu, A. H., and Schüth, F., 2006, "Nanocasting: A Versatile Strategy for Creating Nanostructured Porous Materials," *Advanced Materials*, **18**(14), pp. 1793–1805.
- [76] Fadeev, A., and Eroshenko, V., 1997, "Study of Penetration of Water into Hydrophobized Porous Silicas," *Journal of colloid and interface science*, **187**(2), pp. 275–82.
- [77] Fadeev, A. Y., and Staroverov, S. M., 1988, "Geometric Structural Properties of Bonded Layers of Chemically Modified Silicas," *Journal of Chromatography A*, **447**, pp. 103–116.
- [78] Qiao, Y., Liu, L., and Chen, X., 2009, "Pressurized Liquid in Nanopores: A Modified

- Laplace-Young Equation," Nano Letters, 9(3), pp. 984–988.
- [79] Kim, T., Lu, W., Lim, H., Han, A., and Qiao, Y., 2011, "Electrically Controlled Hydrophobicity in a Surface Modified Nanoporous Carbon," *Applied Physics Letters*, **98**(5), pp. 25–28.
- [80] Chen, X., Cao, G., Han, A., Punyamurtula, V. K., Liu, L., Culligan, P. J., Kim, T., and Qiao, Y., 2008, "Nanoscale Fluid Transport: Size and Rate Effects," *Nano Letters*, **8**(9), pp. 2988–2992.
- [81] Han, A., Kong, X., and Qiao, Y., 2006, "Pressure Induced Liquid Infiltration in Nanopores," *Journal of Applied Physics*, **100**(1), p. 014308.
- [82] Han, A., Lu, W., Punyamurtula, V. K., Chen, X., Surani, F. B., Kim, T., and Qiao, Y., 2008, "Effective Viscosity of Glycerin in a Nanoporous Silica Gel," *Journal of Applied Physics*, **104**(12).
- [83] Han, A., Lu, W., Kim, T., Chen, X., and Qiao, Y., 2008, "Influence of Anions on Liquid Infiltration and Defiltration in a Zeolite Y," *Physical Review E Statistical, Nonlinear, and Soft Matter Physics*, **78**(3), pp. 3–6.
- [84] Han, A., Chen, X., and Qiao, Y., 2008, "Effects of the Addition of Electrolyte on Liquid Infiltration in a Hydrophobic Nanoporous Silica Gel," *Langmuir*, **24**(14), pp. 7044–7047.
- [85] Surani, F. B., and Qiao, Y., 2006, "Infiltration and Defiltration of an Electrolyte Solution in Nanopores," *Journal of Applied Physics*, **100**(3), pp. 1–5.
- [86] Kong, X., and Qiao, Y., 2005, "Thermal Effects on Pressure-Induced Infiltration of a Nanoporous System," *Philosophical Magazine Letters*, **85**(7), pp. 331–337.
- [87] Han, A., and Qiao, Y., 2007, "Effects of Surface Treatment of MCM-41 on Motions of Confined Liquids," *Journal of Physics D: Applied Physics*, **40**(18), pp. 5743–5746.
- [88] Cao, G., 2012, "Working Mechanism of Nanoporous Energy Absorption System under High Speed Loading," *Journal of Physical Chemistry C*, **116**(14), pp. 8278–8286.
- [89] Ramesh, K. T., 2008, "High Rates and Impact Experiments," *Springer Handbook of Experimental Solid Mechanics*, Springer US, Boston, MA, pp. 929–960.
- [90] Zukas, J. A., 2004, "Chapter 1 Dynamic Behavior of Materials and Structures," *Studies in Applied Mechanics*, **49**(C), pp. 1–31.
- [91] Soliman, E. M., Sheyka, M. P., and Taha, M. R., 2012, "Low-Velocity Impact of Thin Woven Carbon Fabric Composites Incorporating Multi-Walled Carbon Nanotubes," *International Journal of Impact Engineering*, **47**, pp. 39–47.
- [92] Song, B., and Chen, W., 2004, "Dynamic Stress Equilibration in Split Hopkinson Pressure Bar Tests on Soft Materials," *Experimental Mechanics*, **44**(3), pp. 300–312.

- [93] Hou, J. P., Petrinic, N., Ruiz, C., and Hallett, S. R., 2000, "Prediction of Impact Damage in Composite Plates," *Composites Science and Technology*, **60**(2), pp. 273–281.
- [94] Kryscio, R. J., Hisel, R. D., Geddes, J. W., Lusk, B. T., Reneer, D. V., and Hoffman, J. M., 2010, "A Multi-Mode Shock Tube for Investigation of Blast-Induced Traumatic Brain Injury," *Journal of Neurotrauma*, **28**(1), pp. 95–104.
- [95] Schwaiger, R., Moser, B., Dao, M., Chollacoop, N., and Suresh, S., 2003, "Some Critical Experiments on the Strain-Rate Sensitivity of Nanocrystalline Nickel," *Acta Materialia*, **51**(17), pp. 5159–5172.
- [96] Kim, H. G., Li, J., Samanta, A., Suresh, S., and Zhu, T., 2007, "Interfacial Plasticity Governs Strain Rate Sensitivity and Ductility in Nanostructured Metals," *Proceedings of the National Academy of Sciences*, **104**(9), pp. 3031–3036.
- [97] Dao, M., Lu, L., Shen, Y. F., and Suresh, S., 2006, "Strength, Strain-Rate Sensitivity and Ductility of Copper with Nanoscale Twins," *Acta Materialia*, **54**(20), pp. 5421–5432.
- [98] Canadinc, D., Efstathiou, C., and Sehitoglu, H., 2008, "On the Negative Strain Rate Sensitivity of Hadfield Steel," *Scripta Materialia*, **59**(10), pp. 1103–1106.
- [99] Li, Z., and Lambros, J., 2001, "Strain Rate Effects on the Thermomechanical Behavior of Polymers," *International Journal of Solids and Structures*, **38**(20), pp. 3549–3562.
- [100] Sarva, S. S., Deschanel, S., Boyce, M. C., and Chen, W., 2007, "Stress-Strain Behavior of a Polyurea and a Polyurethane from Low to High Strain Rates," *Polymer*, **48**(8), pp. 2208–2213.
- [101] Siviour, C. R., and Jordan, J. L., 2016, "High Strain Rate Mechanics of Polymers: A Review," *Journal of Dynamic Behavior of Materials*, **2**(1), pp. 15–32.
- [102] Paul, A., and Ramamurty, U., 2000, "Strain Rate Sensitivity of a Closed-Cell Aluminum Foam," *Materials Science and Engineering A*, **281**(1–2), pp. 1–7.
- [103] Ouellet, S., Cronin, D., and Worswick, M., 2006, "Compressive Response of Polymeric Foams under Quasi-Static, Medium and High Strain Rate Conditions," *Polymer Testing*, **25**(6), pp. 731–743.
- [104] Higashi, K., Mukai, T., Miyoshi, T., Somekawa, H., and Nakano, S., 2005, "Compressive Response of a Closed-Cell Aluminum Foam at High Strain Rate," *Scripta Materialia*, **54**(4), pp. 533–537.
- [105] Vesenjak, M., Veyhl, C., and Fiedler, T., 2012, "Analysis of Anisotropy and Strain Rate Sensitivity of Open-Cell Metal Foam," *Materials Science and Engineering A*, **541**, pp. 105–109.
- [106] Shen, J., Lu, G., and Ruan, D., 2010, "Compressive Behaviour of Closed-Cell Aluminium Foams at High Strain Rates," *Composites Part B: Engineering*, **41**(8), pp. 678–685.

- [107] Cantwell, W. J., and Morton, J., 1991, "The Impact Resistance of Composite Materials a Review," *Composites*, **22**(5), pp. 347–362.
- [108] Hangai, Y., Kubota, N., Utsunomiya, T., Kawashima, H., Kuwazuru, O., and Yoshikawa, N., 2015, "Drop Weight Impact Behavior of Functionally Graded Aluminum Foam Consisting of A1050 and A6061 Aluminum Alloys," *Materials Science and Engineering A*, **639**, pp. 597–603.
- [109] Lu, W., Kim, T., Punyamurtula, V. K., Han, A., and Qiao, Y., 2011, "Effects of Addition of Potassium Chloride and Ethylene Glycol on Nanofluidic Behaviors," *Journal of Materials Science*, **46**(11), pp. 4053–4057.
- [110] Qiao, Y., Zhongyuan, S., Lu, W., and Han, A., 2010, "Temperature Variation in Energy Absorption System Functionalized by Nanomaterials," *MRS Proceedings*, **1242**, pp. 1–7.
- [111] Lim, H., Lu, W., Chen, X., and Qiao, Y., 2012, "Anion Size Effect on Electrode Potential in a Nanoporous Carbon," *International Journal of ELECTROCHEMICAL SCIENCE*, **7**, pp. 2577–2583.
- [112] Lim, H., Lu, W., Chen, X., and Qiao, Y., 2013, "Effects of Ion Concentration on Thermally-Chargeable Double-Layer Supercapacitors.," *Nanotechnology*, **24**, p. 465401.
- [113] Lu, W., Han, A., Kim, T., Punyamurtula, V. K., Chen, X., and Qiao, Y., 2009, "Field-Responsive Ion Transport in Nanopores," *Applied Physics Letters*, **94**(2), pp. 2007–2010.
- [114] Lu, W., Punyamurtula, V. K., and Qiao, Y., 2011, "An Energy Absorption System Based on Carbon Nanotubes and Non-Aqueous Liquid," *International Journal of Materials Research*, **102**(5), pp. 587–590.
- [115] Lu, W., Han, A., Kim, T., and Qiao, Y., 2009, "Effect of 16-Mercaptohexadecanoic Acid Modification on Liquid Transport in a Nanoporous Carbon," *Applied Physics Letters*, **94**(22), pp. 33–36.
- [116] Han, A., Lu, W., Kim, T., Punyamurtula, V. K., and Qiao, Y., 2009, "The Dependence of Infiltration Pressure and Volume in Zeolite Y on Potassium Chloride Concentration," *Smart Materials and Structures*, **18**, pp. 1–5.
- [117] Lu, W., Chakravarthula, S. S., Chen, J., and Qiao, Y., 2012, "Propagation of a Cleavage Crack Front across a Field of Persistent Grain Boundaries," *International Journal of Solids and Structures*, **49**(3–4), pp. 584–589.
- [118] Lu, W., Kim, T., Han, A., and Qiao, Y., 2012, "Electrically Controlling Infiltration Pressure in Nanopores of a Hexagonal Mesoporous Silica," *Materials Chemistry and Physics*, **133**(1), pp. 259–262.
- [119] Lu, W., Kim, T., Han, A., Chen, X., and Qiao, Y., 2009, "Eletrowetting Effect in a Nanoporous Silica," *Langmuir*, **25**(16), pp. 9463–9466.

- [120] Surani, F. B., Kong, X., Panchal, D. B., and Qiao, Y., 2005, "Energy Absorption of a Nanoporous System Subjected to Dynamic Loadings," *Applied Physics Letters*, **87**(16), pp. 1–3.
- [121] Zhang, Y., Li, M., Gao, Y., Xu, B., and Lu, W., 2018, "Compressing Liquid Nanofoam Systems: Liquid Infiltration or Nanopore Deformation?," *Nanoscale*, **10**(39), pp. 18444–18450.
- [122] Zhao, J., Culligan, P. J., Germaine, J. T., and Chen, X., 2009, "Experimental Study on Energy Dissipation of Electrolytes in Nanopores," *Langmuir*, **25**(21), pp. 12687–12696.
- [123] Zhao, H., Elnasri, I., and Li, H. J., 2006, "The Mechanism of Strength Enhancement under Impact Loading of Cellular Materials," *Advanced Engineering Materials*, **8**(9), pp. 877–883.
- [124] Majumder, M., Chopra, N., Andrews, R., and Hinds, B. J., 2005, "Nanoscale Hydrodynamics: Enhanced Flow in Carbon Nanotubes," *Nature*, **438**(7064), pp. 44–44.
- [125] Holt, J. K., Park, H. G., Wang, Y., Stadermann, M., Artyukhin, A. B., Grigoropoulos, C. P., Noy, A., and Bakajin, O., 2006, "Fast Mass Transport Through Sub–2-Nanometer Carbon Nanotubes," *Science*, **312**(May), pp. 1034–1037.
- [126] Li, M., and Lu, W., 2017, "Adaptive Liquid Flow Behavior in 3D Nanopores," *Physical Chemistry Chemical Physics*, **19**(26), pp. 17167–17172.
- [127] Borman, V. D., Belogorlov, A. A., Grekhov, A. M., and Tronin, V. N., 2014, "Fluctuations of the Number of Neighboring Pores and Appearance of Multiple Nonergodic States of a Nonwetting Liquid Confined in a Disordered Nanoporous Medium," *Physics Letters A*, **378**(38–39), pp. 2888–2893.
- [128] Wang, P., Xu, S., Li, Z., Yang, J., Zhang, C., Zheng, H., and Hu, S., 2014, "Experimental Investigation on the Strain-Rate Effect and Inertia Effect of Closed-Cell Aluminum Foam Subjected to Dynamic Loading," *Materials Science and Engineering A*, **620**, pp. 253–261.
- [129] Tan, P. J., Harrigan, J. J., and Reid, S. R., 2002, "Inertia Effects in Uniaxial Dynamic Compression of a Closed Cell Aluminium Alloy Foam," *Materials Science and Technology*, **18**(5), pp. 480–488.
- [130] Wang, Z. P., and Sun, C. T., 2002, "Modeling Micro-Inertia in Heterogeneous Materials under Dynamic Loading," *Wave Motion*, **36**(4), pp. 473–485.
- [131] Scatena, L. F., Brown, M. G., and Richmond, G. L., 2001, "Water at Hydrophobic Surfaces: Weak Hydrogen Bonding and Strong Orientation Effects," *Science*, **292**(5518), pp. 908–912.
- [132] Hummer, G., Rasaiah, J. C., and Noworyta, J. P., 2001, "Water Conduction through the Hydrophobic Channel of a Carbon Nanotube.," *Nature*, **414**(6860), pp. 188–190.

- [133] Joseph, S., and Aluru, N. R., 2008, "Why Are Carbon Nanotubes Fast Transporters of Water?," *Nano Letters*, **8**(2), pp. 452–458.
- [134] Poynor, A., Hong, L., Robinson, I. K., Granick, S., Zhang, Z., and Fenter, P. A., 2006, "How Water Meets a Hydrophobic Surface," *Physical Review Letters*, **97**(26), p. 266101.
- [135] Bianco, A., Kostarelos, K., and Prato, M., 2005, "Applications of Carbon Nanotubes in Drug Delivery," *Current Opinion in Chemical Biology*, **9**(6), pp. 674–679.
- [136] Eroshenko, V., Regis, R. C., Soulard, M., and Patarin, J., 2001, "Energetics: A New Field of Application for Hydrophobic Zeolites," *J. Am. Chem. Soc.*, **33**(123), pp. 8129–8130.
- [137] Xu, B., Chen, X., Lu, W., Zhao, C., and Qiao, Y., 2014, "Non-Dissipative Energy Capture of Confined Liquid in Nanopores," *Applied Physics Letters*, **104**(20), p. 203107.
- [138] Wheeler, T. D., and Stroock, A. D., 2008, "The Transpiration of Water at Negative Pressures in a Synthetic Tree.," *Nature*, **455**(September), pp. 208–212.
- [139] Park, H. G., and Jung, Y., 2014, "Carbon Nanofluidics of Rapid Water Transport for Energy Applications.," *Chemical Society reviews*, **43**(2), pp. 565–76.
- [140] Wasan, D. T., and Nikolov, A. D., 2003, "Spreading of Nanofluids on Solids.," *Nature*, **423**(6936), pp. 156–159.
- [141] Li, Y., Xu, J., and Li, D., 2010, "Molecular Dynamics Simulation of Nanoscale Liquid Flows," *Microfluidics and Nanofluidics*, **9**(6), pp. 1011–1031.
- [142] Huang, H., Song, Z., Wei, N., Shi, L., Mao, Y., Ying, Y., Sun, L., Xu, Z., and Peng, X., 2013, "Ultrafast Viscous Water Flow through Nanostrand-Channelled Graphene Oxide Membranes.," *Nature communications*, **4**, p. 2979.
- [143] Sokhan, V. P., Nicholson, D., and Quirke, N., 2001, "Fluid Flow in Nanopores: An Examination of Hydrodynamic Boundary Conditions," *Journal of Chemical Physics*, **115**(8), pp. 3878–3887.
- [144] Lu, W., Punyamurtula, V. K., Han, A., Kim, T., and Qiao, Y., 2009, "A Thermally Sensitive Energy-Absorbing Composite Functionalized by Nanoporous Carbon," *Journal of Materials Research*, **24**(11), pp. 3308–3312.
- [145] Hu, D., Jiang, H., Meng, K., Xu, J., and Lu, W., 2016, "The Impact Mitigation of a Heterojunction Nanotube–water System: Behavior and Mechanism," *Phys. Chem. Chem. Phys.*, **18**(10), pp. 7395–7403.
- [146] Rigby, S. P., and Edler, K. J., 2002, "The Influence of Mercury Contact Angle, Surface Tension, and Retraction Mechanism on the Interpretation of Mercury Porosimetry Data.," *Journal of colloid and interface science*, **250**(1), pp. 175–190.
- [147] Lefevre, B., Saugey, A., Barrat, J. L., Bocquet, L., Charlaix, E., Gobin, P. F., and Vigier,

- G., 2004, "Intrusion and Extrusion of Water in Hydrophobic Mesopores," *Journal of Chemical Physics*, **120**(10), pp. 4927–4938.
- [148] Zhao, J., Culligan, P. J., Qiao, Y., Zhou, Q., Li, Y., Tak, M., Park, T., and Chen, X., 2010, "Electrolyte Solution Transport in Electropolar Nanotubes," *Journal of Physics: Condensed Matter*, **22**(31), p. 315301.
- [149] Xu, B., Wang, B., Park, T., Qiao, Y., Zhou, Q., and Chen, X., 2012, "Temperature Dependence of Fluid Transport in Nanopores," *Journal of Chemical Physics*, **136**(18), p. 184701.
- [150] Andreev, S., Reichman, D., and Hummer, G., 2005, "Effect of Flexibility on Hydrophobic Behavior of Nanotube Water Channels," *Journal of Chemical Physics*, **123**(19), p. 194502.
- [151] Xu, B., Li, Y., Park, T., and Chen, X., 2011, "Effect of Wall Roughness on Fluid Transport Resistance in Nanopores," *Journal of Chemical Physics*, **135**(14), p. 144703.
- [152] Zhao, J., Liu, L., Culligan, P. J., and Chen, X., 2009, "Thermal Effect on the Dynamic Infiltration of Water into Single-Walled Carbon Nanotubes," *Physical Review E Statistical, Nonlinear, and Soft Matter Physics*, **80**(6), p. 061206.
- [153] Mohiuddin Mala, G., and Li, D., 1999, "Flow Characteristics of Water in Microtubes," *International Journal of Heat and Fluid Flow*, **20**(2), pp. 142–148.
- [154] Cao, G., Qiao, Y., Zhou, Q., and Chen, X., 2008, "Water Infiltration Behaviours in Carbon Nanotubes under Quasi-Static and Dynamic Loading Conditions," *Molecular Simulation*, **34**(10), pp. 1267–1274.
- [155] Xu, B., Qiao, Y., and Chen, X., 2014, "Mitigating Impact/Blast Energy via a Novel Nanofluidic Energy Capture Mechanism," *Journal of the Mechanics and Physics of Solids*, **62**(1), pp. 194–208.
- [156] Li, M., and Lu, W., 2017, "Liquid Marble: A Novel Liquid Nanofoam Structure for Energy Absorption," *AIP Advances*, **7**(5), p. 055312.
- [157] Aussillous, P., and Quéré, D., 2001, "Liquid Marbles," *Nature*, **411**(6840), pp. 924–927.
- [158] McHale, G., and Newton, M. I., 2011, "Liquid Marbles: Principles and Applications," *Soft Matter*, **7**(12), p. 5473.
- [159] Binks, B. P., and Murakami, R., 2006, "Phase Inversion of Particle-Stabilized Materials from Foams to Dry Water.," *Nature materials*, **5**(11), pp. 865–869.
- [160] Aussillous, P., and Quéré, D., 2006, "Properties of Liquid Marbles," *Proceedings of the Royal Society A: Mathematical, Physical and Engineering Sciences*, **462**(2067), pp. 973–999.
- [161] Lu, W., Punyamurtula, V. K., Han, A., Kim, T., and Qiao, Y., 2011, "A Thermally Sensitive

- Energy-Absorbing Composite Functionalized by Nanoporous Carbon," *Journal of Materials Research*, **24**(11), pp. 3308–3312.
- [162] Yildirim, A., Budunoglu, H., Daglar, B., Deniz, H., and Bayindir, M., 2011, "One-Pot Preparation of Fluorinated Mesoporous Silica Nanoparticles for Liquid Marble Formation and Superhydrophobic Surfaces," *ACS Applied Materials and Interfaces*, **3**(6), pp. 1804–1808.
- [163] Han, A., Punyamurthula, V. K., Lu, W., and Qiao, Y., 2008, "Deformation of a Nanoporous Silica under Compressive Loading," *Journal of Applied Physics*, **103**(8), p. 084318.
- [164] Fish, J., Filonova, V., and Kuznetsov, S., 2012, "Micro-Inertia Effects in Nonlinear Heterogeneous Media," *International Journal for Numerical Methods in Engineering*, **91**(13), pp. 1406–1426.
- [165] Li, M., Li, J., Barbat, S., Baccouche, R., and Lu, W., 2018, "Enhanced Filler-Tube Wall Interaction in Liquid Nanofoam-Filled Thin-Walled Tubes," *Composite Structures*, **200**, pp. 120–126.
- [166] Brahmakumar, M., Pavithran, C., and Pillai, R. M., 2005, "Coconut Fibre Reinforced Polyethylene Composites: Effect of Natural Waxy Surface Layer of the Fibre on Fibre/Matrix Interfacial Bonding and Strength of Composites," *Composites Science and Technology*, **65**(3–4), pp. 563–569.
- [167] Jang, S., Chung, J., Seo, S., Lee, S., Lee, Y., Lee, S., and Choi, H. J., 2017, "Enhancement of Interfacial Adhesion Based on Nanostructured Alumina/Aluminum Laminates," *Composites Part B: Engineering*, **129**, pp. 204–209.
- [168] Cheng, Z., Kennedy, D., and Williams, W. F., 1996, "Effect of Interfacial Imperfection on Buckling and Bending Behavior of Composite Laminates," *AIAA Journal*, **34**(12), pp. 2590–2595.
- [169] Shi, S. S., Sun, Z., Hu, X. Z., and Chen, H. R., 2014, "Carbon-Fiber and Aluminum-Honeycomb Sandwich Composites with and without Kevlar-Fiber Interfacial Toughening," *Composites Part A: Applied Science and Manufacturing*, **67**, pp. 102–110.
- [170] Lin, S., Yuk, H., Zhang, T., Parada, G. A., Koo, H., Yu, C., and Zhao, X., 2016, "Stretchable Hydrogel Electronics and Devices," *Advanced Materials*, **28**(22), pp. 4497–4505.
- [171] Ku, H., Wang, H., Pattarachaiyakoop, N., and Trada, M., 2011, "A Review on the Tensile Properties of Natural Fiber Reinforced Polymer Composites," *Composites Part B: Engineering*, **42**(4), pp. 856–873.
- [172] Ruch, P. W., Beffort, O., Kleiner, S., Weber, L., and Uggowitzer, P. J., 2006, "Selective Interfacial Bonding in Al(Si)-Diamond Composites and Its Effect on Thermal Conductivity," *Composites Science and Technology*, **66**(15), pp. 2677–2685.
- [173] Lee, S. H., Cho, E., Jeon, S. H., and Youn, J. R., 2007, "Rheological and Electrical

- Properties of Polypropylene Composites Containing Functionalized Multi-Walled Carbon Nanotubes and Compatibilizers," *Carbon*, **45**(14), pp. 2810–2822.
- [174] Kaelble, D., Dynes, P., and Cirlin, E., 1974, "Interfacial Bonding and Environmental Stability of Polymer Matrix Composites," *The Journal of Adhesion*, **6**(September 2012), pp. 23–48.
- [175] Reid, S. R., and Reddy, T. Y., 1986, "Axial Crushing of Foam-Filled Tapered Sheet Metal Tubes," *International Journal of Mechanical Sciences*, **28**(10), pp. 643–656.
- [176] Guillow, S. R., Lu, G., and Grzebieta, R. H., 2001, "Quasi-Static Axial Compression of Thin-Walled Circular Aluminium Tubes," *International Journal of Mechanical Sciences*, **43**(9), pp. 2103–2123.
- [177] Santosa, S., and Wierzbicki, T., 1998, "Crash Behavior of Box Columns Filled with Aluminum Honeycomb or Foam," *Computers and Structures*, **68**(4), pp. 343–367.
- [178] Santosa, S. P., Wierzbicki, T., Hanssen, A. G., and Langseth, M., 2000, "Experimental and Numerical Studies of Foam-Filled Sections," *International Journal of Impact Engineering*, **24**(5), pp. 509–534.
- [179] Duarte, I., Vesenjak, M., Krstulović-Opara, L., and Ren, Z., 2015, "Compressive Performance Evaluation of APM (Advanced Pore Morphology) Foam Filled Tubes," *Composite Structures*, **134**, pp. 409–420.
- [180] Sun, Y. T., Xu, J., Li, Y. B., Xu, X. Q., Liu, C., and Chen, X., 2013, "Mechanism of Water Infiltration and Defiltration through ZSM-5 Zeolite: Heating and Sodium Chloride Concentration Effect," *Journal of Nanomaterials*, **2013**, p. 249369.
- [181] Liu, L., Lim, H., Lu, W., Qiao, Y., and Chen, X., 2013, "Mechanical-to-Electric Energy Conversion by Mechanically Driven Flow of Electrolytes Confined in Nanochannels," *Applied Physics Express*, **6**(1).
- [182] Han, A., Punyamurtula, V. K., Kim, T., and Qiao, Y., 2008, "The Upper Limit of Energy Density of Nanoporous Materials Functionalized Liquid," *Journal of Materials Engineering and Performance*, **17**(3), pp. 326–329.
- [183] Chen, X., Surani, F. B., Kong, X., Punyamurtula, V. K., and Qiao, Y., 2006, "Energy Absorption Performance of Steel Tubes Enhanced by a Nanoporous Material Functionalized Liquid," *Applied Physics Letters*, **89**(24), pp. 1–3.
- [184] Sun, Y., Xu, J., Zhao, C., Li, P., and Li, Y., 2014, "Exploring a New Candidate of Energy Absorber: Thin-Walled Tube Structures Filled with Nanoporous Material Functionalized Liquid," *IRCOBI Conference 2014*, pp. 578–586.
- [185] Sun, Y., Li, Y., Zhao, C., Wang, M., Lu, W., and Qiao, Y., 2016, "Crushing of Circular Steel Tubes Filled with Nanoporous-Materials-Functionalized Liquid," *International Journal of Damage Mechanics*, **0**(0), pp. 1–12.

- [186] Andrews, K. R. F., England, G. L., and Ghani, E., 1983, "Classification of the Axial Collapse of Cylindrical Tubes under Quasi-Static Loading," *International Journal of Mechanical Sciences*, **25**(9–10), pp. 687–696.
- [187] Kavi, H., Toksoy, A. K., and Guden, M., 2006, "Predicting Energy Absorption in a Foam-Filled Thin-Walled Aluminum Tube Based on Experimentally Determined Strengthening Coefficient," *Materials and Design*, **27**(4), pp. 263–269.
- [188] Liu, Q., Fu, J., Wang, J., Ma, J., Chen, H., Li, Q., and Hui, D., 2017, "Axial and Lateral Crushing Responses of Aluminum Honeycombs Filled with EPP Foam," *Composites Part B: Engineering*, **130**, pp. 236–247.
- [189] Duarte, I., Krstulović-Opara, L., and Vesenjak, M., 2015, "Characterisation of Aluminium Alloy Tubes Filled with Aluminium Alloy Integral-Skin Foam under Axial Compressive Loads," *Composite Structures*, **121**, pp. 154–162.
- [190] Abramowicz, W., and Jones, N., 1984, "Dynamic Axial Crushing of Circular Tubes," *International Journal of Impact Engineering*, **2**(3), pp. 263–281.
- [191] Liu, Y., Schaedler, T. A., Jacobsen, A. J., Lu, W., Qiao, Y., and Chen, X., 2014, "Quasi-Static Crush Behavior of Hollow Microtruss Filled with NMF Liquid," *Composite Structures*, **115**(1), pp. 29–40.
- [192] Liu, Y., Schaedler, T. A., Jacobsen, A. J., and Chen, X., 2014, "Quasi-Static Energy Absorption of Hollow Microlattice Structures," *Composites Part B: Engineering*, **67**, pp. 39–49.
- [193] Xu, B., Chen, X., Lu, W., Zhao, C., and Qiao, Y., 2014, "Non-Dissipative Energy Capture of Confined Liquid in Nanopores," *Applied Physics Letters*, **104**(20), pp. 2012–2016.
- [194] Lu, W., 2016, "Novel Protection Mechanism of Blast and Impact Waves by Using Nanoporous Materials," *Dynamic Behavior of Materials, Volume 1*, Springer International Publishing, pp. 177–183.
- [195] Hanssen, A., Langseth, M., and Hopperstad, O., 2001, "Optimum Design for Energy Absorption of Square Aluminium Columns with Aluminium Foam Filler," *International Journal of Mechanical Sciences*, **43**(1), pp. 153–176.
- [196] Toksoy, A. K., and Güden, M., 2005, "The Strengthening Effect of Polystyrene Foam Filling in Aluminum Thin-Walled Cylindrical Tubes," *Thin-Walled Structures*, **43**(2), pp. 333–350.
- [197] Zhang, Z., Liu, S., and Tang, Z., 2010, "Crashworthiness Investigation of Kagome Honeycomb Sandwich Cylindrical Column under Axial Crushing Loads," *Thin-Walled Structures*, **48**(1), pp. 9–18.
- [198] Lu, G., and Yu, T. X., 2003, Energy Absorption of Structures and Materials, CRC Press.

- [199] Chen, X., and Qiao, Y., 2007, "Science and Prospects of Using Nanoporous Materials for Energy Absorption," *MRS Proceedings*, **1041**.
- [200] Liu, Y., Schaedler, T. A., Jacobsen, A. J., Lu, W., Qiao, Y., and Chen, X., 2014, "Quasi-Static Crush Behavior of Hollow Microtruss Filled with NMF Liquid," *Composite Structures*, **115**(1), pp. 29–40.
- [201] Nicholas, T., 1981, "Tensile Testing of Materials at High Rates of Strain," *Experimental Mechanics*, **21**(5), pp. 177–185.
- [202] Chen, X., Xu, B., and Liu, L., 2014, "Nanoscale Fluid Mechanics and Energy Conversion," *Applied Mechanics Reviews*, **66**(5), p. 050803.
- [203] Namazi, H., Rakhshaei, R., Hamishehkar, H., and Kafil, H. S., 2016, "Antibiotic Loaded Carboxymethylcellulose/MCM-41 Nanocomposite Hydrogel Films as Potential Wound Dressing," *International Journal of Biological Macromolecules*, **85**, pp. 327–334.
- [204] Jang, D., Meza, L. R., Greer, F., and Greer, J. R., 2013, "Fabrication and Deformation of Three-Dimensional Hollow Ceramic Nanostructures.," *Nature materials*, **12**(10), pp. 893–8.
- [205] Mohd Amin, M. C. I., Ahmad, N., Halib, N., and Ahmad, I., 2012, "Synthesis and Characterization of Thermo- and PH-Responsive Bacterial Cellulose/Acrylic Acid Hydrogels for Drug Delivery," *Carbohydrate Polymers*, **88**(2), pp. 465–473.
- [206] Lei, Z., Wang, Q., Sun, S., Zhu, W., and Wu, P., 2017, "A Bioinspired Mineral Hydrogel as a Self-Healable, Mechanically Adaptable Ionic Skin for Highly Sensitive Pressure Sensing," *Advanced Materials*, **1700321**, pp. 1–6.
- [207] Chen, Q., Chen, H., Zhu, L., and Zheng, J., 2015, "Fundamentals of Double Network Hydrogels," *J. Mater. Chem. B*, **3**(3), pp. 3645–3886.
- [208] Wang, Q., Hou, R., Cheng, Y., and Fu, J., 2012, "Super-Tough Double-Network Hydrogels Reinforced by Covalently Compositing with Silica-Nanoparticles," *Soft Matter*, **8**(22), p. 6048.
- [209] Gong, J. P., Katsuyama, Y., Kurokawa, T., and Osada, Y., 2003, "Double-Network Hydrogels with Extremely High Mechanical Strength," *Advanced Materials*, **15**(14), pp. 1155–1158.
- [210] Yuk, H., Zhang, T., Lin, S., Parada, G. A., and Zhao, X., 2015, "Tough Bonding of Hydrogels to Diverse Non-Porous Surfaces," *Nature Materials*, **15**(November), pp. 1–25.
- [211] Xu, K., Li, W., Li, P., Wang, P., An, H., Liu, C., Tan, Y., and Lu, C., 2012, "Hydrophobically Associated Hydrogels Based on Acrylamide and Anionic Surface Active Monomer with High Mechanical Strength," *Soft Matter*, **8**(18), pp. 5078–5086.
- [212] Okumura, Y., and Ito, K., 2001, "The Polyrotaxane Gel: A Topological Gel by Figure-of-

- Eight Cross-Links," *Advanced Materials*, **13**(7), pp. 485–487.
- [213] Yang, S., Wang, J., Tan, H., Zeng, F., and Liu, C., 2012, "Mechanically Robust PEGDA—MSNs-OH Nanocomposite Hydrogel with Hierarchical Meso-Macroporous Structure for Tissue Engineering," *Soft Matter*, **8**, p. 8981.
- [214] Dept of Transportation (US) National Highway Traffic Safety Administration (NHTSA), 2009, Traffic Safety Facts: Occupant Protection (DOT HS 811 160).
- [215] Sun, Y., Li, P., Qiao, Y., and Li, Y., 2014, "Time-Dependent Gas-Liquid Interaction in Molecular-Sized Nanopores," *Scientific Reports*, **4**, p. 6547.
- [216] Lu, W., Han, A., Kim, T., Lim, H., and Qiao, Y., 2009, "Effects of Surface Charging Treatment on Outer and Inner Surfaces of a Nanoporous Carbon," *Journal of Materials Research*, pp. 2471–2475.
- [217] Grosu, Y., Giacomello, A., Meloni, S., González-Fernández, L., Chorazewski, M., Geppert-Rybczynska, M., Faik, A., Nedelec, J. M., and Grolier, J. P., 2018, "Viscosity at the Nanoscale: Confined Liquid Dynamics and Thermal Effects in Self-Recovering Nanobumpers," *Journal of Physical Chemistry C*, **122**(26), pp. 14248–14256.
- [218] Coiffard, L., and Eroshenko, V., 2006, "Temperature Effect on Water Intrusion/Expulsion in Grafted Silica Gels.," *Journal of colloid and interface science*, **300**(1), pp. 304–9.
- [219] Han, A., Lu, W., Punyamurtula, V. K., Kim, T., and Qiao, Y., 2009, "Temperature Variation in Liquid Infiltration and Defiltration in a MCM41," *Journal of Applied Physics*, **105**(2), pp. 2–5.
- [220] Grosu, Y., Ievtushenko, O., Eroshenko, V., Nedelec, J. M., and Grolier, J. P. E., 2014, "Water Intrusion/Extrusion in Hydrophobized Mesoporous Silica Gel in a Wide Temperature Range: Capillarity, Bubble Nucleation and Line Tension Effects," *Colloids and Surfaces A: Physicochemical and Engineering Aspects*, **441**, pp. 549–555.
- [221] Kim, T., Lu, W., Han, A., Punyamurtula, V. K., Chen, X., and Qiao, Y., 2009, "Effects of Anion Concentration on Ion-Transport Pressure in Nanopores," *Applied Physics Letters*, **94**(1), pp. 4–6.
- [222] Ryzhikov, A., Nouali, H., Daou, T. J., and Patarin, J., 2018, "A Drastic Influence of the Anion Nature and Concentration on High Pressure Intrusion-Extrusion of Electrolyte Solutions in Silicalite-1," *Physical Chemistry Chemical Physics*, **20**(9), pp. 6462–6468.
- [223] Forrestal, M. J., Wright, T. W., and Chen, W., 2007, "The Effect of Radial Inertia on Brittle Samples during the Split Hopkinson Pressure Bar Test," *International Journal of Impact Engineering*, **34**(3), pp. 405–411.
- [224] Hao, Y., and Hao, H., 2013, "Dynamic Compressive Behaviour of Spiral Steel Fibre Reinforced Concrete in Split Hopkinson Pressure Bar Tests," *Construction and Building Materials*, **48**, pp. 521–532.

- [225] Pankow, M., Salvi, A., Waas, A. M., Yen, C. F., and Ghiorse, S., 2011, "Split Hopkinson Pressure Bar Testing of 3D Woven Composites," *Composites Science and Technology*, **71**(9), pp. 1196–1208.
- [226] Ha, J. H., Yi, N. H., Choi, J. K., and Kim, J. H. J., 2011, "Experimental Study on Hybrid CFRP-PU Strengthening Effect on RC Panels under Blast Loading," *Composite Structures*, **93**(8), pp. 2070–2082.
- [227] Wu, C., Huang, L., and Oehlers, D. J., 2010, "Blast Testing of Aluminum Foam–Protected Reinforced Concrete Slabs," *Journal of Performance of Constructed Facilities*, **25**(5), pp. 464–474.
- [228] Hooper, P. A., Sukhram, R. A. M., Blackman, B. R. K., and Dear, J. P., 2012, "On the Blast Resistance of Laminated Glass," *International Journal of Solids and Structures*, **49**(6), pp. 899–918.